

# Diffusion Model’s Generalization Can Be Characterized by Inductive Biases toward a Data-Dependent Ridge Manifold

Ye He <sup>\*</sup>

Yitong Qiu <sup>†</sup>

Molei Tao <sup>‡</sup>

## Abstract

When a diffusion model is not memorizing the training data set, how does it generalize exactly? A quantitative understanding of the distribution it generates would be beneficial to, for example, an assessment of the model’s performance for downstream applications. We thus explicitly characterize what diffusion model generates, by proposing a log-density ridge manifold and quantifying how the generated data relate to this manifold as inference dynamics progresses. More precisely, inference undergoes a **reach-align-slide** process centered around the ridge manifold: trajectories first reach a neighborhood of the manifold, then align as being pushed toward or away from the manifold in normal directions, and finally slide along the manifold in tangent directions. Within the scope of this general behavior, different training errors will lead to different normal and tangent motions, which can be quantified, and these detailed motions characterize when inter-mode generations emerge. More detailed understanding of training dynamics will lead to more accurate quantification of the generation inductive bias, and an example of random feature model will be considered, for which we can explicitly illustrate how diffusion model’s inductive biases originate as a composition of architectural bias and training accuracy, and how they evolve with the inference dynamics. Experiments on synthetic multimodal distributions and MNIST latent diffusion support the predicted directional effects, in both low- and high-dimensions.

## 1 Introduction

Diffusion models (Sohl-Dickstein et al., 2015; Ho et al., 2020; Song et al., 2021) now deliver state-of-the-art sample quality across a wide range of generative tasks, which has made them a central tool for image, audio and video generation (Dhariwal and Nichol, 2021; Kong et al., 2021; Brooks et al., 2024). At the same time, understanding how innovative these models can be (or in other words, what exactly do they generate) is becoming increasingly important. In fact, certain diffusion models can memorize the training data and act like a stochastic parrot that just randomly repeats training data, which means the generation quality may appear to be high but in fact no new knowledge is created; in addition, it can lead to safety and privacy concerns (Carlini et al., 2023; Somepalli et al., 2023; Duan et al., 2023; Liu et al., 2024). Naturally, what triggers memorization of diffusion model has been extensively investigated (e.g., Kadkhodaie et al., 2023; Zhang et al., 2023). By now, it is fairly well accepted that it is the various sources of error inside diffusion model that give its non-memorization; in fact, criteria for (non-)memorization can already be made rather quantitative (e.g., Ye et al., 2025), and ‘generalization’ became a synonym of non-memorization in this literature.

One important question still being actively investigated though is, when diffusion model is not memorizing, how/where does the model produce new samples different from the training set, i.e. how does it innovate knowledge. A quantitative, explicit answer would help distinguish generalization from hallucination and assess the applicability of the generative model to specific downstream tasks. The powerful classical theory

<sup>\*</sup>Georgia Institute of Technology. yhe367@gatech.edu

<sup>†</sup>University of Science and Technology of China. qyt0912@mail.ustc.edu.cn

<sup>‡</sup>Georgia Institute of Technology. mtao@gatech.edu

of statistical learning can help bound the gap between the generated distribution and the latent population distribution (e.g., [Wang et al. \(2024, Theorem 3\)](#)), but in practice such a worst-case bound can be loose as it needs to account for all possible population distributions that are consistent with the finite dataset which the model trains on. This motivates an alternative, fully data-dependent perspective: compare the generated distribution directly to the empirical distribution of the training data, and regard this discrepancy as the model’s generalization.

Many recent progress along this line provide rich insights. For example, [Aithal et al. \(2024\)](#)’s seminal empirical investigation suggests some geometric bias, in which generated data concentrate in structured regions that connect distinct modes of the data. More systematically speaking, generalization in diffusion models may arise from several mechanisms, and the literature studies it from complementary perspectives. One perspective concerns the *target*, asking whether stochasticity in the finite training target is itself a driver of generalization ([Vastola, 2025](#); [Bertrand et al., 2025](#)). A second perspective examines *training inductive bias* ([Kamb and Ganguli, 2024](#); [Shah et al., 2025](#); [Wu et al., 2025](#); [Bonnaire et al., 2025](#)), characterizing how the learned reverse-time dynamics depend on the model class and learning procedure. A third perspective focuses on *inference* ([Baptista et al., 2025](#); [Chen, 2025](#); [Farghly et al., 2025](#)), understanding what reverse-time inference dynamics generate under manually assumed structured training error. While extremely insightful, the literature still lacks a rigorous and quantitative understanding of diffusion model’s generalization.

Motivated by this gap, we develop a purely data-driven (no population distribution involved) framework to explicitly quantify the inductive biases of diffusion model’s generation. Our work integrates the perspectives in the literature: On the *target* side, we treat the finite training dataset as the target and analyze how the generated distribution relates to the empirical distribution of training data, rather than attributing generalization to the stochasticity of sampling an unknown population distribution. On the *inference* side, we make the data-structure explicit by constructing a time-indexed family of log-density ridge sets from the smoothed empirical density, and we analyze how inference trajectories evolve relative to this geometry. This differs from the work ([Farghly et al., 2025](#)) that motivates log-density smoothing as a useful analytical lens but does not study the simulated inference dynamics or provides a ridge-manifold description based on the data. On the *training* side, building on random-feature analyses of diffusion training ([George et al., 2025](#); [Bonnaire et al., 2025](#)), we go beyond test/training error comparisons and show how limited-expressivity parametrization (due to finite width) and inaccurate optimization translate into *directional* geometric effects during inference. Our results confirm and explain when and why samples will populate structured intermediate regions beyond the training dataset, how this behavior depends on both the time of the sampling dynamics and what is learned during training. Compared to recent analytical explanations of interpolation bias that rely on stylized settings or imposed error ansatz (e.g., two-point data and smoothed empirical score) ([Chen, 2025](#)), our results are derived under verifiable regularity conditions and explicitly connect the resulting geometric bias to the dataset and to training parameters. We also complement the interesting work of ([Li et al., 2025](#)), which investigates the transition between sampling uniform from some low-dimensional manifold and sampling a target distribution supported on the manifold, as our setting differs in two key ways: first, we study the full denoising diffusion, where noise level is time-dependent and vanishing as sampling approaches the data, as opposed to constant-noise level considered; second, rather than assuming there is some underlying manifold without spelling out what it is, we explicitly characterize the geometric object that governs generation in our framework and quantify how the learned score/mean estimator drives the inference dynamics around this object.

As illustrated in Figure 1, our theoretical results (Section 3) show that the inference dynamics follows a simple reach-align-slide progression, which can be summarized as follows:

1. **Reach:** after an initial transient, generated samples enter a neighborhood of the corresponding log-density ridge, so the log-density ridge becomes the natural reference geometry for the rest of the inference trajectory.

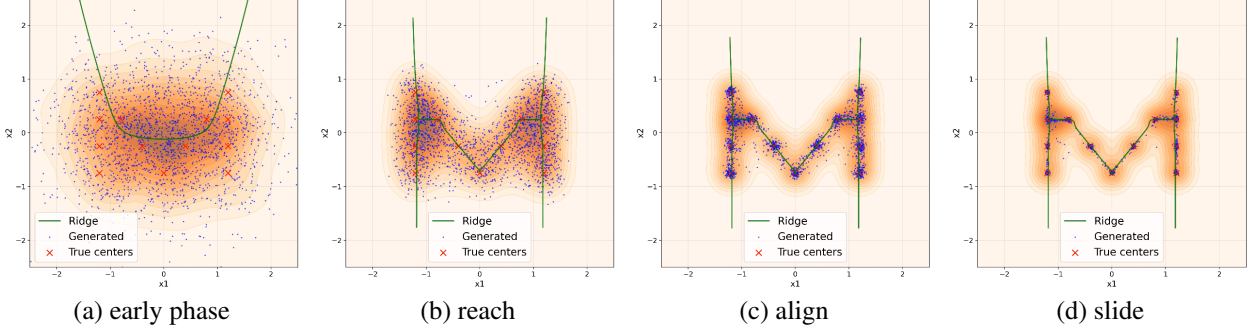


Figure 1: **Illustration of the generation inductive bias.** 13 training points (red crosses) form a letter ‘M’ in 2D. Generated samples (blue dots) evolve relative to the time-indexed log-density ridges (green curve) by following reach-align-slide. The background color represents the KDE.

2. **Normal alignment:** generated samples move closer to the log-density ridge and effectively align with it. The closest distance, however, does not vanish in general and is controlled by the component of the training error in the normal directions.
3. **Tangent sliding:** generated samples slide along the log-density ridge toward training samples, which can populate structured intermediate regions between training samples. The tangent concentration around training samples is controlled by the component of the training error in the tangent directions.

Unlike test-error-based notions of generalization, the reach-align-slide view demonstrates that a generated samples are explicitly concentrated on a geometric structure terms as ‘ridge’ (Definition 3.1), and our theory also characterizes how training error can result in different generated distribution along the ridge (Section 4.1). The latter can be made very explicit when we consider random feature neural network (RFNN) trained by gradient descent (GD) in Section 4.2, where the training error admits closed-form decompositions that map onto normal & tangent directions induced by ridges.

## 2 Preliminaries

**SDE-based Diffusion Models.** To generate new samples in  $\mathbb{R}^d$  based on  $n$ -many existing data samples  $\{x_0^{(i)}\}_{i=1}^n \subset \mathbb{R}^d$ , the variance-preserving (VP) SDE-based diffusion models consider forward process  $(X_t)_{0 \leq t \leq T}$  satisfying  $dX_t = -X_t dt + \sqrt{2} dB_t$  for all  $t \in [0, T]$ , with marginals  $p_t = \text{Law}(X_t)$  and  $p_0 = p$  being the data distribution. The reverse process  $(Y_t)_{0 \leq t \leq T}$  satisfies,

$$dY_t = (Y_t + 2\nabla \log p_{T-t}(Y_t)) dt + \sqrt{2} d\bar{B}_t, \quad 0 \leq t \leq T - \delta. \quad (1)$$

The term  $\{s(t, x) = \nabla \log p_t(x)\}_{\delta \leq t \leq T}$  in (1) is referred as the score function. The early stopping time  $0 < \delta \ll 1$  is to make sure the score function is well-defined. In practice, (1) is simulated using Gaussian initial condition. As it is challenging to compute score directly, people usually learn  $s(t, x)$  through optimizing the denoising score matching loss  $\mathcal{L}_{\text{DSM}} = \int_{\delta}^T w(t) \mathbb{E}[\|s_{\theta}(t, X_t(z)) + \frac{z}{\sqrt{h_t}}\|^2] dt$  where  $a_t := e^{-t}$ ,  $h_t = 1 - e^{-2t}$ ,  $X_t(z) := a_t X_0 + \sqrt{h_t} z$  and  $z \sim \mathcal{N}(0, I_d)$  is independent to  $X_0$ .  $w(t)$  is the training weight and  $s_{\theta}(t, x)$  is the parametrized score.

**Denoising Mean Matching Loss.** In this work, we consider an alternative training loss, which is motivated by the Tweedie’s formula: the score is determined by posterior mean of the clean data conditioned on noisy observation:  $\nabla \log p_t(x) = -\frac{x}{h_t} + \frac{1}{h_t} \mathbb{E}_{x_0 \sim p_{0|t}(\cdot|x)}[a_t x_0]$ . This identity shows that learning the score  $\nabla \log p_t(x)$  is essentially equivalent to learning the posterior mean

$$m(t, x) := \mathbb{E}_{x_0 \sim p_{0|t}(\cdot|x)}[a_t x_0], \quad (2)$$

Thus, we can view learning in diffusion model as learning either the score or the posterior mean. We adopt the latter as it is consistent with the viewpoint in [Li and He \(2025\)](#) that data-prediction is a direct way to learn structure of clean data, especially when they concentrate near low-dim structure, which aligns with our geometric focus; analyzing the former would be analogous though.

The mean matching loss that controls the gap between the exact reverse process and the approximated reverse process can be expressed via the posterior mean  $m(t, x)$ :

$$\mathcal{L}_{\text{MM}} = \int_{\delta}^T w(t) h_t^{-2} \mathbb{E}[\|m_A(t, X_t) - m(t, X_t)\|^2] dt, \quad (3)$$

where  $m_A(t, x)$  is parametrized by neural networks to approximate the posterior mean  $m(t, x)$ . Since  $\mathcal{L}_{\text{MM}}$  is hard to evaluate directly using data samples, we instead minimize the denoising posterior mean matching loss (analogue to denoising score matching loss):

$$\mathcal{L}_{\text{DMM}} = \int_{\delta}^T w(t) h_t^{-2} \mathbb{E}[\| -a_t X_0 + m_A(t, X_t) \|^2] dt. \quad (4)$$

Crucially,  $\mathcal{L}_{\text{DMM}}$  is fully computable from the training set by drawing  $X_0$  from data. For more details on the DMM loss, we refer the readers to [Appendix A](#). In our paper, for the convenience of our analysis, we assume the expectations wrt. the noises in  $\mathcal{L}_{\text{DMM}}$  and time  $t$  are exactly evaluated and denote the learned posterior mean by  $m_A$ . The inference process, initialized at Gaussian, is characterized by the SDE

$$d\tilde{Y}_t = (\tilde{Y}_t + 2h_{T-t}^{-1}(m_A(T-t, \tilde{Y}_t) - \tilde{Y}_t)) dt + \sqrt{2} dB_t, \quad t \in [0, T-\delta]. \quad (5)$$

**Random Feature Neural Network and Gradient Descent.** We consider a simplified but analytical favored representation, random features neural networks (RFNN), for the posterior mean parametrization. Similar RFNN has been studied in [George et al. \(2025\)](#); [Bonnaire et al. \(2025\)](#), but whereas they study asymptotic regimes with dimension  $d$ , width  $p$  and data size  $n$  growing, we focus on a nonasymptotic setting where  $d, p, n$  are fixed and our results explicitly track their finite values. In particular, the parametrized posterior mean is represented by a two-layer neural network

$$m_A(t, x) := \frac{A}{\sqrt{p}} \sigma\left(\frac{W_x x}{\sqrt{d}} + \frac{W_t \varphi_t}{\sqrt{2K_t + 1}} + b\right) := \frac{A}{\sqrt{p}} \sigma_t(x) \quad (6)$$

where  $W_x \in \mathbb{R}^{p \times d}$  and  $W_t \in \mathbb{R}^{p \times (2K_t + 1)}$  are Gaussian random matrices with i.i.d. standard Gaussian entries, also independent to  $\xi$ .  $\varphi_t \in \mathbb{R}^{2K_t + 1}$  consists of  $2K_t + 1$  Fourier basis on  $[0, T]$ .  $b \sim \mathcal{N}(0, I_p)$  is the bias feature, independent to  $W_x, W_t$ .  $\sigma$  is the nonlinear activation function and  $A \in \mathbb{R}^{d \times p}$  is the parameter matrix to learn. The DMM loss denoted as  $\mathcal{L}_{\text{DMM}}(A)$ , is then given by  $\mathcal{L}_{\text{DMM}}(A) = \int_{\delta}^T \frac{w(t)}{h_t^2} \mathbb{E}[\| -a_t X_0 + \frac{A}{\sqrt{p}} \sigma_t(X_t) \|^2] dt$ . We optimize  $\mathcal{L}_{\text{DMM}}(A)$  by gradient descent with constant learning rate  $\eta$ , with iterations given by

$$A_{k+1} - A_k = -2\eta A_k \tilde{U} + 2\eta \tilde{V}, \quad (7)$$

with  $\tilde{U} = \int_{\delta}^T \frac{w(t)}{h_t^2} \frac{\mathbb{E}[\sigma_t(X_t) \sigma_t(X_t)^\top]}{p} dt \in \mathbb{R}^{p \times p}$  and  $\tilde{V} = \int_{\delta}^T \frac{w(t)}{h_t^2} \frac{\mathbb{E}_z[a_t X_0 \sigma_t(X_t)^\top]}{\sqrt{p}} dt \in \mathbb{R}^{d \times p}$ .

### 3 Geometric Dynamical Properties of the Inference Process

In this section, we introduce a family of data-dependent ridge manifolds across noise levels and study how the dynamic of  $\{\tilde{Y}_t\}_{0 \leq t \leq T-\delta}$  behaves relative to these sets. After stating mild assumptions on the data, we establish geometric properties needed for the analysis and prove dynamical results that formalize the reach-align-slide behavior.

**Assumption 1** (Empirical Data Distribution). *Data points  $\{x_0^{(i)}\}_{i=1}^n$  are well-separated and bounded, i.e.,  $\Delta := \min_{i \neq j} \|x_0^{(i)} - x_0^{(j)}\| > 0$  and  $R := \max_i \|x_0^{(i)}\| < \infty$ . The data distribution  $p$  is the empirical distribution of the data, i.e.,  $p = \frac{1}{n} \sum_{i=1}^n \delta_{x_0^{(i)}}$ .*

### 3.1 Data-dependent Manifolds - Log-density Ridge Sets

Genovese et al. (2014); Chen et al. (2015) introduced the notion of density ridge sets to characterize low-dimensional geometric properties of a probability density/point cloud. That notion is insufficient for this research, but it turns out once we replace density by *log density*, the new definition will closely relate to where diffusion model generalizes, as will be shown in Section 3.2-3.4.

**Definition 3.1** (Log-density Ridge Sets). *For any smooth probability density  $p$  on  $\mathbb{R}^d$  and any positive integer  $d^* < d$ , the  $d^*$ -dimensional log-density ridge set of  $p$  with threshold  $\beta > 0$ , denoted as  $\mathcal{R}_{d^*}(p; \beta)$ , is defined by*

$$\mathcal{R}_{d^*}(p; \beta) := \left\{ x \in \mathbb{R}^d \mid E(x)E(x)^\top \nabla \log p(x) = 0, \lambda_{d^*+1}(x) \leq -\beta \right\}$$

where  $E(x) = (v_{d^*+1}(x), \dots, v_d(x)) \in \mathbb{R}^{d \times (d-d^*)}$  with  $\{(\lambda_i(x), v_i(x))\}_{i=1}^d$  being the eigenvalues/eigen-vectors of  $\nabla^2 \log p(x)$  s.t.  $\lambda_1(x) \geq \lambda_2(x) \dots \geq \lambda_{d^*}(x) > \lambda_{d^*+1}(x) \geq \dots \geq \lambda_d(x)$  for all  $x \in \mathbb{R}^d$ .

**Notation and visualization.** For  $t \in [\delta, T]$ , this work considers a sequence of log-density ridge sets of the forward marginal  $p_t = \text{Law}(X_t)$  with threshold  $\beta_t = \Theta(1/h_t)$  for small  $t$ . For simplicity, we denote this ridge set by  $\mathcal{R}_t$ . This choice of  $\beta_t$  is the key to establish our dynamical framework, meanwhile it also guarantees the curvature condition in Definition 3.1 for almost every points when  $t$  is small (an argument based on properties of  $\nabla^2 \log p_t$  is included in Remark C.3). As shown in Figure 1, the log-density ridges capture the dominant low-dim geometry of  $p_t$ .

**Tube neighborhood and projection map.** Our analysis quantifies how the reverse-time inference process relates to the evolving ridge geometry. We therefore work in a tube neighborhood around  $\mathcal{R}_t$  where the nearest-point projection  $\Pi_t$  is well-defined. Let  $\text{dist}(x, \mathcal{R}_t)$  be the Euclidean distance to  $\mathcal{R}_t$ . Assumption 2 states that  $\mathcal{R}_t$  has positive reach, which guarantees uniqueness and regularity of the nearest-point projection in a nontrivial neighborhood.

**Assumption 2** (Smoothness and positive reach). *For any  $t \in [\delta, T]$ , there exists  $r_t > 0$  such that  $\mathcal{R}_t$  is a (piecewise)  $C^2$ -embedded submanifold in  $\mathbb{R}^d$  with a reach no smaller than  $r_t > 0$ , i.e., for all  $x \in \mathbb{R}^d$  with  $\text{dist}(x, \mathcal{R}_t) \leq r_t$ , there exists unique  $x^* \in \mathcal{R}_t$  such that  $\text{dist}(x, \mathcal{R}_t) = \|x - x^*\|$ .*

**Connection to the data assumption.** Under Assumption 1, we verify that the log-density ridge sets  $\mathcal{R}_t$  indeed satisfy Assumption 2; moreover we obtain explicit data-dependent estimates for the reach  $r_t$  and estimations for  $\|\nabla \Pi_t\|$  and  $\|\partial_t \Pi_t\|$  in Proposition 3.1. These verifications and rate calculations are deferred to Appendix C.

**Proposition 3.1.** *Under Assumption 1, the log-density ridge sets  $\{\mathcal{R}_t\}_{\delta \leq t \leq T}$  satisfy Assumption 2 with  $r_t = \Omega(h_t^2 \theta_t^{-1} R^{-3})$  and arbitrary  $\theta_t = \exp(-o(h_t^{-1}))$  as  $t \rightarrow \delta^+ \ll 1$ . Furthermore, for any  $\rho_t \in (0, r_t)$  and the tube neighborhood  $\mathcal{T}_t(\rho_t)$  given below*

$$\mathcal{T}_t(\rho_t) := \{x \in \mathbb{R}^d \mid \text{dist}(x, \mathcal{R}_t) \leq \rho_t\}, \quad (8)$$

the nearest-point projection  $\Pi_t : \mathcal{T}_t(\rho_t) \rightarrow \mathcal{R}_t$  is well-defined with the following properties:

- (1)  $\forall x \in \mathcal{T}_t(\rho_t)$ ,  $n_t(x) := x - \Pi_t(x)$  is in the normal space at  $\Pi_t(x)$ , i.e.,  $n_t(x) \in N_{\Pi_t(x)}(\mathcal{R}_t)$ ;
- (2)  $\Pi_t$  is  $C^1$  on  $\mathcal{T}_t(\rho_t)$  and  $\sup_{x \in \mathcal{T}_t(\rho_t)} \|\nabla \Pi_t(x)\| \leq \frac{1}{1 - \rho_t/r_t}$ ;
- (3) the motion of  $\Pi_t$  is bounded: picking  $\rho_t = \Theta(r_t)$ ,  $\sup_{x \in \mathcal{T}_t(\rho_t)} \|\partial_t \Pi_t(x)\| = \mathcal{O}(R)$ .

### 3.2 Stage 1 - Reaching the Tube Neighborhood

We define a stopping time  $\tilde{t}_{\text{in}} := \inf\{0 \leq t \leq T - \delta \mid \tilde{Y}_t \in \mathcal{T}_{T-t}(\rho_{T-t})\}$ . The following theorem characterize the entry of  $\tilde{Y}_t$  into the neighborhood  $\mathcal{T}_{T-t}(\rho_{T-t})$ .

**Theorem 3.1** (Informal, formal one in Theorem D.1). *Under Assumption 1, we have*

$$\mathbb{P}(\tilde{t}_{\text{in}} \leq T - \delta) \geq 1 - e_\delta - \varepsilon(T) - \sqrt{\varepsilon_A(T, \delta)/8},$$

where  $\lim_{\delta \rightarrow 0^+} e_\delta = 0$ ,  $\lim_{T \rightarrow \infty} \varepsilon(T) = 0$  and  $\varepsilon_A(T, \delta) := \int_\delta^T h_t^{-2} \mathbb{E}[\|m(t, X_t) - m_A(t, X_t)\|^2] dt$ .

### 3.3 Stage 2 - Aligning along Normal Directions

For any  $x \in \mathcal{T}_{T-t}(\rho_{T-t})$ , as proved in Proposition B.1, we can define the square-normal distance from any  $x \in \mathcal{T}_{T-t}(\rho_{T-t})$  to  $\mathcal{R}_{T-t}$  as  $D_{T-t}(x) := \|x - \Pi_{T-t}(x)\|^2 = \|n_{T-t}(x)\|^2$ . After  $\tilde{Y}_t$  enters the neighborhood  $\mathcal{T}_{T-t}(\rho_{T-t})$ ,  $D_{T-t}(\tilde{Y}_t)$  exhibits the following contraction property, with proof deferred to Appendix E.

**Theorem 3.2.** *Under Assumption 1, define  $\kappa_{s,t} = 2 \int_s^t (\beta_{T-u} - 1) du$ ,  $B_{s,t}(d, R) = \int_s^t e^{-\kappa_{u,t}} (\rho_{T-u} R + d) du$  and  $e_A^\perp(t, x) := P^\perp(\Pi_t(x)) e_A(t, x)$  with  $e_A = m_A - m$ . Then for any  $t \in [\tilde{t}_{\text{in}}, T - \delta]$ ,*

$$\mathbb{E}[D_{T-t}(\tilde{Y}_t)] \lesssim e^{-\kappa_{\tilde{t}_{\text{in}}, t}} \rho_{T-\tilde{t}_{\text{in}}} + B_{\tilde{t}_{\text{in}}, t}(d, R) + \int_{\tilde{t}_{\text{in}}}^t e^{-\kappa_{u,t}} \frac{\mathbb{E}[\|e_A^\perp(T-u, \tilde{Y}_u)\|^2]}{h_{T-u}^2 \beta_{T-u}} du.$$

Furthermore, picking  $\beta_t = c/h_t$  for any  $c \in [\frac{1}{2}, 1]^1$ , when  $\delta \ll 1$ , we have

$$\mathbb{E}[D_\delta(\tilde{Y}_{T-\delta})] = \mathcal{O}(d\delta^c + \delta^c \int_{\tilde{t}_{\text{in}}}^{T-\delta} h_{T-u}^{-1-c} \mathbb{E}[\|e_A^\perp(T-u, \tilde{Y}_u)\|^2] du).$$

### 3.4 Stage 3 - Sliding along Tangent Directions

For any  $t \in [0, T - \delta]$ ,  $p_{T-t}$  is mixture of Gaussians with centers  $\{m_{T-t}^{(i)} := a_{T-t} x_0^{(i)}\}_{i=1}^n$ . At each center, we define a center-dominant region  $\mathcal{B}_{T-t}^{(i)}(\theta_{T-t}) := \{x \in \mathbb{R}^d \mid \text{Softmax}(-\frac{\|x - m_{T-t}^{(i)}\|^2}{2h_{T-t}})_i \geq 1 - \theta_{T-t}\}$  where  $\theta_s$  is arbitrary s.t.  $\theta_s = \exp(-o(h_s^{-1}))$  as  $s \rightarrow 0^+$ . Under Assumption 1, as  $t \rightarrow T - \delta$  and  $\delta \ll 1$ , the union of all center-dominated regions covers almost every point in the space and  $\tilde{Y}_t$  enters it. More details are deferred to Appendix C. Near the end of inference,  $\tilde{Y}_t$  enters one of the center-dominant regions, we can approximate the tangent component locally at the associate center: for  $\tilde{Y}_t \in \mathcal{T}_{T-t}(\rho_{T-t}) \cap \mathcal{B}_{T-t}^{(i)}(\theta_{T-t})$ , the tangent components are defined as

$$\tilde{u}_t^{(i)} := (U_{T-t}^{(i)})^\top (\tilde{Y}_t - m_{T-t}^{(i)}) \in \mathbb{R}^{d^*}, \quad (9)$$

where  $U_{T-t}^{(i)} \in \mathbb{R}^{d \times d^*}$  is the matrix consisting of orthonormal columns as the top- $d^*$  eigenvectors of  $\nabla^2 \log p_{T-t}(m_{T-t}^{(i)})$ . Then we can track and estimate the squared-tangent distance  $\|\tilde{u}_t^{(i)}\|^2$ . We introduce the result in the following theorem, and leave the details and proofs to Appendix F.

**Theorem 3.3.** *Under Assumption 1, for any  $t \in [\tilde{t}_{\text{in}}, T - \delta]$ , define  $e_A^{\parallel, i}(t, x) = (U_t^{(i)})^\top e_A(t, x)$  with  $e_A = m_A - m$ . If  $\tilde{Y}_t \in \mathcal{B}_{T-t}^{(i)}(\theta_{T-t})$ , then we have*

$$\frac{d}{dt} \mathbb{E}[\|\tilde{u}_t^{(i)}\|^2] \leq -\left(\frac{1}{h_{T-t}} - 2\right) \mathbb{E}[\|\tilde{u}_t^{(i)}\|^2] + \tilde{\epsilon}_{T-t}^{(i)} + \frac{4}{h_{T-t}} \|e_A^{\parallel, i}(T-t, \tilde{Y}_t)\|^2,$$

<sup>1</sup> $c$  can be chosen arbitrarily between  $[\frac{1}{2}, 1]$  due to the property of  $\nabla^2 \log p_t(x)$  as explained in Remark C.3.

where  $\tilde{e}_{T-t}^{(i)} = \mathcal{O}(d)$ . Furthermore, with  $\delta \ll 1$ , we have

$$\mathbb{E}[\|\tilde{u}_{T-\delta}^{(i)}\|^2] = \mathcal{O}(d\sqrt{\delta} + \sqrt{\delta} \int_{\tilde{t}_{\text{in}}}^{T-\delta} h_{T-u}^{-\frac{3}{2}} \mathbb{E}[\|e_A^{\parallel,i}(T-u, \tilde{Y}_u)\|^2] du).$$

**Remark 3.1** (Comparison between normal&tangent directions). *Our bounds in Theorems 3.2,3.3 show that geometry at the final inference stage is controlled by dimension-errors and the cumulated mean-errors, splitting along normal&tangent directions. The discrepancy on the coefficients in the two directions orients from different contraction mechanisms: normal contraction is due to the curvature threshold of the ridge, hence depending on the  $\beta_t$ -related parameter  $c$ ; while tangential contraction is purely driven by the reverse-time SDE. While the discrepancy makes the normal dimension-error ( $d\delta^c$ ) smaller than the tangential dimension-error ( $d\delta^{1/2}$ ), its effect on the mean-errors is consistent in the two directions. Both reflect that the training weight  $w(t)$  sets how hard the objective pushes down the end-stage mean-errors: if the per-time error  $w(t)h_t^{-2}\mathbb{E}[\|e_A(T-t, \tilde{Y}_t)\|^2] = \mathcal{O}(1)$ , the normal and tangential mean-errors scale like  $\delta^c \int_{\delta}^{T-\tilde{t}_{\text{in}}} h_t^{1-c}/w(t)dt$  and  $\delta^{1/2} \int_{\delta}^{T-\tilde{t}_{\text{in}}} h_t^{1/2}/w(t)dt$  respectively. In particular, under weights  $w(t) = h_t^2, h_t, 1$ , the mean-errors along both directions yield  $\mathcal{O}(1), \mathcal{O}(\delta), \mathcal{O}(\delta^2)$  respectively, hence inducing different inductive biases in generation.*

## 4 How Training Affects Generation: General Theory + an Explicit RF Example

This section explains how to incorporate understandings of score-training dynamics into the reach-align-slide picture in Section 3. The key idea is to control the normal and tangential error terms in Theorem 3.2 and Theorem 3.3 using the corresponding components of the posterior mean matching loss  $\mathcal{L}_{\text{MM}}$  in (3), namely  $\mathcal{L}_{\text{MM}}^{\perp}$  and  $\mathcal{L}_{\text{MM}}^{\parallel}$ . This yields a direct interface:

$$\text{training dynamics} \implies (\mathcal{L}_{\text{MM}}^{\perp}, \mathcal{L}_{\text{MM}}^{\parallel}) \implies \text{alignment and sliding guarantees.}$$

Decomposing  $\mathcal{L}_{\text{MM}}^{\perp}$  and  $\mathcal{L}_{\text{MM}}^{\parallel}$  into architecture-driven and optimization-driven parts then translates architecture capacity (network width) and optimization choices (training time and initialization) into quantitative predictions on (i) how tightly inference aligns to the ridge geometry; (ii) how much it spreads along the ridge. We made the results very concrete for RFNN (or RF for shorter abbreviation) thanks to its linear training dynamics (although we note RF is just an example; in fact, since the first end-to-end generation accuracy bound (Wang et al., 2024), there have been several good works analyzing the training dynamics of diffusion model in various contexts (e.g., Wang et al., 2024; Han et al., 2025; Cui et al., 2025)). The general theory relating training dynamics to the log-density ridge geometry will be presented in Section 4.1; more explicit results based on finite-size RF trained by gradient **descent**<sup>2</sup> will be presented in Section 4.2, and a concrete example for sized-2 training set will be elaborated in Section 4.3, where both components admit explicit decompositions into an *architecture* term (width-limited) and an *optimization* term (training-time dependent).

### 4.1 Directional Decomposition along Log-density Ridges

The posterior mean matching error decomposes into *directional mean-matching errors*, i.e.,  $\mathcal{L}_{\text{MM}} = \mathcal{L}_{\text{MM}}^{\perp} + \mathcal{L}_{\text{MM}}^{\parallel}$  s.t. for  $\dagger \in \{\perp, \parallel\}$ ,  $\mathcal{L}_{\text{MM}}^{\dagger}(A) := \int_{\delta}^T \frac{w(t)\mathbb{E}[\|P_t^{\dagger}(X_t)e_A(t, X_t)\|^2]}{h_t^2} dt$  with  $e_A := m_A - m$ .

---

<sup>2</sup>As opposed to gradient flow in the seminal work of Bonnaire et al. (2025), where the RF is of infinite width and data dimension goes to infinity too, which also differ from our nonasymptotic setting.

**Theorem 4.1.** *Under mild assumptions, the normal/tangent-error in Theorems 3.2 and 3.3 can be estimated by the projected posterior mean matching loss in normal/tangent direction, i.e.,*

$$\text{normal-error bound} \lesssim C_\delta^\perp \mathcal{L}_{\text{MM}}^\perp(A) + d\delta^c + C_\delta^\perp(\sqrt{d} + R)e^{-T}, \quad (10)$$

$$\text{tangent-error bound} \lesssim C_\delta^{\parallel} \mathcal{L}_{\text{MM}}^{\parallel}(A) + d\delta + C_\delta^{\parallel}(\sqrt{d} + R)e^{-T}. \quad (11)$$

where  $C_\delta^\perp := \delta^c (1 \vee \frac{\delta^{1-c}}{w(\delta)})$ ,  $C_\delta^{\parallel} := \delta^{\frac{1}{2}} (1 \vee \frac{\delta^{\frac{1}{2}}}{w(\delta)})$  and  $c = \lim_{t \rightarrow \delta} h_t \beta_t$  is arbitrary in  $[\frac{1}{2}, 1]$ .

**Remark 4.1.** *The training-independent terms in the bounds can be made small by taking small  $\delta$  and large  $T$ . The remaining contributions admit a linear decomposition into normal and tangential parts,  $\mathcal{L}_{\text{MM}}^\perp$  and  $\mathcal{L}_{\text{MM}}^{\parallel}$ , because the inverse-time dynamics is linear in the (learned) posterior mean. While these two terms share the same structural form, their magnitudes can differ substantially since they depend on the particular training output. Importantly, the resulting estimates are still nontrivial: they bound and predict the inference trajectory ( $\tilde{Y}_t$ ) using only quantities determined by the training output together with the reference OU process. Establishing this connection requires only mild assumptions on training, which we state in Appendix G.*

## 4.2 Application in RF+GD

Let  $\tilde{U}$  be the RFNN kernel in (7) with rank  $r \leq p$  and eigen-decomposition  $\tilde{U} = \sum_{j=1}^r \lambda_j u_j u_j^\top$  with  $\{u_j\}_{j \in [r]}$  being a set of orthonormal vectors and  $\lambda_1 > \lambda_2 > \dots > \lambda_r > 0$ .

**Theorem 4.2** (Training-time and width control geometric behavior). *Assume the conditions in Theorems 3.2, 3.3, 4.1 hold. Let  $\{A_k\}_{k \geq 0}$  be the GD iterates in (7) with learning rate  $\eta < \frac{2}{\lambda_1}$ , then*

$$\begin{aligned} \text{normal-error bound at step } k &\lesssim C_\delta(\text{Err}_{\text{arc}}^\perp + \text{Err}_{\text{train}}^\perp(k)) + \text{remainder}, \\ \text{tangent-error bound at step } k &\lesssim C_\delta(\text{Err}_{\text{arc}}^{\parallel} + \text{Err}_{\text{train}}^{\parallel}(k)) + \text{remainder}. \end{aligned}$$

For each  $\dagger \in \{\perp, \parallel\}$ ,

- (1) the architecture term  $\text{Err}_{\text{arc}}^\dagger$  is the weighted least-squares residual evaluated at  $A^* = A_0(I_p - \tilde{U}\tilde{U}^\top) + \tilde{V}\tilde{U}^\top$ :  $\text{Err}_{\text{arc}}^\dagger = \int_\delta^T \frac{w(t)}{h_t^2} \mathbb{E}[\|P_t^\dagger(X_t)e_{A^*}(t, X_t)\|^2] dt$ .
- (2) the optimization term is expressed as  $\text{Err}_{\text{train}}^\dagger(k) = \sum_{j,l=1}^r (1-2\eta\lambda_j)^k (1-2\eta\lambda_l)^k a_j^\top P_{jl}^\dagger a_l + 2 \sum_{j=1}^r (1-2\eta\lambda_j)^k a_j^\top b_j^\dagger$ , where  $a_j = (A_0 - \tilde{V}\tilde{U}^\top)u_j \in \mathbb{R}^d$  for all  $j \in [r]$ ,  $P_{jl}^\dagger \in \mathbb{R}^{d \times d}$  and  $b_j^\dagger \in \mathbb{R}^d$  are ridge-projected feature covariances/cross-terms (formulas in Appendix H (28)).

Consequently, increasing training time  $k$  reduces both effects geometrically, while increasing width  $p$  primarily reduces the irreducible architecture error bounds  $\text{Err}_{\text{arc}}^\perp, \text{Err}_{\text{arc}}^{\parallel}$ .

## 4.3 RFNN for Two Points in 2D

Consider the two-point dataset in  $\mathbb{R}^2$ . Assume WLOG  $x_0^{(1)} = (-\mu, 0)$  and  $x_0^{(2)} = (\mu, 0)$ . Here  $\mathcal{R}_t \equiv \{(x_1, 0) | x_1 \in \mathbb{R}\}$  and the posterior mean is  $m(t, x) = (a_t \mu \tanh(\frac{a_t \mu}{h_t} x_1), 0) := (f_t(x_1), 0)$ . Moreover, the second row of  $\tilde{V}$  is zero, i.e.,  $\tilde{V} = e_1 \tilde{v}^\top$  for some  $\tilde{v} \in \mathbb{R}^p$ . Denoting the gradient descent initialization  $A_0 = (A_{0,1}, A_{0,2})^\top$ , the optimization-driven errors along tangent and normal directions are respectively given by  $\text{Err}_{\text{train}}^{\parallel}(k) = \sum_{i=1}^r \lambda_i (1-2\eta\lambda_i)^{2k} (A_{0,1}^\top u_i - \tilde{v}^\top u_i / \lambda_i)^2$  and  $\text{Err}_{\text{train}}^\perp(k) = \sum_{i=1}^r \lambda_i (1-2\eta\lambda_i)^{2k} (A_{0,2}^\top u_i)^2$ . Both errors decay to zero as  $k \rightarrow \infty$ , but their magnitudes at finite training time depend on how the initialization aligns with the kernel eigenvectors  $\{u_i\}_{i=1}^r$ . As a result, the error can be very different in normal

versus tangent directions, hence leading to different geometric generation outcomes. For instance, normal-direction (vertical) generation behavior under finite width ( $p$ ) and finite training time ( $k$ ) differs sharply across initializations:

- (1) *Zero initialization*: if  $A_{0,2} = 0$ , then  $\text{Err}_{\text{train}}^{\perp}(k) \equiv 0$  and hence  $\mathcal{L}_{\text{MM}}^{\perp} \equiv 0$ . The theory therefore predicts essentially perfect normal alignment even with small  $k$ . So the samples are nearly on the horizontal line.
- (2) *Slow-spectrum initialization*: if  $A_{0,2}$  is aligned with the smallest positive eigenvalue's eigenspace and  $A_{0,2} = \frac{1}{\lambda_r} u_r$ . Then  $\mathcal{L}_{\text{MM}}^{\perp} = \frac{1}{\lambda_r} (1 - 2\eta\lambda_r)^{2k}$ . In this case, normal alignment can be poor when  $k$  is small. As  $k$  increases, the gap from samples to the horizontal ridge decreases at the slow geometric rate determined by  $\lambda_r$ .

In contrast, the architecture-driven error is purely tangential: the normal component  $\text{Err}_{\text{arc}}^{\perp} = 0$ , while the tangent component  $\text{Err}_{\text{arc}}^{\parallel} = \int_{\delta}^T \frac{w(t)}{h_t^2} \mathbb{E}_{x \sim p_t} [f_t(x_1)^2] dt - \tilde{v}^T \tilde{U}^+ \tilde{v}$  which is strictly positive at finite  $p$ . Consequently, the normal error is much smaller than the tangential error, leading to strong normal alignment to the ridge but persistent tangential spreading along it. The samples therefore form an edge-like interpolation between the two points. As  $p$  grows, the tangential architecture floor shrinks, and the slide stage increasingly concentrates samples near the two centers, yielding memorization-like behavior in this toy example.

## 5 Experiments

In this section, we provide numerical experiments to validate theoretical insights gathered from the previous sections. Due to space constraints, we defer details of experimental setups to Appendix I.

### 5.1 Synthetic Data - Two Points in 2D Plane

**Numerical Verification of Geometric Biases.** As the reach-align-slide characterization in Section 3 are independent of training architectures, we first quantitatively validate it on a 2D dataset  $\mathcal{D} = \{(-3, 0), (3, 0)\}$ , using both RFNN and MLP architectures with different training weights  $w(t) \in \{1, h_t, h_t^2\}$ : we explicitly track the directional error bounds in Theorems 3.2, 3.3, and compare to the generated sample configurations. Note that in this setup, the ridge manifold is the horizontal. The tangent and normal directions are explicitly given by  $e_1 = (1, 0)$  and  $e_2 = (0, 1)$ .

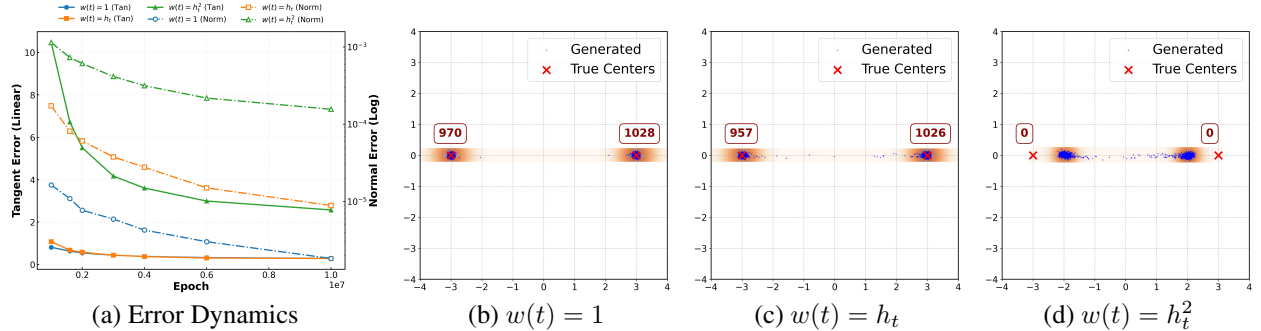


Figure 2: **Error dynamics and generated samples of RFNN.** (a) Evolution of tangential errors (solid lines, left axis, linear scale) and normal errors (dash-dot lines, right axis, log scale) during training. (b)–(d) Comparison of generated sample configurations under different weighting schedules. Boxed numbers indicate sample counts around the target modes (radius = 0.5). The background color represents the KDE plot.

As shown in Figures 2(a) and 3(a), the evolution of the directional errors aligns closely with the generation geometry. Specifically, the normal error bound in Theorem 3.2 yields a tight upper bound: it matches

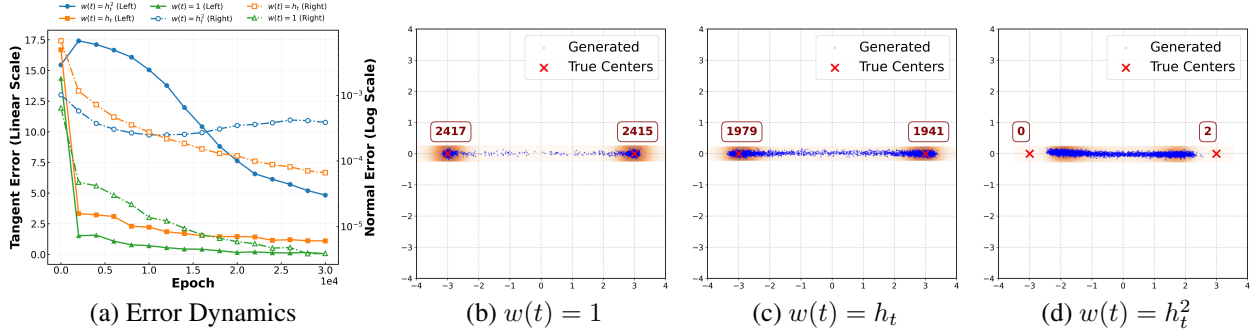


Figure 3: **Error dynamics and generated samples of MLP.** (a) Evolution of tangential errors (solid lines, left axis, linear scale) and normal errors (dash-dot lines, right axis, log scale) during training. (b)–(d) Comparison of generated sample configurations under different weighting schedules. Boxed numbers indicate sample counts around the target modes (radius = 0.5). The background color represents the KDE plot.

the observed concentration of samples near  $y = 0$ ; similarly, the tangent error bound in Theorem 3.3 correctly predicts the magnitudes of sample spread. This consistent agreement across different architectures and weight schedules confirms the validity of our analysis in Section 3.

The formation of the ‘edge’ in generation (Figures 2,3(c)–(d)) is explained by the magnitude disparity between the directional error bounds derived in Theorems 3.2 and 3.3. As shown in panel (a) of Figures 2 and 3, the normal errors remain small throughout training, effectively keeping samples near ridge manifold ( $y = 0$ ). In contrast, the tangent errors fail to vanish and settle at positive floors, which prevents samples from converging to the training data, driving them to spread along the line segment as seen in panels (b)–(d). The larger is the tangent-error floor, the more spreadout are the samples on the ridge, leading to a more pronounced ‘edge’ structure in generation.

Furthermore, the generation geometry along the tangent direction is highly sensitive to the weighting schedule  $w(t)$ . For both models, the empirical results align with our predictions in Remark 3.1:  $w(t) = 1$  produces the smallest tangent errors, while  $w(t) = h_t$  and  $w(t) = h_t^2$  lead to progressively larger errors. Consequently, a smaller tangent error results in more concentrated samples around data points, as demonstrated by the sample counts in boxed regions of panels (b)–(d).

**From Training Dynamics to Inference Error.** In this part, we experimentally validate the theoretical connection between training error  $\mathcal{L}_{\text{MM}}$  and generation geometry established in Theorem 4.1. Under the same setting, Figure 4 tracks the evolution of directional training loss for different weight schedules. The

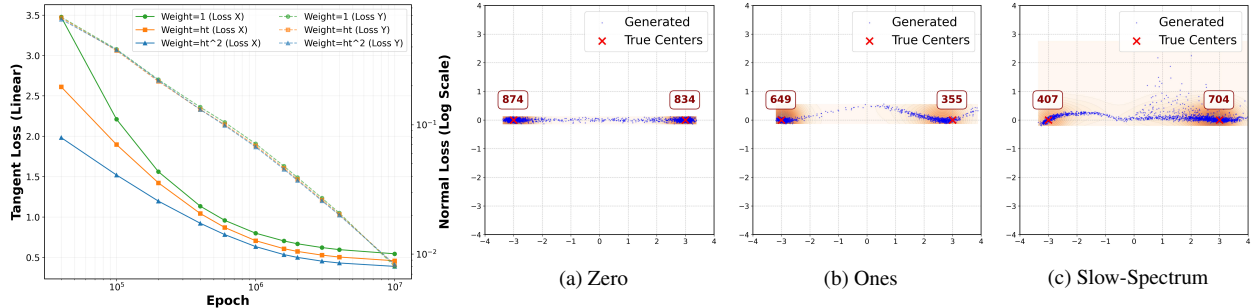


Figure 4: **Loss Decomposition of RFNN.** Evolution of tangent and normal loss components ( $w(t) = 1, h_t, h_t^2$ ) for the RFNN.

Figure 5: **Initialization Effects (Epoch 40k).** Comparison of generated samples under (a) zero (b) all-ones and (c) slow-spectrum initializations. The colored shading denotes the KDE of the distribution.

normal loss  $\mathcal{L}_{\text{MM}}^\perp(A)$  (dashed lines, right-axis, log-scale) remains consistently low. Combined with the robust coefficient  $C_\delta^\perp$ , the normal-error bound predicted by Theorem 4.1 remains small under all three weight schedules, consistent with the observed generation near ridge. In contrast, tangential behavior is

affected by the interplay between tangential loss  $\mathcal{L}_{\text{MM}}^{\parallel}(A)$  and constant  $C_{\delta}^{\parallel}$ . For  $w(t) = h_t^2$  (blue line in Figure 4), this schedule yields the lowest training loss. However, since  $w(\delta) \approx \delta^2$ , the sensitivity coefficient explodes as  $C_{\delta}^{\parallel} \approx \frac{\delta}{\delta^2} \propto \delta^{-1}$ . This massive amplification dominates the tangent-error bound in (11), causing the significant ‘edge’ effect in generation. For  $w(t) = 1$  (green line in Figure 4), it yields the highest training loss. Yet, with  $w(\delta) = 1$ , the coefficient remains small ( $C_{\delta}^{\parallel} \approx \delta^{1/2}$ ), effectively suppressing tangential error, which is consistent with the observed memorization effect in this setting.

**Biases of Different Initializations.** Our results in Section 4.3 demonstrate that the generation geometry is highly sensitive to the initialization of GD in the RFNN. In Figure 5, we compare the generation geometries with finite training time (40K epoch) under three initialization schemes: *Zeros* ( $A_0 = 0$ ), *Ones* ( $A_0 = 1$ ), and *Slow-spectrum* (first row Gaussian and second row aligning with small eigenvalue ( $\approx 10^{-5}$ )). With *Zeros* initialization, the generated samples remain strictly on the horizontal line. In contrast, for both *Ones* and *Slow-spectrum* initializations, samples form an ‘arch’ shape. This observation directly validates our analysis in Section 4.3: the transient ‘arch’ emerges because the normal alignment is still in progress (due to finite training time) but slow, a behavior precisely predicted by the slow geometric convergence rate in our Theorem 4.2.

## 5.2 More Points in 2D

We present two 2D examples where generation geometries are nontrivial while our proposed log-density ridges still predict the generalization appropriately (see Appendix J.1 for more examples).

We first present a case where the target distribution is supported at  $(\pm 1, \pm 1)$ . Figure 6 shows sample configurations and moving ridges, illustrating how the ridge structure aligns with generalization. Notably, generalization concentrates on low-dimensional ‘edges’ not present in the training set. While some might consider this straightforward and think generalization happens via straight line ‘mode interpolation’, our second example shows this isn’t always true: ridges can be ‘bent’ instead. This is shown in Figure 7, with the target distribution supported at  $(0, 0)$ ,  $(3, 0)$ , and  $(0, 5)$ .

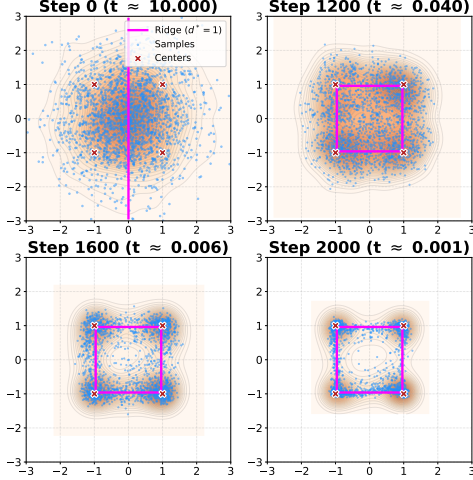


Figure 6: Generalization from 4 training points.

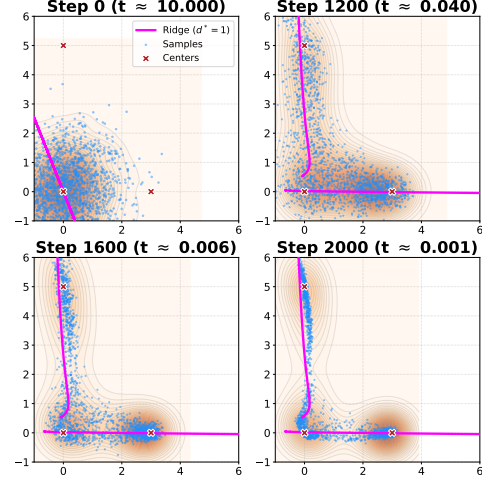


Figure 7: Generalization from 3 training points.

## 5.3 Higher Dimension Data - MNIST

In this section, we test on MNIST to study geometric convergence toward the ridge manifold  $\mathcal{R}_{d^*}$ . We aim to identify the two stages in our theory: *normal alignment* and *tangential sliding*. By tracking normal/tangential errors, we show that the model spends most time in normal alignment, leaving little time for tangential

sliding toward data samples, which naturally yields generalization. For sampling trajectories of MNIST, please refer to Appendix J.2.

**Experimental Setup.** We evaluate our method on a binary MNIST subset (digits 4 and 8). To reduce complexity, we first train a VAE with MLP encoder and decoder to embed images  $\mathbf{x} \in \mathbb{R}^{784}$  into a 32-dimensional latent space  $\mathcal{Z} \subset \mathbb{R}^{32}$ . Details are in Appendix I.3.

**Normal Alignment.** Since the distribution of the MNIST dataset in latent space is unknown, we derive an estimator via Newton’s method to compute distance to the manifold (in latent space):  $\hat{d}_{\text{Newton}}(x) = \|\Lambda_{\perp}(x)^{-1} E(x)^\top \nabla \log p(x)\|$ . The detailed derivation is provided in Appendix I.4. We compute the mean normal distance by averaging over 2,000 inference trajectories, as shown in Figure 8(a). We observe that the evolution of generation along the normal direction is roughly divided into three stages. *Steps 0-200*: the process is dominated by pure Gaussian noise, resulting no distance-decay. *Steps 200-800*: samples are pulled towards the ridge  $\mathcal{R}_{d^*}$ , corresponding to the align-stage in our theory. *Steps 800-1000*: the distance curve plateaus, corresponding to end of normal alignment due to reaching the normal-error floor.

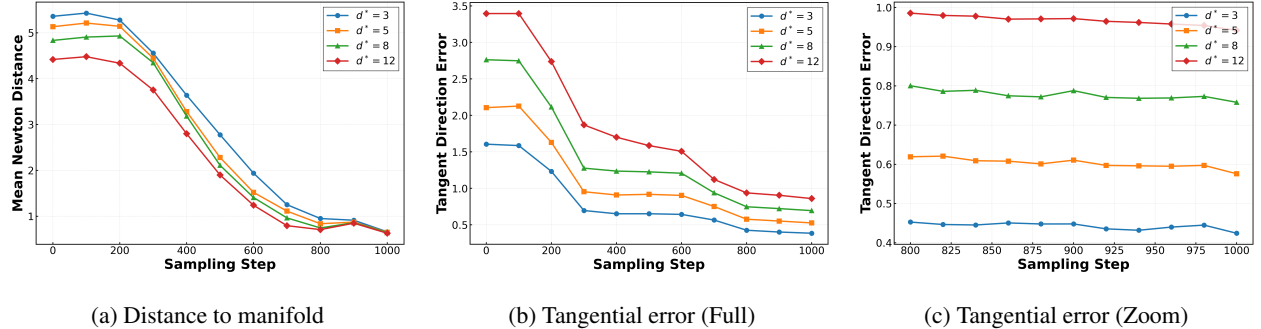


Figure 8: **Evolution of Ridge Manifold metrics during inference.** (a) Mean Newton distance estimator  $\hat{d}_{\text{Newton}}(x)$  versus sampling steps for  $d^*$ . (b) Tangential error trajectories over the full sampling horizon. (c) Zoom-in of the tangential error in the final 200 steps.

**Tangential Sliding.** Figure 8(b) shows the averaged tangent-error (computed using (9)) over time. We observe that the tangent-errors experience multiple decaying stages with different rates. Together with the normal direction behavior, this could suggest the tangential sliding landscapes vary when samples approach ridges of different intrinsic dimensions  $d^*$ . In the last 200 steps (Figure 8(c)), tangential motion becomes negligible—samples cease sliding toward data and instead diffuse on ridges, enabling generalization.

## 6 Limitations

This article did not consider errors induced by (coarse) time discretization of the inference process, which could lead to additional changes to the normal and tangent distribution, but based on understandings of diffusion model discretization error that have been perfected over the years (Lee et al., 2022; De Bortoli, 2022; Chen et al., 2023b,a; Benton et al., 2024; Conforti et al., 2023; Wang et al., 2024), these changes are expected to be minor, unless the discretization time schedule corresponds to very large step sizes, for which little quantitative analysis exists so far.

## Acknowledgment

MT thanks Hongkai Zhao, Mikhail Belkin and Peter L. Bartlett for inspiring discussions.

## References

E. Aamari, J. Kim, F. Chazal, B. Michel, A. Rinaldo, and L. Wasserman. Estimating the reach of a manifold. 2019. (Cited on page 24.)

S. K. Aithal, P. Maini, Z. Lipton, and J. Z. Kolter. Understanding hallucinations in diffusion models through mode interpolation. *Advances in Neural Information Processing Systems*, 37:134614–134644, 2024. (Cited on page 2.)

R. Baptista, A. Dasgupta, N. B. Kovachki, A. Oberai, and A. M. Stuart. Memorization and regularization in generative diffusion models. *arXiv preprint arXiv:2501.15785*, 2025. (Cited on page 2.)

J. Benton, V. De Bortoli, A. Doucet, and G. Deligiannidis. Nearly d-linear convergence bounds for diffusion models via stochastic localization. In *The Twelfth International Conference on Learning Representations*, 2024. (Cited on page 12.)

Q. Bertrand, A. Gagneux, M. Massias, and R. Emonet. On the closed-form of flow matching: Generalization does not arise from target stochasticity. *arXiv preprint arXiv:2506.03719*, 2025. (Cited on page 2.)

T. Bonnaire, R. Urfin, G. Biroli, and M. Mézard. Why diffusion models don't memorize: The role of implicit dynamical regularization in training. *arXiv preprint arXiv:2505.17638*, 2025. (Cited on pages 2, 4, and 7.)

T. Brooks, B. Peebles, C. Holmes, W. DePue, Y. Guo, L. Jing, D. Schnurr, J. Taylor, T. Luhman, E. Luhman, et al. Video generation models as world simulators. *OpenAI Blog*, 1(8):1, 2024. (Cited on page 1.)

N. Carlini, J. Hayes, M. Nasr, M. Jagielski, V. Sehwag, F. Tramer, B. Balle, D. Ippolito, and E. Wallace. Extracting training data from diffusion models. In *32nd USENIX security symposium (USENIX Security 23)*, pages 5253–5270, 2023. (Cited on page 1.)

H. Chen, H. Lee, and J. Lu. Improved analysis of score-based generative modeling: User-friendly bounds under minimal smoothness assumptions. In *International Conference on Machine Learning*, pages 4735–4763. PMLR, 2023a. (Cited on page 12.)

S. Chen, S. Chewi, J. Li, Y. Li, A. Salim, and A. R. Zhang. Sampling is as easy as learning the score: theory for diffusion models with minimal data assumptions. *ICLR*, 2023b. (Cited on page 12.)

Y.-C. Chen, C. R. Genovese, and L. Wasserman. Asymptotic theory for density ridges. *The Annals of Statistics*, pages 1896–1928, 2015. (Cited on page 5.)

Z. Chen. On the interpolation effect of score smoothing. *arXiv preprint arXiv:2502.19499*, 2025. (Cited on page 2.)

G. Conforti, A. Durmus, and M. G. Silveri. Score diffusion models without early stopping: finite fisher information is all you need. *arXiv preprint arXiv:2308.12240*, 2023. (Cited on page 12.)

H. Cui, C. Pehlevan, and Y. M. Lu. A precise asymptotic analysis of learning diffusion models: theory and insights. *arXiv preprint arXiv:2501.03937*, 2025. (Cited on page 7.)

V. De Bortoli. Convergence of denoising diffusion models under the manifold hypothesis. *TMLR*, 2022. (Cited on page 12.)

P. Dhariwal and A. Nichol. Diffusion models beat gans on image synthesis. *Advances in neural information processing systems*, 34:8780–8794, 2021. (Cited on page 1.)

J. Duan, F. Kong, S. Wang, X. Shi, and K. Xu. Are diffusion models vulnerable to membership inference attacks? In *International Conference on Machine Learning*, pages 8717–8730. PMLR, 2023. (Cited on page 1.)

T. Faghly, P. Potaptchik, S. Howard, G. Deligiannidis, and J. Pidstrigach. Diffusion models and the manifold hypothesis: Log-domain smoothing is geometry adaptive. *arXiv preprint arXiv:2510.02305*, 2025. (Cited on page 2.)

C. R. Genovese, M. Perone-Pacifico, I. Verdinelli, and L. Wasserman. Nonparametric ridge estimation. 2014. (Cited on page 5.)

A. J. George, R. Veiga, and N. Macris. Denoising score matching with random features: Insights on diffusion models from precise learning curves. *arXiv preprint arXiv:2502.00336*, 2025. (Cited on pages 2 and 4.)

A. Han, W. Huang, Y. Cao, and D. Zou. On the feature learning in diffusion models. *ICLR*, 2025. (Cited on page 7.)

Y. He, K. Rojas, and M. Tao. Zeroth-order sampling methods for non-log-concave distributions: Alleviating metastability by denoising diffusion. *Advances in Neural Information Processing Systems*, 37:71122–71161, 2024. (Cited on page 28.)

J. Ho, A. Jain, and P. Abbeel. Denoising diffusion probabilistic models. *Advances in neural information processing systems*, 33:6840–6851, 2020. (Cited on page 1.)

Z. Kadkhodaie, F. Guth, E. P. Simoncelli, and S. Mallat. Generalization in diffusion models arises from geometry-adaptive harmonic representations. *arXiv preprint arXiv:2310.02557*, 2023. (Cited on page 1.)

M. Kamb and S. Ganguli. An analytic theory of creativity in convolutional diffusion models. *arXiv preprint arXiv:2412.20292*, 2024. (Cited on page 2.)

Z. Kong, W. Ping, J. Huang, K. Zhao, and B. Catanzaro. Diffwave: A versatile diffusion model for audio synthesis. *ICLR*, 2021. (Cited on page 1.)

H. Lee, J. Lu, and Y. Tan. Convergence for score-based generative modeling with polynomial complexity. *Advances in Neural Information Processing Systems*, 35:22870–22882, 2022. (Cited on page 12.)

G. Leobacher and A. Steinicke. Existence, uniqueness and regularity of the projection onto differentiable manifolds. *Annals of global analysis and geometry*, 60(3):559–587, 2021. (Cited on page 18.)

T. Li and K. He. Back to basics: Let denoising generative models denoise. *arXiv preprint arXiv:2511.13720*, 2025. (Cited on page 4.)

X. Li, Z. Shen, Y.-P. Hsieh, and N. He. When scores learn geometry: Rate separations under the manifold hypothesis. *arXiv preprint arXiv:2509.24912*, 2025. (Cited on page 2.)

Y. Liu, J. Huang, Y. Li, D. Wang, and B. Xiao. Generative ai model privacy: a survey. *Artificial Intelligence Review*, 58(1):33, 2024. (Cited on page 1.)

K. Moshksar. Refining concentration for gaussian quadratic chaos. *arXiv preprint arXiv:2412.03774*, 2024. (Cited on page 28.)

P. Niyogi, S. Smale, and S. Weinberger. Finding the homology of submanifolds with high confidence from random samples. *Discrete & Computational Geometry*, 39(1):419–441, 2008. (Cited on page 19.)

K. Shah, A. Kalavasis, A. R. Klivans, and G. Daras. Does generation require memorization? creative diffusion models using ambient diffusion. *arXiv preprint arXiv:2502.21278*, 2025. (Cited on page 2.)

J. Sohl-Dickstein, E. Weiss, N. Maheswaranathan, and S. Ganguli. Deep unsupervised learning using nonequilibrium thermodynamics. In *International conference on machine learning*, pages 2256–2265. pmlr, 2015. (Cited on page 1.)

G. Somepalli, V. Singla, M. Goldblum, J. Geiping, and T. Goldstein. Understanding and mitigating copying in diffusion models. *Advances in Neural Information Processing Systems*, 36:47783–47803, 2023. (Cited on page 1.)

Y. Song, J. Sohl-Dickstein, D. P. Kingma, A. Kumar, S. Ermon, and B. Poole. Score-based generative modeling through stochastic differential equations. *ICLR*, 2021. (Cited on page 1.)

J. J. Vastola. Generalization through variance: how noise shapes inductive biases in diffusion models. *arXiv preprint arXiv:2504.12532*, 2025. (Cited on page 2.)

Y. Wang, Y. He, and M. Tao. Evaluating the design space of diffusion-based generative models. *Advances in Neural Information Processing Systems*, 37:19307–19352, 2024. (Cited on pages 2, 7, and 12.)

Y.-H. Wu, P. Marion, G. Biau, and C. Boyer. Taking a big step: Large learning rates in denoising score matching prevent memorization. *arXiv preprint arXiv:2502.03435*, 2025. (Cited on page 2.)

Z. Ye, Q. Zhu, M. Tao, and M. Chen. Provable separations between memorization and generalization in diffusion models. *arXiv preprint arXiv:2511.03202*, 2025. (Cited on page 1.)

H. Zhang, J. Zhou, Y. Lu, M. Guo, P. Wang, L. Shen, and Q. Qu. The emergence of reproducibility and consistency in diffusion models. *arXiv preprint arXiv:2310.05264*, 2023. (Cited on page 1.)

# Contents

<b>1</b>	<b>Introduction</b>	<b>1</b>
<b>2</b>	<b>Preliminaries</b>	<b>3</b>
<b>3</b>	<b>Geometric Dynamical Properties of the Inference Process</b>	<b>4</b>
3.1	Data-dependent Manifolds - Log-density Ridge Sets . . . . .	5
3.2	Stage 1 - Reaching the Tube Neighborhood . . . . .	6
3.3	Stage 2 - Aligning along Normal Directions . . . . .	6
3.4	Stage 3 - Sliding along Tangent Directions . . . . .	6
<b>4</b>	<b>How Training Affects Generation: General Theory + an Explicit RF Example</b>	<b>7</b>
4.1	Directional Decomposition along Log-density Ridges . . . . .	7
4.2	Application in RF+GD . . . . .	8
4.3	RFNN for Two Points in 2D . . . . .	8
<b>5</b>	<b>Experiments</b>	<b>9</b>
5.1	Synthetic Data - Two Points in 2D Plane . . . . .	9
5.2	More Points in 2D . . . . .	11
5.3	Higher Dimension Data - MNIST . . . . .	11
<b>6</b>	<b>Limitations</b>	<b>12</b>
<b>A</b>	<b>Denoising Mean Matching Loss</b>	<b>17</b>
<b>B</b>	<b>Data-Independent Properties of the Log-density Ridge Sets</b>	<b>18</b>
<b>C</b>	<b>Data dependent Ridge Motion Estimations</b>	<b>21</b>
<b>D</b>	<b>Analysis of Stage 1</b>	<b>27</b>
<b>E</b>	<b>Analysis of Stage 2</b>	<b>30</b>
<b>F</b>	<b>Analysis of Stage 3</b>	<b>33</b>
<b>G</b>	<b>From Inference to Training</b>	<b>37</b>
<b>H</b>	<b>Analysis of the Training Process</b>	<b>39</b>
<b>I</b>	<b>Experimental Details</b>	<b>44</b>
I.1	Two Points in 2D Plane . . . . .	44
I.2	More Points in 2D Plane . . . . .	45
I.3	MNIST . . . . .	45
I.4	Derivation of the Newton Distance Estimator . . . . .	46
<b>J</b>	<b>More Experiment Results</b>	<b>46</b>
J.1	RFNN on Different Sets . . . . .	46
J.2	MNIST Trajectories . . . . .	53

## A Denoising Mean Matching Loss

In this section, we introduce the detailed derivation of the posterior mean-matching loss  $\mathcal{L}_{\text{MM}}$  and the denoising posterior mean-matching loss  $\mathcal{L}_{\text{DMM}}$ . According to Tweedie's formula that

$$\nabla \log p_t(x) = -\frac{x}{h_t} + \frac{\mathbb{E}[a_t X_0 | X_t = x]}{h_t} = -\frac{x}{h_t} + \frac{m(t, x)}{h_t},$$

to parametrize the score, it suffices to parametrize the posterior mean  $m$ . We denote the parametrization by  $m_A$ . Then the posterior mean matching loss  $\mathcal{L}_{\text{MM}}$  defined in (3) is equivalent to the score matching loss:

$$\begin{aligned}\mathcal{L}_{\text{MM}} &= \int_{\delta}^T \frac{w(t)}{h_t^2} \mathbb{E}[\|m_A(t, X_t) - m(t, X_t)\|^2] dt \\ &= \int_{\delta}^T w(t) \mathbb{E}\left[\left\|\frac{-X_t + m_A(t, X_t)}{h_t} - \frac{-X_t + m(t, X_t)}{h_t}\right\|^2\right] dt \\ &= \int_{\delta}^T w(t) \mathbb{E}[\|s_A(t, X_t) - \nabla \log p_t(X_t)\|^2] dt.\end{aligned}$$

However,  $\mathcal{L}_{\text{MM}}$  can't be evaluated directly using data from  $X_0$ . We can apply the same denoising trick as what's done for score matching loss.

$$\begin{aligned}\mathcal{L}_{\text{MM}} &= \int_{\delta}^T \frac{w(t)}{h_t^2} \mathbb{E}[\|m_A(t, X_t) - m(t, X_t)\|^2] dt \\ &= \int_{\delta}^T \frac{w(t)}{h_t^2} \mathbb{E}[\|m_A(t, X_t) - a_t X_0 + a_t X_0 - m(t, X_t)\|^2] dt \\ &= \int_{\delta}^T \frac{w(t)}{h_t^2} \mathbb{E}[\|m_A(t, X_t) - a_t X_0\|^2] dt + \int_{\delta}^T \frac{w(t)}{h_t^2} \mathbb{E}[\|m(t, X_t) - a_t X_0\|^2] dt \\ &\quad - 2 \int_{\delta}^T \frac{w(t)}{h_t^2} \mathbb{E}[\langle m_A(t, X_t) - a_t X_0, m(t, X_t) - a_t X_0 \rangle] dt \\ &= \mathcal{L}_{\text{DMM}} + C,\end{aligned}$$

where the last term in the third identity is canceled due to the definition of  $m$  and tower property. The second term in the third identity is a constant independent to the trained parameter  $A$ . Therefore, we can train to optimize  $\mathcal{L}_{\text{DMM}}$  directly. The DMM loss evolves two expectations and one integral:

$$\mathcal{L}_{\text{DMM}} = \int_{\delta}^T \frac{w(t)}{h_t^2} \mathbb{E}_{X_0} \mathbb{E}_z [\| -a_t X_0 + m_A(t, a_t X_0 + \sqrt{h_t} z) \|^2] dt.$$

Under data assumption 1 that  $p = \frac{1}{n} \sum_{i=1}^n \delta_{x_0^{(i)}}$ , the expectation  $\mathbb{E}_{X_0}$  can be exactly evaluated through empirical average over all training data, i.e.,

$$\mathcal{L}_{\text{DMM}} = \frac{1}{n} \sum_{i=1}^n \int_{\delta}^T \frac{w(t)}{h_t^2} \mathbb{E}_z [\| -a_t x_0^{(i)} + m_A(t, a_t x_0^{(i)} + \sqrt{h_t} z) \|^2] dt. \quad (12)$$

For the convenience of analysis, we focus on analyzing the loss defined in (12), which corresponds to exact evaluations for  $\mathbb{E}_z$  and integral in  $t$ .

In practice, the loss in (12) is used after further numerical approximations for  $\mathbb{E}_z$  and integral in  $t$ . The practical DMM loss is given by

$$\mathcal{L}_{\text{DMM}}^{m,N} = \frac{1}{nm} \sum_{i,j=1}^{n,m} \sum_{k=1}^N \frac{t_k - t_{k-1}}{h_{t_k}^2} \| -a_{t_k} x_0^{(i)} + m_A(t_k, a_{t_k} x_0^{(i)} + \sqrt{h_{t_k}} z^{(i,j)}) \|^2$$

where  $\{z^{(i,j)}\}_{1 \leq i \leq n, 1 \leq j \leq m}$  is a sequence of i.i.d. standard Gaussian vectors in  $\mathbb{R}^d$  and  $\delta = t_0 < t_1 < \dots < t_N = T$  are the time grids for numerical integration on  $[\delta, T]$ .

## B Data-Independent Properties of the Log-density Ridge Sets

In this section, we introduce properties of the log-density ridges that are independent to our data assumptions. We summarize them in the following Proposition.

**Proposition B.1.** *Under Assumption 2, for any  $\rho_t \in (0, r_t]$  and the tube neighborhood  $\mathcal{T}_t(\rho_t)$  given below*

$$\mathcal{T}_t(\rho_t) := \{x \in \mathbb{R}^d \mid \text{dist}(x, \mathcal{R}_t) \leq \rho_t\}, \quad (13)$$

*the nearest-point projection  $\Pi_t : \mathcal{T}_t(\rho_t) \rightarrow \mathcal{R}_t$  is well-defined and we have*

- (1)  $\Pi_t$  is  $C^1$  on  $\mathcal{T}_t(\rho_t)$ ;
- (2)  $\forall x \in \mathcal{T}_t(\rho_t)$ ,  $n_t(x) := x - \Pi_t(x)$  is in the normal space at  $\Pi_t(x)$ , i.e.  $n_t(x) \in N_{\Pi_t(x)}(\mathcal{R}_t)$ ;
- (3)  $\sup_{x \in \mathcal{T}_t(\rho_t)} \|\nabla \Pi_t(x)\| \leq \frac{1}{1 - \rho_t/r_t}$ ;
- (4) *the motion of  $\Pi_t$  is bounded: for any  $z \in \mathcal{R}_t$ , there exists a velocity field  $v_t \in N_z(\mathcal{R}_t)$  s.t.  $\sup_{x \in \mathcal{T}_t(\rho_t)} \|\partial_t \Pi_t\| \leq V_t + \frac{\rho_t}{1 - \rho_t/r_t} W_t$  where*

$$V_t = \sup_{z \in \mathcal{R}_t} \|v_t(z)\|, \quad W_t = \sup_{z \in \mathcal{R}_t, \|u\|=1} \|P^{\parallel}(z)(\nabla v_t(z)u)\|^3.$$

*Proof of Proposition B.1.* That  $\Pi_t$  is well-defined on  $\mathcal{T}_t(\rho_t)$  directly follows from Assumption 2. The  $C^1$  smoothness of  $\Pi_t$  in space follows from [Leobacher and Steinicke \(2021, Theorem 2\)](#). Property (2) follows from the optimality of the nearest-point:  $z = \Pi_t(x)$  minimizes  $\|x - z'\|^2$  over  $z' \in \mathcal{R}_t$ . Therefore, differentiating  $z' \mapsto \|x - z'\|^2$  along any tangent direction  $u \in T_z(\mathcal{R}_t)$  yields

$$D(\|x - z'\|^2)[u]|_{z'=z} = -2\langle x - z, u \rangle = -2\langle n_t(x), u \rangle = 0.$$

Therefore,  $n_t(x) \in N_z(\mathcal{R}_t)$ .

To prove (3), we first apply the explicit expression of  $\nabla \Pi_t(x)$  in [Leobacher and Steinicke \(2021, Theorem C\)](#):

$$\nabla \Pi_t(x) = (id_{T_{\Pi_t(x)}(\mathcal{R}_t)} - \|x - \Pi_t(x)\| S_{t, \Pi_t(x), v})^{-1} P^{\parallel}(\Pi_t(x)), \quad \theta = \frac{x - \Pi_t(x)}{\|x - \Pi_t(x)\|},$$

where  $S_{t, \Pi_t(x), \theta}$  is the shape operator in the normal direction  $\theta$ . According to Lemma B.1 and the linearity of  $S_{t, \Pi_t(x), \theta}$  in  $\theta$ , we have

$$\|\nabla \Pi_t(x)\| \leq \|(id_{T_{\Pi_t(x)}(\mathcal{R}_t)} - \|x - \Pi_t(x)\| S_{t, \Pi_t(x), v})^{-1} P^{\parallel}(\Pi_t(x))\|$$

---

<sup>3</sup>For any  $z \in \mathcal{R}_t$ , we use  $P^{\parallel}(z)$  (or  $P^{\perp}(z)$ ) to represent the orthogonal projection from  $\mathbb{R}^d$  to  $T_z(\mathcal{R}_t)$  (or  $N_z(\mathcal{R}_t)$ ).

$$\leq \|(id_{T_{\Pi_t(x)}(\mathcal{R}_t)} - S_{t,\Pi_t(x),\|x-\Pi_t(x)\|v})^{-1}\| \leq \frac{1}{1 - \|x - \Pi_t(x)\|/r_t} \leq \frac{1}{1 - \rho_t/r_t}.$$

Last, to prove (4), we first apply Lemma B.2 to show existence of the normal velocity field  $v_t$ . Then the estimation of  $\|\partial_t \Pi_t\|$  follows from the definition of  $V_t$  and Lemma B.3.  $\square$

**Definition B.1** (Shape Operator). *Let  $\Pi_{t,z}$  be the second fundamental form of  $\mathcal{R}_t$  at  $z \in \mathcal{R}_t$ . For  $\theta \in N_z(\mathcal{R}_t)$ , the shape operator in the direction of  $\theta$  is defined as  $S_{t,z,\theta} : T_z(\mathcal{R}_t) \rightarrow T_z(\mathcal{R}_t)$  is then defined as*

$$\langle S_{t,z,\theta} u, v \rangle = \langle \Pi_{t,z}(u, v), \theta \rangle, \quad \forall u, v \in T_z(\mathcal{R}_t).$$

**Lemma B.1.** *Under Assumption 2, for any  $z \in \mathcal{R}_t$  and  $\theta \in N_z(\mathcal{R}_t)$ , we have*

- (1) *the shape operator is bounded:  $\|S_{t,z,\theta}\| \leq \|\theta\|/r_t$ ;*
- (2) *if  $\|\theta\| \leq \rho_t < r_t$ , the operator  $L_{t,z,\theta} := id_{T_z(\mathcal{R}_t)} - S_{t,z,\theta}$  is invertible and*

$$\|L_{t,z,\theta}^{-1}\| \leq \frac{1}{1 - \|\theta\|/r_t}.$$

*Proof of Lemma B.1.* According to Niyogi et al. (2008, Proposition 6.1), under Assumption 2,  $\|\Pi_{t,z}\| \leq 1/r_t$  for all  $t$ . Therefore,  $\|S_{t,z,\theta}\| \leq \|\theta\|/r_t$  and hence  $\|L_{t,z,\theta}^{-1}\| = \|(id_{T_z(\mathcal{R}_t)} - S_{t,z,\theta})^{-1}\| \leq \frac{1}{1 - \|\theta\|/r_t}$ .  $\square$

**Lemma B.2.** *Fix  $t \in [\delta, T]$ . Let  $U \subset \mathbb{R}^{d^*}$  be open and  $\tilde{\Phi}_t : U \rightarrow \mathbb{R}^d$  be a  $C^1$ -family of  $C^2$  embeddings such that  $\tilde{\Phi}_t(U) \subset \mathcal{R}_t$  and  $\tilde{\Phi}_t$  is a local parametrization of  $\mathcal{R}_t$  along a given  $C^1$ -curve  $z(t) \in \mathcal{R}_t$ . Assume that  $z(t) = \tilde{\Phi}_t(\tilde{u}(t))$  for some  $C^1$ -curve  $\tilde{u}(t) \in U$ . Then there exists a  $C^1$ -family of local diffeomorphisms  $\psi_t : U' \rightarrow U$ . Then there exists a family of diffeomorphism  $\psi_t : U' \rightarrow U$  such that*

$$\Phi_t := \tilde{\Phi}_t \circ \psi_t : U' \rightarrow \mathcal{R}_t, \quad \partial_t \Phi_t(u) \perp T_{\Phi_t(u)}(\mathcal{R}_t), \quad \forall (t, u) \in [\delta, T] \times U'.$$

Consequently, the velocity field  $v_t(z) := \partial_t \Phi_t(u)$  for  $z = \Phi_t(u)$  is a well-defined  $C^0$  normal velocity field on  $\Phi(U')$ , i.e.,  $v_t(z) \in N_z(\mathcal{R}_t)$ . Moreover,  $v_t$  is intrinsic in the sense that it equals to the normal component of  $\partial_t \tilde{\Phi}_t$ :  $v_t(\Phi_t(u)) = P_{N_{\Phi_t(u)}}(\partial_t \tilde{\Phi}_t(\psi_t(u)))$ , and is therefore independent of the tangent reparametrization of the chart.

*Proof of Lemma B.2.* Define  $\tilde{v}_t(u) := \partial_t \tilde{\Phi}_t(u)$ . Since  $\tilde{\Phi}_t$  is an embedding,  $\nabla \tilde{\Phi}_t(u) : \mathbb{R}^{d^*} \rightarrow T_{\tilde{\Phi}_t(u)}(\mathcal{R}_t)$  is a linear isomorphism for each  $(t, u)$ . Let  $P^{\parallel}(\tilde{\Phi}_t(u))$  denote orthogonal projection onto  $T_{\tilde{\Phi}_t(u)}(\mathcal{R}_t)$ . Define a time-dependent vector field  $a_t$  on  $U$  by

$$\nabla \tilde{\Phi}_t(u) a_t(u) = -P^{\parallel}(\tilde{\Phi}_t(u)) \tilde{v}_t(u) \in T_{\tilde{\Phi}_t(u)}(\mathcal{R}_t). \quad (14)$$

Since  $\nabla \tilde{\Phi}_t(u)$  is invertible on  $T_{\tilde{\Phi}_t(u)}(\mathcal{R}_t)$ ,  $a_t(u)$  in (14) is uniquely defined. Furthermore, under our assumptions,  $(t, u) \mapsto \nabla \tilde{\Phi}_t(u)$  and  $(t, u) \mapsto P^{\parallel}(\tilde{\Phi}_t(u)) \tilde{v}_t(u)$  are continuous in  $t$  and smooth in  $u$ , hence  $(t, u) \mapsto a_t(u)$  is also continuous in  $t$  and smooth in  $u$ .

Pick an open set  $U' \subset U$  that contains  $\tilde{u}(t)$  for all  $t \in [\delta, T]$ . Consider the ODE

$$\partial_t \psi_t(u) = a_t(\psi_t(u)), \quad \psi_\delta(u) = u \in U'. \quad (15)$$

Due to the regularity of  $a_t(\cdot)$ , there exists a unique solution  $\psi_t$  for all  $t \in [\delta, T]$  and  $\psi_t$  is a diffeomorphism for each  $t$ .

Now apply chain rule and we get

$$\begin{aligned}
\partial_t \Phi_t(u) &= \partial_t(\tilde{\Phi}_t \circ \psi_t)(u) = \tilde{v}_t(\psi_t(u)) + \nabla \tilde{\Phi}_t(\psi_t(u)) \partial_t \psi_t(u) \\
&= \tilde{v}_t(\psi_t(u)) + \nabla \tilde{\Phi}_t(\psi_t(u)) a_t(\psi_t(u)) = \tilde{v}_t(\psi_t(u)) - P^{\parallel}(\tilde{\Phi}_t(\psi_t(u))) \tilde{v}_t(\psi_t(u)) \\
&= P^{\perp}(\tilde{\Phi}_t(\psi_t(u))) \tilde{v}_t(\psi_t(u)),
\end{aligned}$$

where the second last identity follows from (14) and  $P^{\perp}(\tilde{\Phi}_t(\psi_t(u))) = I - P^{\parallel}(\tilde{\Phi}_t(\psi_t(u)))$  is the normal projection. Therefore,  $\partial \Phi_t(u) \perp T_{\tilde{\Phi}_t(\psi_t(u))}(\mathcal{R}_t)$ . Last,  $v_t(z) := \partial \Phi_t(u) \in N_{\tilde{\Phi}_t(\psi_t(u))}(\mathcal{R}_t)$  with  $z = \Phi_t(u)$  is well-defined on  $\Phi_t(U')$  and we can check that  $v_t(\Phi_t(u))$  is exactly the normal component of  $\partial_t \tilde{\Phi}_t(\psi_t(u))$ , hence independent to the tangent reparametrization.  $\square$

**Lemma B.3.** *For  $t \in [\delta, T]$ , let  $x \in \mathcal{T}_t(\rho_t)$  and  $z(t) := \Pi_t(x)$ . Under conditions in Lemma B.2 and Assumption 2, there exists a reparametrization chart  $\Phi_t$  in normal gauge and a  $C^1$  curve  $u(t) \in U \subset \mathbb{R}^{d^*}$  such that  $z(t) = \Phi_t(u(t))$  and*

$$\partial_t \Pi_t(x) = v_t(z(t)) + \tau_t, \quad v_t(z(t)) \in N_{z(t)}(\mathcal{R}_t) \text{ and } \tau_t := \nabla_u \Phi_t(u(t)) \partial_t u(t) \in T_{z(t)}(\mathcal{R}_t).$$

Furthermore,  $\|\tau_t\| \leq \frac{\rho_t}{1-\rho_t/r_t} W_t$ .

*Proof of Lemma B.3.* The existence of  $\Phi_t$  follows from Lemma B.2. Next, differentiate  $z(t) = \Phi_t(u(t))$  and we get

$$\partial_t z(t) = \partial_t \Phi_t(u(t)) + \nabla_u \Phi_t(u(t)) \partial_t u(t) = v_t(z) + \tau_t.$$

To prove the bound for  $\|\tau_t\|$ , we consider the local tangent frame  $\{E_i(t)\}_{i=1}^{d^*}$  along  $z(t)$  induced by the chart  $u \mapsto \Phi_t(u)$ . Since  $n_t(x) = x - z(t) \perp T_{z(t)}(\mathcal{R}_t)$ , we have  $\langle n_t(x), E_i(t) \rangle = 0$  for all  $1 \leq i \leq d^*$ . Differentiate wrt  $t$  on both sides and we get

$$0 = -\langle \partial_t z(t), E_i(t) \rangle + \langle n_t(x), \partial_t E_i(t) \rangle.$$

Decompose  $\partial_t z(t) = v_t(z(t)) + \tau_t$  and use the fact that  $v_t(z(t)) \perp T_{z(t)}(\mathcal{R}_t)$ , and we get

$$\langle \tau_t, E_i(t) \rangle = \langle n_t(x), \partial_t E_i(t) \rangle. \tag{16}$$

Using the local frame we can compute  $\partial_t E_i(t)$  as follows. Since  $E_i(t) = \partial_{u_i} \Phi_t(u(t))$ , we have

$$\begin{aligned}
\partial_t E_i(t) &= \partial_{u_i} \partial_t \Phi_t(u(t)) + \sum_{j=1}^{d^*} \partial_{u_i u_j}^2 \Phi_t(u(t)) \partial_j u(t) \\
&= \partial_{u_i} (v_t \circ \Phi_t)(u(t)) + \sum_{j=1}^{d^*} P^{\perp}(z)(\partial_{u_i u_j}^2 \Phi_t(u(t))) \partial_t u_j(t) + \sum_{j=1}^{d^*} P^{\parallel}(z)(\partial_{u_i u_j}^2 \Phi_t(u(t))) \partial_t u_j(t) \\
&= \nabla v_t(z) E_i(t) + \sum_{j=1}^{d^*} \Pi_{t,z}(E_i(t), E_j(t)) \partial_t u_j(t) + \sum_{j=1}^{d^*} P^{\parallel}(z)(\partial_{u_i u_j}^2 \Phi_t(u(t))) \partial_t u_j(t).
\end{aligned}$$

Since  $n_t(x) \in N_{z(t)}(\mathcal{R}_t)$ , we have

$$\begin{aligned}
\langle n_t(x), \partial_t E_i(t) \rangle &= \langle n_t(x), \nabla v_t(z(t)) E_i(t) \rangle + \langle n_t(x), \Pi_{t,z}(E_i(t), \sum_j \partial_t u_j(t) E_j(t)) \rangle \\
&= \langle n_t(x), \nabla v_t(z(t)) E_i(t) \rangle + \langle S_{t,z,n_t(x)} \tau_t, E_i(t) \rangle,
\end{aligned}$$

where the last identity follows from the definition of shape operator and  $\tau_t = \sum_j \partial_t u_j(t) E_j(t)$ . Plug the above equation into (16) and we get that restricted to the tangent space  $\mathcal{T}_{z(t)}(\mathcal{R}_t)$ ,

$$(I - S_{t,z,n_t(x)})\tau_t = P^{\parallel}(z(t))(\nabla v_t(z(t)))^{\top} n_t(x).$$

Therefore, according to Lemma B.1, the definition of  $W_t$  and the fact that  $x \in \mathcal{T}_t(\rho_t)$ ,

$$\|\tau_t\| \leq \|L_{t,z,n_t(x)}^{-1}\| \|\nabla v_t(z(t))\| \|n_t(x)\| \leq \frac{\rho_t}{1 - \rho_t/r_t} W_t.$$

□

## C Data dependent Ridge Motion Estimations

In this section, we provided some data-dependent estimations for quantities related to dynamical properties of the log-density ridges.

**Proposition C.1.** *Under Assumption 1, the log-density ridge sets satisfy Assumption 2. Furthermore, when  $t \rightarrow \delta^+ \ll 1$ , we have the following order estimations:*

$$r_t = \Omega(\beta_t h_t^3 \theta_t^{-1} R^{-3}), \quad V_t = \mathcal{O}(\beta_t^{-1} h_t^{-1} R), \quad W_t = \mathcal{O}(\beta_t^{-1} h_t^{-1} R r_t^{-1}),$$

where  $\theta_t$  is arbitrarily with order  $\theta_t = \exp(-o(h_t^{-1}))$ .

**Remark C.1** (Order estimation of ridge motion). *Combining Propositions B.1 and C.1, picking  $\rho_t = \Theta(r_t)$  and  $\beta_t = \Theta(1/h_t)$ , we proved Proposition 3.1-(3):  $\sup_{x \in \mathcal{T}_t(\rho_t)} \|\partial_t \Pi_t(x)\| = \mathcal{O}(R)$ .*

To study the relation between the data Assumption 1 and properties of the data-dependent manifold  $\mathcal{R}_t$ . The key is to estimate the derivatives of the score  $\nabla \log p_{T-t}(\cdot)$  in different regions dominated by centers  $\{m_{T-t}^{(i)} := a_{T-t} x_0^{(i)}\}_{i=1}^n$ . For each  $i \in [n]$  and  $|\theta_s| < 1$  for any  $\zeta > 0$  when  $s \rightarrow 0^+$ , define the center- $i$  dominate region

$$\mathcal{B}_{T-t}^{(i)}(\theta_{T-t}) := \{x \in \mathbb{R}^d \mid \text{Softmax}\left(-\frac{\|x - a_{T-t} x_0^{(i)}\|^2}{2h_{T-t}}\right)_i \geq 1 - \theta_{T-t}\}. \quad (17)$$

Next, we introduce a sufficient condition for  $x \in \mathcal{B}_{T-t}^{(i)}(\theta_{T-t})$ .

**Lemma C.1.** *For any  $x \in \mathbb{R}^d$  and  $\theta_{T-t} \in (0, \frac{1}{2})$ , if*

$$\|x - m_{T-t}^{(j)}\|^2 - \|x - m_{T-t}^{(i)}\|^2 \geq 2h_{T-t} \log\left(\frac{(1 - \theta_{T-t})(n - 1)}{\theta_{T-t}}\right), \quad \forall j \neq i, \quad (18)$$

then  $x \in \mathcal{B}_{T-t}^{(i)}(\theta_{T-t})$ .

**Remark C.2.** *As  $t \rightarrow T^-$ , if  $h_{T-t} = o(1)$  and  $\theta_{T-t} = \exp(-o(h_{T-t}^{-1}))$ , then RHS of (18) is of order  $o(1)$ . Therefore,  $Y_t$  (or  $\tilde{Y}_t$ ) satisfies the (18) with probability 1 as  $t \rightarrow T^-$ . As a consequence of Lemma C.1,  $Y_t \in \mathcal{B}_{T-t}^{(i)}(\theta_{T-t})$  (or  $\tilde{Y}_t \in \mathcal{B}_{T-t}^{(i)}(\theta_{T-t})$ ) with probability 1 as  $t \rightarrow T^-$ .*

*Proof of Lemma C.1.* Under (18), we have that for all  $j \neq i$ ,

$$\frac{\text{Softmax}\left(-\frac{\|x - m_{T-t}\|^2}{2h_{T-t}}\right)_j}{\text{Softmax}\left(-\frac{\|x - m_{T-t}\|^2}{2h_{T-t}}\right)_i} = \exp\left(-\frac{\|x - m_{T-t}^{(j)}\|^2 - \|x - m_{T-t}^{(i)}\|^2}{2h_{T-t}}\right) \leq \frac{\theta_{T-t}}{(1 - \theta_{T-t})(n - 1)}.$$

Therefore,

$$\begin{aligned} & 1 - \text{Softmax}\left(-\frac{\|x - m_{T-t}\|^2}{2h_{T-t}}\right)_i \\ &= \sum_{j \neq i} \text{Softmax}\left(-\frac{\|x - m_{T-t}\|^2}{2h_{T-t}}\right)_j \leq \frac{\theta_{T-t}}{(1 - \theta_{T-t})} \text{Softmax}\left(-\frac{\|x - m_{T-t}\|^2}{2h_{T-t}}\right)_i. \end{aligned}$$

The statement follows from the definition of  $\mathcal{B}_{T-t}^{(i)}(\eta_{T-t})$ .  $\square$

Now we provide estimates of derivatives of the score on the center-dominate regions.

**Lemma C.2.** *For any  $t \in [\delta, T]$ , we have*

$$\sup_{x \in \cup_{i=1}^n \mathcal{B}_t^{(i)}(\theta_t)} \|\nabla m(t, x)\| \leq \frac{20a_t^2 \theta_t R^2}{h_t}, \quad \sup_{x \in \cup_{i=1}^n \mathcal{B}_t^{(i)}(\theta_t)} \|\nabla^3 \log p_t(x)\| \leq \frac{80a_t^3 \theta_t R^3}{h_t^3},$$

where  $\mathcal{B}_t^{(i)}(\theta_t)$  is defined in (17) with any  $\theta_t = \exp(-o(h_t^{-1}))$ .

**Remark C.3** (Choice of  $\beta_t$ ). *Lemma C.2 also validates the choice of ridge threshold  $\beta_t = \Theta(1/h_t)$  when  $t \rightarrow 0^+$ . According to Lemma C.3,  $\nabla^2 \log p_t(x) = -\frac{1}{h_t} I_d + \frac{1}{h_t^2} \Sigma(t, x)$ . According to estimations in Lemma C.2, each eigenvalue  $\lambda_j(t, x)$  of  $\nabla^2 \log p_t(x)$  satisfies*

$$\lambda_j(t, x) \leq -\frac{1}{h_t} + \frac{20a_t^2 \theta_t R^2}{h_t^2} \leq -\frac{c}{h_t}, \quad \frac{1}{2} < c < 1,$$

under some choice of  $\theta_t = \exp(-o(h_t^{-1}))$ . Therefore, as  $t \rightarrow 0^+$ , the choice of  $\beta_t = c/h_t$  makes the second condition in the log-density ridge definition automatically satisfied.

*Proof of Lemma C.2.* According to Lemma C.3, for all  $x \in \mathcal{B}_t^{(i)}(\theta_t)$

$$\|\nabla m(t, x)\| = \frac{1}{h_t} \|\Sigma(t, x)\| \leq \frac{1}{h_t} \sum_{j=1}^n \text{Softmax}\left(-\frac{\|x - a_t x_0\|^2}{2h_t}\right)_j \|a_t x_0^{(j)} - m(t, x)\|^2.$$

Notice that for  $j = i$ ,

$$\begin{aligned} \|a_t x_0^{(i)} - m(t, x)\| &= \|a_t x_0^{(i)} - \sum_{j'=1}^n \text{Softmax}\left(-\frac{\|x - a_t x_0\|^2}{2h_t}\right)_{j'} a_t x_0^{(j')}\| \\ &\leq \sum_{j' \neq i} \text{Softmax}\left(-\frac{\|x - a_t x_0\|^2}{2h_t}\right)_{j'} \|a_t x_0^{(j')} - a_t x_0^{(i)}\| \leq 2a_t \theta_t R. \end{aligned}$$

For  $j \neq i$ , we have

$$\|a_t x_0^{(j)} - m(t, x)\| \leq \|a_t x_0^{(i)} - m(t, x)\| + \|a_t x_0^{(i)} - a_t x_0^{(j)}\| \leq 2a_t(\theta_t + 1)R \leq 4a_t R.$$

Combining the above estimations and we get

$$\begin{aligned} & \|\nabla m(t, x)\| \\ &\leq \frac{1}{h_t} \text{Softmax}\left(-\frac{\|x - a_t x_0\|^2}{2h_t}\right)_i (2a_t \theta_t R)^2 + \frac{1}{h_t} \left( \sum_{j \neq i} \text{Softmax}\left(-\frac{\|x - a_t x_0\|^2}{2h_t}\right)_j \right) (4a_t R)^2 \end{aligned}$$

$$\leq \frac{20a_t^2\theta_t R^2}{h_t}.$$

Following the same approach, we can bound  $\|\nabla^3 \log p_t(x)\|$  for  $x \in \mathcal{B}_t^{(i)}(\theta_t)$ :

$$\begin{aligned} & \|\nabla^3 \log p_t(x)\| \\ & \leq \frac{1}{h_t^3} \sum_{j=1}^n \text{Softmax}\left(-\frac{\|x - a_t x_0\|^2}{2h_t}\right)_j \|a_t x_0^{(j)} - m(t, x)\|^3 \\ & \leq \frac{1}{h_t^3} (\text{Softmax}\left(-\frac{\|x - a_t x_0\|^2}{2h_t}\right)_i) (2a_t \theta_t R)^3 + \frac{1}{h_t^3} \left(\sum_{j \neq i} \text{Softmax}\left(-\frac{\|x - a_t x_0\|^2}{2h_t}\right)_j\right) (4a_t R)^3 \\ & \leq \frac{80a_t^3 \theta_t R^3}{h_t^3}. \end{aligned}$$

□

Now we introduce the proof of Proposition C.1.

*Proof of Proposition C.1.* According to Lemma C.4, we have

$$\sup_{z \in \mathcal{R}_t} \|\Pi_{t,z}\| \leq \frac{1}{\beta_t} \sup_{z \in \mathcal{R}_t} \|\nabla^3 \log p_t(z)\|.$$

Since reach is at least the reciprocal of maximal curvature, we derive that

$$r_t \gtrsim \beta_t \left( \sup_{z \in \mathcal{R}_t} \|\nabla^3 \log p_t(z)\| \right)^{-1}.$$

As  $t \rightarrow 0^+$ , according to Lemma C.1 and definition of  $\mathcal{B}_t^{(i)}(\theta_t)$ ,  $x \in \cup_{i=1}^n \mathcal{B}_t^{(i)}(\theta_t)$  with probability 1 and  $\cup_{i=1}^n \mathcal{B}_t^{(i)}(\theta_t) \rightarrow \mathbb{R}^d$ . Therefore, as  $t \rightarrow 0^+$ , we have

$$r_t \gtrsim \beta_t \left( \sup_{z \in \mathcal{R}_t} \|\nabla^3 \log p_t(z)\| \right)^{-1} \gtrsim \beta_t \left( \sup_{x \in \cup_{i=1}^n \mathcal{B}_t^{(i)}(\theta_t)} \|\nabla^3 \log p_t(x)\| \right)^{-1} = \Omega\left(\frac{\beta_t h_t^3}{\theta_t R^3}\right),$$

for any  $\theta_t = \exp(-o(h_t^{-1}))$  and the last estimation follows from Lemma C.2.

To bound  $V_t$ , recall that  $V_t = \sup_{z \in \mathcal{R}_t} \|v_t(z)\|$  with  $v_t(z)$  being the velocity field induced by the normal gauge in Lemma B.2.

According to Lemma C.5,

$$\begin{aligned} v_t(z) &= -(E_t(z) \nabla^2 \log p_t(z) E_t(z))^{-1} E_t(z)^\top \partial_t \nabla \log p_t(z) \\ &= -(E_t(z) \nabla^2 \log p_t(z) E_t(z))^{-1} \frac{1}{h_t} E_t(z)^\top \partial_t m(t, z), \end{aligned}$$

where the last identity follows from Lemma C.6. Therefore,

$$\begin{aligned} V_t &\leq \sup_{z \in \mathcal{R}_t} \|v_t(z)\| \\ &\leq \frac{1}{h_t} \sup_{z \in \mathcal{R}_t} \|(E_t(z) \nabla^2 \log p_t(z) E_t(z))^{-1}\| \|E_t(z)^\top \partial_t m(t, z)\| \\ &\leq \frac{1}{\beta_t h_t} \sup_{z \in \mathcal{R}_t} \|E_t(z)^\top \partial_t m(t, z)\|, \end{aligned}$$

where the last inequality follows from the estimate in the proof of Lemma C.5. Hence according to Lemma C.7,  $V_t = \mathcal{O}(\frac{R}{h_t \beta_t})$ .

Last, to bound  $W_t$ , recall that  $W_t = \sup_{z \in \mathcal{R}_t, \|u\|=1} \|P^\parallel(z)(\nabla v_t(z)u)\|$ . Notice that  $v_t(z) \in N_z(\mathcal{R}_t)$ . Hence  $P^\perp(z)v_t(z) = v_t(z)$ . Differentiate both sides of the equation at  $z$  along direction  $u$ , we have

$$\begin{aligned} & (\nabla_u P^\perp(z))v_t(z) + P^\perp(z)\nabla_u v_t(z) = \nabla_u v_t(z) \\ \implies & (\nabla_u P^\perp(z))v_t(z) = (I - P^\perp(z))\nabla_u v_t(z) = P^\parallel(z)\nabla_u v_t(z). \end{aligned}$$

Therefore, we immediately obtain

$$W_t \leq \left( \sup_{z \in \mathcal{R}_t, \|u\|=1} \|\nabla_u P^\perp(z)\| \right) V_t$$

Next, we bound  $\|\nabla_u P^\parallel(z)\|$ . Notice that  $P^\parallel(z) + P^\perp(z) = I_d$ , hence  $\|\nabla_u P^\parallel(z)\| = \|\nabla_u P^\perp(z)\|$ . Now we start from  $P^\perp(z)^2 = P^\perp(z)$ , taking the directional derivative on both side, left multiplying  $P^\parallel(z)$  and right multiplying  $P^\parallel(z)$ ,

$$P^\parallel(z)(\nabla_u P^\parallel(z))P^\parallel(z) + P^\parallel(z)(\nabla_u P^\parallel(z))P^\parallel(z) = P^\parallel(z)\nabla_u P^\parallel(z)P^\parallel(z),$$

Hence  $P^\parallel(z)\nabla_u P^\parallel(z)P^\parallel(z) = 0$ . Similarly, we start from  $P^\perp(z)^2 = P^\perp(z)$ , taking the directional derivative on both side, left multiplying  $P^\perp(z)$  and right multiplying  $P^\perp(z)$ , and get

$$P^\perp(z)(\nabla_u P^\parallel(z))P^\parallel(z)P^\perp(z) + P^\perp(z)P^\parallel(z)(\nabla_u P^\parallel(z))P^\perp(z) = P^\perp(z)(\nabla_u P^\parallel(z))P^\perp(z).$$

Since  $P^\parallel(z)P^\perp(z) = P^\perp(z)P^\parallel(z)$ , we have  $P^\perp(z)(\nabla_u P^\parallel(z))P^\perp(z)$ . Therefore, we can express  $\nabla_u P^\parallel(z)$  on  $T_z(\mathcal{R}_t) \oplus N_z(\mathcal{R}_t)$  as

$$\nabla_u P^\parallel(z) = \begin{pmatrix} 0 & B^\top \\ B & 0 \end{pmatrix},$$

with  $B = P^\perp(z)(\nabla_u P^\parallel(z))P^\parallel(z) : T_z(\mathcal{R}_t) \rightarrow N_z(\mathcal{R}_t)$ . Therefore,

$$\|\nabla_u P^\perp(z)\| = \|\nabla_u P^\parallel(z)\| = \|B\| = \|\Pi_{t,z}(u, \cdot)\|_{T_z(\mathcal{R}_t) \rightarrow N_z(\mathcal{R}_t)} \lesssim \frac{1}{r_t}.$$

where the last inequality follows from Aamari et al. (2019, Theorem 3.4). Therefore, we have

$$W_t \lesssim V_t/r_t.$$

Hence we proved Proposition C.1-(3). □

**Lemma C.3** (Explicit formulas). *Under Assumption 1, we have that for all  $t \in [\delta, T]$ ,*

$$\begin{aligned} \nabla \log p_t(x) &= -\frac{x}{h_t} + \frac{m(t, x)}{h_t}, \quad \nabla^2 \log p_t(x) = -\frac{I_d}{h_t} + \frac{\Sigma(t, x)}{h_t^2}, \\ \nabla^3 \log p_t(x) &= \frac{\mathbb{E}[(U(t, x) - m(t, x))^{\otimes 3}]}{h_t^3}, \end{aligned}$$

where  $U(t, x) \in \mathbb{R}^d$  is a random vector taking values  $\{a_t x_0^{(i)}\}_{i=1}^n$  with probabilities  $\{\text{Softmax}(-\frac{\|x - a_t x_0\|^2}{2h_t})\}_i^n$  and

$$m(t, x) = \mathbb{E}[U(t, x)], \quad \Sigma(t, x) = \text{Cov}(U(t, x)),$$

with  $x_0 = (x_0^{(1)}, x_0^{(2)}, \dots, x_0^{(n)})$ . Furthermore,  $\nabla m(t, x) = \Sigma(t, x)/h_t$ .

**Lemma C.4** (Second Fundamental Form Bound). *For any  $t \in [\delta, T]$  and  $z \in \mathcal{R}_t$ , we have*

$$\|\Pi_{t,z}\| \leq \frac{1}{\beta_t} \|\nabla^3 \log p_t(z)\|.$$

*Proof of Lemma C.4.* For any  $z \in \mathcal{R}_t$ , we consider  $T \in \mathbb{R}^{d \times d^*}$  and  $N \in \mathbb{R}^{d \times (d-d^*)}$  to be the orthonormal basis spanning the spaces  $T_z(\mathcal{R}_t)$  and  $N_z(\mathcal{R}_t)$  respectively. We use coordinates  $(u, v) \in \mathbb{R}^{d^*} \times \mathbb{R}^{d-d^*}$  via  $x(u, v) = z + Tu + Nv$ . We can define the function

$$F(u, v) := N^\top \nabla \log p_t(x(u, v)) \in \mathbb{R}^{d-d^*}.$$

Since  $z \in \mathcal{R}_t$ , the definition of ridge set  $\mathcal{R}_t$  includes the normal component of the score  $\nabla \log p_t(x)$  is zero, i.e.,  $F(0, 0) = 0$ . The partial derivatives along the normal direction is

$$\partial_v F(u, v) = N^\top \nabla^2 \log p_t(x(u, v)) N, \quad \partial_v F(0, 0) = N^\top \nabla^2 \log p_t(z) N.$$

Since  $\nabla^2 \log p_t$  is invertible, we have

$$\|(\partial_v F(0, 0))^{-1}\| = \|(N^\top \nabla^2 \log p_t(z) N)^{-1}\| \leq \frac{1}{\beta_t},$$

where the inequality follows from the second condition in the definition of  $\mathcal{R}_t$ . Therefore, apply the implicit function theorem and we get: there exists a neighborhood  $0 \in U \subset \mathbb{R}^{d^*}$  and a  $C^2$  map  $\phi : U \rightarrow \mathbb{R}^{d-d^*}$  with  $\phi(0) = 0$  such that the local solution set to  $F(u, v) = 0$  is the set  $\{(u, v) \mid v = \phi(u)\}$ . Therefore, a local parametrization of the manifold is

$$\gamma(u) = z + Tu + N\phi(u).$$

And differentiating  $F(u, \phi(u)) = 0$  at  $u = 0$  implies  $\nabla \phi(0) = 0$ . Now differentiate  $F(u, \phi(u)) = 0$  twice and evaluate at  $u = 0$  and use the fact that  $\nabla \phi(0) = 0$ , we get

$$\partial_{uu} F(0, 0) + \partial_v F(0, 0) \nabla^2 \phi(0) = 0.$$

Since  $F(u, v) = N^\top \nabla \log p_t(x(u, v))$ , we have that for all  $\xi \in \mathbb{R}^{d^*}$ ,

$$\partial_{uu} F(0, 0)[\xi, \xi] = N^\top (\nabla^3 \log p_t(z))[T\xi, T\xi] \implies \|\partial_{uu} F(0, 0)\| \leq \|\nabla^3 \log p_t(z)\|.$$

Therefore, we have

$$\|\nabla^2 \phi(0)\| = \|-(\partial_v F(0, 0))^{-1} \partial_{uu} F(0, 0)\| \leq \|-(\partial_v F(0, 0))^{-1}\| \|\partial_{uu} F(0, 0)\| \leq \frac{1}{\beta_t} \|\nabla^3 \log p_t(z)\|.$$

Last, along the local parametrization  $\gamma(u) = z + Tu + N\phi(u)$ , we have

$$\partial_{ij}^2 \gamma(0) = N \partial_{ij}^2 \phi(0).$$

Therefore, apply the definition of  $\Pi$  and we get

$$\Pi_{t,z}(\nabla \gamma(0)\xi, \nabla \gamma(0)\theta) = P^\perp(z) \nabla^2 \gamma(0)[\xi, \theta] = N \nabla^2 \phi(0)[\xi, \theta].$$

Since  $N$  is isotropic (orthonormal), we prove the Lemma.  $\square$

**Lemma C.5** (Normal velocity field expression). *For all fixed  $t \in [\delta, T]$  and  $z \in \mathcal{R}_t$ , let  $E_t \in \mathbb{R}^{d \times (d-d^*)}$  be the normal eigen-matrix in the definition of  $\mathcal{R}_t$ . The normal velocity field in Lemma B.2 can be expressed as*

$$v_t(z) = -(E_t(z) \nabla^2 \log p_t(z) E_t(z))^{-1} E_t(z) \partial_t \nabla \log p_t(z) \in N_z(\mathcal{R}_t). \quad (19)$$

*Proof of Lemma C.5.* Fix  $t_0 \in (\delta, T)$  and  $z_0 \in \mathcal{R}_{t_0}$ , consider the normal gauge parametrization near  $(t_0, z_0)$ . we define  $F(t, x) := E_{t_0}(z_0)^\top \nabla \log p_t(x) \in \mathbb{R}^{d-d^*}$  with  $E_{t_0}$  being the orthonormal basis of  $N_{z_0}(\mathcal{R}_{t_0})$ . Since  $z_0 \in \mathcal{R}_{t_0}$ , we have  $F(t_0, z_0) = 0$ . Taking partial derivatives of  $F$  and evaluating at  $(t_0, z_0)$ , we get

$$\begin{aligned}\partial_t F(t_0, z_0) &= E_{t_0}(z_0)^\top \partial_t \nabla \log p_t(z_0)|_{t=t_0}, \\ \nabla F(t_0, z_0) &= E_{t_0}(z_0)^\top \nabla^2 \log p_{t_0}(z_0).\end{aligned}$$

Pick a normal gauge curve  $t \mapsto z(t) \in \mathcal{R}_t$  with  $z(t_0) = z_0$  and  $\partial_t z(t)|_{t=t_0} \in N_{z_0}(\mathcal{R}_{t_0})$ . We have  $F(z, z(t)) = 0$ . Taking derivative wrt.  $t$  to both sides of the equation, we get

$$\begin{aligned}0 &= \partial_t F(t_0, z_0) + \nabla F(t_0, z_0) \partial_t z \\ &= E_{t_0}(z_0)^\top \partial_t \nabla \log p_t(z_0)|_{t=t_0} + E_{t_0}(z_0)^\top \nabla^2 \log p_{t_0}(z_0) \partial_t z(t)|_{t=t_0} \\ &= E_{t_0}(z_0)^\top \partial_t \nabla \log p_t(z_0)|_{t=t_0} + E_{t_0}(z_0)^\top \nabla^2 \log p_{t_0}(z_0) E_{t_0}(z_0) \theta_0,\end{aligned}$$

In the last identity, due to the fact that  $\partial_t z(t)|_{t=t_0} \in N_{z_0}(\mathcal{R}_{t_0})$ , we write  $\partial_t z(t)|_{t=t_0} = E_{t_0}(z_0) \theta_0$  for some  $\theta_0 \in \mathbb{R}^{d-d^*}$ . According to the definition of  $\mathcal{R}_{t_0}$ , all eigenvalues of  $E_{t_0}(z_0)^\top \nabla^2 \log p_{t_0}(z_0) E_{t_0}(z_0) \in \mathbb{R}^{(d-d^*) \times (d-d^*)}$  are less than  $-\beta_{t_0}$ . Therefore,  $E_{t_0}(z_0)^\top \nabla^2 \log p_{t_0}(z_0) E_{t_0}(z_0)$  is invertible and

$$\|(E_{t_0}(z_0)^\top \nabla^2 \log p_{t_0}(z_0) E_{t_0}(z_0))^{-1}\| \leq 1/\beta_{t_0}.$$

Hence the normal velocity field  $v_{t_0}(z_0)$  is unique and

$$\begin{aligned}v_{t_0}(z_0) &= E_{t_0}(z_0) \theta_0 \\ &= E_{t_0}(z_0) (E_{t_0}(z_0)^\top \nabla^2 \log p_{t_0}(z_0) E_{t_0}(z_0))^{-1} E_{t_0}(z_0)^\top \partial_t \nabla \log p_t(z_0)|_{t=t_0} \\ &= (E_{t_0}(z_0)^\top \nabla^2 \log p_{t_0}(z_0) E_{t_0}(z_0))^{-1} E_{t_0}(z_0)^\top \partial_t \nabla \log p_t(z_0)|_{t=t_0}.\end{aligned}$$

Therefore, the Lemma is proved by varying  $t_0$  and  $z_0$ .  $\square$

**Lemma C.6** (Expression of ridge motion). *Let  $E_t \in \mathbb{R}^{d \times (d-d^*)}$  be the normal eigen-matrix in the definition of  $\mathcal{R}_t$ , i.e.,  $\mathcal{R}_t = \{x \in \mathbb{R}^d \mid E_t(x) \nabla \log p_t(x) = 0, \lambda_{d^*+1} \leq -\beta_t\}$ . Then we have*

$$E_t(z)^\top \partial_t \nabla \log p_t(z) = \frac{1}{h_t} E_t(z)^\top \partial_t m(t, z).$$

*Proof of Lemma C.6.* According to Tweedie's formula, we have

$$\begin{aligned}E_t(x) \nabla \log p_t(x) &= \frac{1}{h_t} E_t(x) (m(t, x) - x), \\ \implies E_t(x) \partial_t \nabla \log p_t(x) &= \frac{1}{h_t} E_t(x) \partial_t m(t, x) - \frac{\partial_t h_t}{h_t^2} E_t(x) (m(t, x) - x).\end{aligned}\tag{20}$$

For  $x = z \in \mathcal{R}_t$ , we have

$$E_t(x) \nabla \log p_t(x) = \frac{1}{h_t} E_t(x) (m(t, x) - x) = 0.$$

Therefore, the last term in (20) cancels. The Lemma is proved.  $\square$

**Lemma C.7.** *For any  $z \in \mathcal{R}_t$ , let  $E_t(z)$  be the eigen-matrix in Definition 3.1. We have*

$$\|E_t(z)^\top \partial_t m(t, z)\| \lesssim (1 + \dot{h}_t) a_t R.$$

*Proof of Lemma C.7.* By Lemma C.3,

$$\begin{aligned}
& \partial_t m(t, z) \\
&= \partial_t(h_t \nabla \log p_t(z) + h_t z) \\
&= \dot{h}_t \nabla \log p_t(z) + h_t \nabla \left( \frac{\partial_t p_t(z)}{p_t(z)} \right) + \dot{h}_t z \\
&= \dot{h}_t \nabla \log p_t(z) + h_t \nabla \left( \frac{z \cdot \nabla p_t(z) + \Delta p_t(z) + d p_t(z)}{p_t(z)} \right) + \dot{h}_t z \\
&= \dot{h}_t \nabla \log p_t(z) + h_t \nabla^2 \log p_t(z) z + d h_t \nabla \log p_t(z) + h_t \nabla \left( \frac{\Delta p_t(z)}{p_t(z)} \right) + \dot{h}_t z \\
&= (\dot{h}_t + d h_t) \nabla \log p_t(z) + h_t \nabla^2 \log p_t(z) z + \dot{h}_t z \\
&\quad + h_t (\text{cont}_{23} \nabla^3 \log p_t(z) + 2 \nabla^2 \log p_t(z) \nabla \log p_t(z)).
\end{aligned}$$

Since  $E_t(z)^\top \nabla \log p_t(z) = 0$  and  $E_t(z)^\top \nabla^2 \log p_t(z) \nabla \log p_t(z) = 0$  for all  $z \in \mathcal{R}_t$ , we have

$$E_t(z)^\top \partial_t m(t, z) = h_t E_t(z)^\top \nabla^2 \log p_t(z) z + \dot{h}_t E_t(z)^\top z + h_t E_t(z)^\top \text{cont}_{23} \nabla^3 \log p_t(z).$$

Next we bound the three terms on the RHS. First, according to Lemma C.3 and the fact that  $E_t(z)^\top \nabla \log p_t(z) = 0$ ,

$$\|E_t(z)^\top z\| = \|E_t(z)^\top m(t, z)\| \leq \|m(t, z)\| \leq a_t R.$$

Next, according to Lemma C.3,  $\nabla^2 \log p_t = -\frac{1}{h_t} I_d + \frac{\Sigma(t, z)}{h_t^2}$  with  $\Sigma(t, z) \succeq 0$ . Therefore, all negative eigenvalues of  $\nabla^2 \log p_t$  are at least  $-\frac{1}{h_t}$ . On the other hand,  $E_t(z)^\top$  only preserve eigenvalues that are smaller than  $-\beta_t$ . Therefore,  $\nabla^2 \log p_t(z)$  only contributes eigenvalues that are smaller than  $-\beta_t$ , hence negative, in  $E_t(z)^\top \nabla^2 \log p_t(z) z$ . We have

$$\|E_t(z)^\top \nabla^2 \log p_t(z) z\| \leq \frac{1}{h_t} \|E_t(z)^\top z\| \leq \frac{a_t R}{h_t}.$$

Regarding the last term, according to Lemma C.2,

$$\|E_t(z)^\top \text{cont}_{23} \nabla^3 \log p_t(z)\| = \|E_t(z)^\top (\nabla^3 \log p_t(z) : I)\| \leq \sqrt{d} \|\nabla^3 \log p_t(z)\| = \mathcal{O}\left(\frac{\sqrt{d} \theta_t R^3}{h_t^3}\right).$$

Since  $\theta_t$  can be arbitrarily chosen with order  $\exp(-o(h_t^{-1}))$ , the last term is negligible in the final order estimation. Hence we proved Lemma C.7.  $\square$

## D Analysis of Stage 1

In this section, we analyze the first stage: the reverse-time inference process enters the tube neighborhood of the log-density ridge with high probability. The formal version of Theorem 3.1 is derived from considering exactly the reverse OU process as the reference process:

$$dX_t^\leftarrow = \left( (1 - \frac{2}{h_{T-t}}) X_t^\leftarrow + \frac{2}{h_{T-t}} m(T-t, X_t^\leftarrow) \right) dt + \sqrt{2} dB_t^\leftarrow, \quad X_0^\leftarrow \sim p_T,$$

and  $X_t^\leftarrow \sim p_{T-t}$  for all  $0 \leq t \leq T_\delta$ . We define the entering time of  $X_t^\leftarrow$ :

$$t_{\text{in}}^\leftarrow := \inf\{0 \leq t \leq T - \delta | X_t^\leftarrow \in \mathcal{T}_{T-t}(\rho_{T-t})\}.$$

And we also analyze the reverse-time inference dynamics  $Y_t$  with

$$t_{\text{in}} := \inf\{0 \leq t \leq T - \delta \mid Y_t \in \mathcal{T}_{T-t}(\rho_{T-t})\}.$$

Then the formal Theorem that describing our stage 1 states as follows:

**Theorem D.1.** *Under Assumption 1, we have*

- (1)  $\mathbb{P}(t_{\text{in}}^{\leftarrow} \leq T - \delta) \geq 1 - e_{\delta}$ ;
- (2)  $\mathbb{P}(t_{\text{in}} \leq T - \delta) \geq 1 - e_{\delta} - \varepsilon(T)$ ;
- (3)  $\mathbb{P}(\tilde{t}_{\text{in}} \leq T - \delta) \geq 1 - e_{\delta} - \varepsilon(T) - \sqrt{\varepsilon_A(T, \delta)/8}$ ,

where  $e_{\delta} = h_{\delta}^{\zeta}$  for any  $\zeta > 0$  and  $e_{\delta} \rightarrow 0$  at any polynomial order as  $\delta \rightarrow 0^+$ .  $\varepsilon(T) = \frac{a_T}{2} \left( \frac{\sqrt{d}}{\sqrt{h_T}} + R \right) \rightarrow 0$  exponentially fast as  $T \rightarrow \infty$ .

*Proof of Theorem D.1.* First, for the exact reverse OU process, we have

$$\mathbb{P}(X_{T-\delta}^{\leftarrow} \in \mathcal{T}_{\delta}(\rho_{\delta})) = \mathbb{P}(X_{\delta} \in \mathcal{T}_{\delta}(\rho_{\delta})) = \mathbb{P}(\text{dist}(X_{\delta}, \mathcal{R}_{\delta}) \leq \rho_{\delta}) \geq \mathbb{P}(\text{dist}(a_{\delta}X_0, \mathcal{R}_{\delta}) + \sqrt{h_{\delta}}\|z\| \leq \rho_{\delta}).$$

We will first show  $\text{dist}(a_{\delta}X_0, \mathcal{R}_{\delta})$  is very small when  $\delta \ll 1$ , and then apply the concentration of  $d$ -dimensional Gaussian to bound the probability.

According to Lemma D.1, if  $\delta$  is small enough such that  $h_{\delta}^{-1} > \frac{2}{a_{\delta}^2 \Delta^2} \ln\left(\frac{4a_{\delta}^2 R^2 (n-1)}{\rho_{\delta}}\right)$ , then

$$\text{dist}(a_{\delta}X_0, \mathcal{R}_{\delta}) \leq \|z_i - a_{\delta}x_0^{(i)}\| \leq \rho_{\delta}/2.$$

Then we have

$$\mathbb{P}(X_{T-\delta}^{\leftarrow} \in \mathcal{T}_{\delta}(\rho_{\delta})) \geq \mathbb{P}(\sqrt{h_{\delta}}\|z\| \leq \rho_{\delta}) = \mathbb{P}(\|z\|^2 \leq \rho_{\delta}^2/h_{\delta})$$

According to the order estimation of  $r_t$  in Proposition C.1, we can pick  $\delta$  small such that  $\rho_{\delta}^2/h_{\delta} \leq d + 2\sqrt{d\zeta \log(1/h_{\delta})} + 2\zeta \log(1/h_{\delta})$  for any  $\zeta > 0$ . Then according to the LMI inequality (Moshksar, 2024), we have

$$\mathbb{P}(X_{T-\delta}^{\leftarrow} \in \mathcal{T}_{\delta}(\rho_{\delta})) \geq \mathbb{P}(\|z\|^2 \leq d + 2\sqrt{d\zeta \log(1/h_{\delta})} + 2\zeta \log(1/h_{\delta})) \geq 1 - h_{\delta}^{\zeta}.$$

Next, for the reverse-time inference process  $Y_t$ . Notice that  $Y_t$  and  $X_t^{\leftarrow}$  have the same generator but with different initializations:  $Y_0 \sim \mathcal{N}(0, I_d)$  while  $X_0^{\leftarrow} \sim p_T$ . Therefore, we have

$$\begin{aligned} |\mathbb{P}(Y_{T-\delta} \in \mathcal{T}_{\delta}(\rho_{\delta})) - \mathbb{P}(X_{T-\delta}^{\leftarrow} \in \mathcal{T}_{\delta}(\rho_{\delta}))| &\leq \text{TV}(\text{Law}(Y_{T-\delta}), p_{\delta}) \leq \text{TV}(\mathcal{N}(0, I_d), p_T) \\ &\leq \sqrt{\frac{\text{KL}(p_T \mid \mathcal{N}(0, I_d))}{2}} \leq \frac{a_T}{2} \left( \frac{\sqrt{d}}{\sqrt{h_T}} + R \right), \end{aligned}$$

where the second inequality follows from data processing inequality. The third inequality follows from Pinsker's inequality. The last inequality follows from property of OU process, see He et al. (2024, Proposition C.1). Therefore, we proved

$$\mathbb{P}(Y_{T-\delta} \in \mathcal{T}_{\delta}(\rho_{\delta})) \geq \mathbb{P}(X_{T-\delta}^{\leftarrow} \in \mathcal{T}_{\delta}(\rho_{\delta})) - \frac{a_T}{2} \left( \frac{\sqrt{d}}{\sqrt{h_T}} + R \right) \geq 1 - h_{\delta}^{\zeta} - \frac{a_T}{2} \left( \frac{\sqrt{d}}{\sqrt{h_T}} + R \right).$$

Last, for the inference process  $\tilde{Y}_t$ , except for initialization error, there are extra trajectory error from  $X_t^\leftarrow$  due to the approximate posterior mean  $m_A$ . We have

$$|\mathbb{P}(\tilde{Y}_{T-\delta} \in \mathcal{T}_\delta(\rho_\delta)) - \mathbb{P}(X_{T-\delta}^\leftarrow \in \mathcal{T}_\delta(\rho_\delta))| \leq \text{TV}(\text{Law}(\tilde{Y}_{T-\delta}), p_\delta) \leq \sqrt{\frac{\text{KL}(\mathbb{P}^\leftarrow \|\tilde{\mathbb{P}})}{2}},$$

where  $\mathbb{P}^\leftarrow$  is the path measure of  $X_t^\leftarrow$  and  $\tilde{\mathbb{P}}$  is the path measure of  $\tilde{Y}_t$ . Then we can apply the traditional analysis of the inference process via Girsanov's Theorem. We get

$$\begin{aligned} & |\mathbb{P}(\tilde{Y}_{T-\delta} \in \mathcal{T}_\delta(\rho_\delta)) - \mathbb{P}(X_{T-\delta}^\leftarrow \in \mathcal{T}_\delta(\rho_\delta))| \\ & \leq \sqrt{\frac{\text{KL}(p_T \|\mathcal{N}(0, I_d))}{2} + \frac{1}{8} \int_\delta^T h_t^{-2} \mathbb{E}[\|m(t, X_t) - m_A(t, X_t)\|^2] dt} \\ & \leq \frac{a_T}{2} \left( \frac{\sqrt{d}}{\sqrt{h_T}} + R \right) + \sqrt{\frac{1}{8} \int_\delta^T h_t^{-2} \mathbb{E}[\|m(t, X_t) - m_A(t, X_t)\|^2] dt}. \end{aligned}$$

The statements follows from transferring the probability to the defined stopping times.  $\square$

**Lemma D.1.** *Under Assumption 1, when  $\delta \ll 1$ , for each  $i \in [n]$ , there exists a point  $z_i \in \mathcal{R}_\delta$  such that*

$$\|z_i - a_\delta x_0^{(i)}\| \leq 2a_\delta R(n-1) \exp\left(-\frac{a_\delta^2 \Delta^2}{2h_\delta}\right).$$

*Proof of Lemma D.1.* According to Lemma C.3, we know

$$\begin{aligned} \nabla \log p_\delta(x) &= -\frac{x}{h_\delta} + \frac{1}{h_\delta} \sum_{i=1}^n \text{Softmax}\left(-\frac{\|x - a_\delta x_0\|^2}{2h_\delta}\right)_i a_\delta x_0^{(i)} \\ \nabla^2 \log p_\delta(x) &= -\frac{1}{h_\delta} I_d + \frac{1}{h_\delta^2} \sum_{i=1}^n \text{Softmax}\left(-\frac{\|x - a_\delta x_0\|^2}{2h_\delta}\right)_i (a_\delta x_0^{(i)} - m(\delta, x))(a_\delta x_0^{(i)} - m(\delta, x))^\top. \end{aligned}$$

Next, we find critical points of  $\nabla \log p_\delta(x)$  and show that they are on the log-density ridge  $\mathcal{R}_\delta$ .

According to the expression of  $\nabla \log p_\delta(x)$ , the critical points are fixed points of

$$x = \sum_{i=1}^n \text{Softmax}\left(-\frac{\|x - a_\delta x_0\|^2}{2h_\delta}\right)_i a_\delta x_0^{(i)} = m(\delta, x).$$

We claim: for each  $i \in [n]$ , within  $B(a_\delta x_0^{(i)}, a_\delta \Delta/4)$ , there exists a unique fixed point, denoted as  $z_i$ . We prove the claim by the contraction mapping theorem. First,  $B(a_\delta x_0^{(i)}, a_\delta \Delta/4) \subset \mathbb{R}^d$  is a closed ball. Second, for all  $x \in B(a_\delta x_0^{(i)}, a_\delta \Delta/4)$ , for all  $j \neq i$ , we have

$$\begin{aligned} \frac{\text{Softmax}\left(-\frac{\|x - a_\delta x_0\|}{2h_\delta}\right)_j}{\text{Softmax}\left(-\frac{\|x - a_\delta x_0\|}{2h_\delta}\right)_i} &= \exp\left(-\frac{\|x - a_\delta x_0^{(j)}\|}{2h_\delta} + \frac{\|x - a_\delta x_0^{(i)}\|}{2h_\delta}\right) \leq \exp\left(-\frac{a_\delta^2 \Delta^2}{2h_\delta}\right), \\ \Rightarrow \sum_{j \neq i} \text{Softmax}\left(-\frac{\|x - a_\delta x_0\|}{2h_\delta}\right)_j &\leq (n-1) \exp\left(-\frac{a_\delta^2 \Delta^2}{2h_\delta}\right). \end{aligned}$$

Hence, we can show  $m(\delta, \cdot) : B(a_\delta x_0^{(i)}, a_\delta \Delta/4) \rightarrow B(a_\delta x_0^{(i)}, a_\delta \Delta/4)$ , i.e., for all  $x \in B(a_\delta x_0^{(i)}, a_\delta \Delta/4)$ ,

$$\|m(\delta, x) - a_\delta x_0^{(i)}\| \leq \sum_{j \neq i} \text{Softmax}\left(-\frac{\|x - a_\delta x_0\|}{2h_\delta}\right)_j a_\delta \|x_0^{(j)} - x_0^{(i)}\|$$

$$\leq 2a_\delta R(n-1) \exp\left(-\frac{a_\delta^2 \Delta^2}{2h_\delta}\right) < a_\delta \Delta/4,$$

given the early stopping time is small enough such that  $h_\delta^{-1} > \frac{2}{a_\delta^2 \Delta^2} \ln(\frac{8R(n-1)}{\Delta})$ . Meanwhile, for  $x \in B(a_\delta x_0^{(i)}, a_\delta \Delta/4)$ , similar to the proof of Lemma C.2,

$$\begin{aligned} \|\nabla m(\delta, x)\| &\leq \frac{1}{h_\delta} \sum_{j \neq i} \text{Softmax}\left(-\frac{\|x - a_\delta x_0\|}{2h_\delta}\right)_j a_\delta^2 \|x_0^{(j)} - x_0^{(i)}\|^2 \\ &\leq \frac{a_\delta^2 R^2(n-1)}{h_\delta} \exp\left(-\frac{a_\delta^2 \Delta^2}{2h_\delta}\right) < 1, \end{aligned}$$

given the early stopping time is small enough such that  $h_\delta^{-1} > \frac{2}{a_\delta^2 \Delta^2} \ln(\frac{a_\delta^2 R^2(n-1)}{h_\delta})$ . Therefore, according to the contraction mapping theorem, there exists a unique fixed point  $z_i \in B(a_\delta x_0^{(i)}, a_\delta \Delta/4)$ . At each  $z_i$ , according to Lemma C.3, we have

$$\begin{aligned} \nabla^2 \log p_\delta(z_i) &= -\frac{1}{h_\delta} I_d + \frac{\text{Cov}(U(\delta, x))}{h_\delta^2} \\ &\preceq -\frac{1}{h_\delta} I_d + \frac{1}{h_\delta^2} a_\delta^2 R^2(n-1) \exp\left(-\frac{a_\delta^2 \Delta^2}{2h_\delta}\right) I_d \\ &\preceq -\frac{1}{2h_\delta} I_d, \end{aligned}$$

given the early stopping time is small enough such that  $h_\delta^{-1} > \frac{2}{a_\delta^2 \Delta^2} \ln(\frac{a_\delta^2 R^2(n-1)}{2h_\delta})$ . Therefore, we proved that  $z_i \in \mathcal{R}_\delta$  with  $\beta_\delta = \Theta(\frac{1}{h_\delta})$ . Last, we estimate the distance from  $z_i$  to  $a_\delta x_0^{(i)}$ .

$$\begin{aligned} \|z_i - a_\delta x_0^{(i)}\| &= \|m(t, z_i) - x_0^{(i)}\| \leq \sum_{j \neq i} \text{Softmax}\left(-\frac{\|z_i - a_\delta x_0\|}{2h_\delta}\right)_j a_\delta \|x_0^{(j)} - x_0^{(i)}\| \\ &\leq 2a_\delta R(n-1) \exp\left(-\frac{a_\delta^2 \Delta^2}{2h_\delta}\right). \end{aligned}$$

□

## E Analysis of Stage 2

In this section, we analyze the stage 2 - align along normal directions. We start from a property of the square-normal distance, which simply follows from the log-density ridge property proved in Appendix C.

**Corollary E.1.** *As a consequence of Proposition B.1, the following properties hold for the square-distance function  $D_t(x) := \|x - \Pi_t(x)\|^2$ :*

- (1)  $D_t \in C^2(\mathcal{T}_t(\rho_t))$  and  $\nabla D_t(x) = 2n_t(x)$ ;
- (2)  $\sup_x \|\nabla^2 D_t(x)\| \leq \frac{2}{1-\rho_t/r_t}$ . As a consequence,  $\sup_x \Delta D_t(x) \leq \frac{2d}{1-\rho_t/r_t}$ .

We will prove Theorem 3.2 for both  $Y_t$  and  $\tilde{Y}_t$ , given below

$$dY_t = \underbrace{\left( Y_t - \frac{2}{h_{T-t}} Y_t + \frac{2}{h_{T-t}} m(T-t, Y_t) dt + \sqrt{2} d\bar{B}_t \right)}_{:= b(T-t, Y_t)} \quad Y_0 \sim \mathcal{N}(0, I_d),$$

$$d\tilde{Y}_t = \underbrace{\left( \tilde{Y}_t - \frac{2}{h_{T-t}} \tilde{Y}_t + \frac{2}{h_{T-t}} m_A(T-t, \tilde{Y}_t) \right) dt + \sqrt{2} d\tilde{B}_t}_{:=b_A(T-t, \tilde{Y}_t)}, \quad \tilde{Y}_0 \sim \mathcal{N}(0, I_d).$$

Note that for  $Y_t$ , it is differed from exact reverse-time OU only in initialization. Therefore, we would like to highlight the relation between reverse OU-dynamics and the log-density ridge geometry through analysis of  $Y_t$ . The gap between  $Y_t$  and  $\tilde{Y}_t$  lies in the approximation error of the posterior mean. Therefore, our analysis for  $\tilde{Y}_t$  will highlight the effect of posterior mean approximation error.

*Proof of Theorem 3.2.* For any  $t \in [0, T - \delta]$ ,  $x \in \mathcal{T}_{T-t}(\rho_t)$ , recall that  $D_{T-t}(x) = \|n_{T-t}(x)\|^2$  and  $n_{T-t}(x) = x - \Pi_{T-t}(x)$ . Once the processes enter  $\mathcal{T}_{T-t}(\rho_t)$ , we can track the evolution of  $D_{T-t}$  via Itô's formula. For the reverse process  $Y_t$ , we have

$$\begin{aligned} dD_{T-t}(Y_t) &= (\partial_t D_{T-t}(Y_t) + 2\langle n_{T-t}(Y_t), b(T-t, Y_t) \rangle + 2\text{trace}(\nabla^2 D_{T-t}(Y_t))) dt \\ &\quad + 2\sqrt{2}\langle n_{T-t}(Y_t), d\bar{B}_t \rangle, \end{aligned}$$

where we have the following estimations for the drift terms:

- (1) According to Corollary E.1,  $2\text{trace}(\nabla^2 D_{T-t}(Y_t)) \leq \frac{4d}{1-\rho_{T-t}/r_{T-t}}$ . Picking  $\rho_t = r_t/2$  for all  $t$  and we get  $2\text{trace}(\nabla^2 D_{T-t}(Y_t)) \leq 8d$ .
- (2) According to Remark C.1,

$$\begin{aligned} \partial_t D_{T-t}(Y_t) &= -\partial_s D_s(Y_t)|_{s=T-t} = 2\langle n_{T-t}(Y_t), \partial_s \Pi_s(Y_t)|_{s=T-t} \rangle \\ &\leq 2\rho_{T-t} \sup_{x \in \mathcal{T}_{T-t}(\rho_{T-t})} \|\partial_s \Pi_s(x)|_{s=T-t}\| := 2\rho_{T-t} S_{T-t}, \end{aligned}$$

and  $S_{T-t} = \mathcal{O}(R)$  when  $T - t \rightarrow 0^+$ .

- (3) if we denote  $z = z_{T-t} := \Pi_{T-t}(Y_t)$ ,  $n_{T-t}(Y_t) \perp T_z(\mathcal{R}_{T-t})$  and we have

$$\begin{aligned} 2\langle n_{T-t}(Y_t), b(T-t, Y_t) \rangle &= 2\langle n_{T-t}(Y_t), Y_t \rangle + 4\langle n_{T-t}(Y_t), \nabla \log p_{T-t}(Y_t) \rangle \\ &= 2\|n_{T-t}(Y_t)\|^2 + 4\langle n_{T-t}(Y_t), \nabla \log p_{T-t}(Y_t) \rangle, \end{aligned}$$

In the last term, we can write  $Y_t = z + n_{T-t}(Y_t)$  and expand  $\nabla \log p_{T-t}(Y_t)$  at  $z \in \mathcal{R}_{T-t}$ . Then we have

$$\begin{aligned} &\langle n_{T-t}(Y_t), \nabla \log p_{T-t}(Y_t) \rangle \\ &= \langle n_{T-t}(Y_t), \nabla \log p_{T-t}(z) \rangle + \langle n_{T-t}(Y_t), \nabla^2 \log p_{T-t}(z) n_{T-t}(Y_t) \rangle \\ &\quad + \frac{1}{2} \langle n_{T-t}(Y_t), \nabla^3 \log p_{T-t}(z') n_{T-t}(Y_t)^{\otimes 2} \rangle, \end{aligned}$$

where

$$\begin{aligned} &\langle n_{T-t}(Y_t), \nabla \log p_{T-t}(z) \rangle = 0, && \text{definition of } \mathcal{R}_{T-t}, \\ &\langle n_{T-t}(Y_t), \nabla^2 \log p_{T-t}(z) n_{T-t}(Y_t) \rangle \\ &= \langle n_{T-t}(Y_t), P^\perp(z) \nabla^2 \log p_{T-t}(z) n_{T-t}(Y_t) \rangle \leq -\beta_{T-t} \|n_{T-t}(Y_t)\|^2, && \text{definition of } \mathcal{R}_{T-t}, \\ &\langle n_{T-t}(Y_t), \nabla^3 \log p_{T-t}(z') n_{T-t}(Y_t)^{\otimes 2} \rangle \\ &\leq \sup_x \|\nabla \log p_{T-t}(x)\| \|n_{T-t}(Y_t)\|^3 \leq \frac{80a_{T-t}^3 R^3}{h_{T-t}^3} \rho_{T-t} \|n_{T-t}(Y_t)\|^2 && \text{Lemma C.2} \end{aligned}$$

$$\leq \frac{a_{T-t}^3 \beta_{T-t}}{2} D_{T-t}(Y_t) \quad \text{Proposition C.1}$$

The last identity follows from Proposition C.1 by picking  $\theta_t$  such that  $r_t = \beta_t h_t^3 R^{-3}/80$  and  $\rho_t = r_t/2$ . Combining the above inequalities, we have

$$\langle n_{T-t}(Y_t), \nabla \log p_{T-t}(Y_t) \rangle \leq -\beta_{T-t}(1 - a_{T-t}^3/4) \|n_{T-t}(Y_t)\|^2 \leq -\frac{3}{4} \beta_{T-t} D_{T-t}(Y_t).$$

Therefore, we have

$$2\langle n_{T-t}(Y_t), b(T-t, Y_t) \rangle \leq -(3\beta_{T-t} - 2) D_{T-t}(Y_t).$$

Combining all the estimations and taking expectations of  $D_{T-t}$ , we obtain the following inequality

$$\frac{d}{dt} \mathbb{E}[D_{T-t}(Y_t)] \leq -(3\beta_{T-t} - 2) \mathbb{E}[D_{T-t}(Y_t)] + 2\rho_{T-t} S_{T-t} + 8d.$$

Last, apply Gronwall's inequality, for any  $t_{\text{in}} \in (0, T - \delta)$  and  $t \in (t_{\text{in}}, T - \delta]$ , we obtain

$$\begin{aligned} \mathbb{E}[D_{T-t}(Y_t)] &\leq \exp\left(-\int_{t_{\text{in}}}^t 3\beta_{T-u} - 2du\right) \mathbb{E}[D_{t-t_{\text{in}}}(Y_{t_{\text{in}}})] \\ &\quad + \int_{t_{\text{in}}}^t \exp\left(-\int_u^t 3\beta_{T-s} - 2ds\right) (2\rho_{T-u} S_{T-u} + 8d) du. \end{aligned}$$

When  $t = T - \delta$ ,  $\beta_t = c/h_t$  and  $\delta \ll 1$ , we have

$$\int_{t_{\text{in}}}^{T-\delta} \exp\left(-\int_u^{T-\delta} 3\beta_{T-s} - 2ds\right) (2\rho_{T-u} S_{T-u} + 8d) du = \mathcal{O}(d\delta^{\frac{3c}{2}}).$$

For the reverse-time inference process  $\tilde{Y}_t$ , we have

$$\begin{aligned} dD_{T-t}(\tilde{Y}_t) &= (\partial_t D_{T-t}(\tilde{Y}_t) + 2\langle n_{T-t}(\tilde{Y}_t), b_A(T-t, \tilde{Y}_t) \rangle \\ &\quad + 2\text{trace}(\nabla^2 D_{T-t}(\tilde{Y}_t))) dt + 2\sqrt{2}\langle n_{T-t}(\tilde{Y}_t), d\tilde{B}_t \rangle. \end{aligned}$$

Notice that the only difference to that of  $Y_t$  is the error  $e_A(t, \cdot) = m(t, \cdot) - m_A(t, \cdot)$  within the normal space, i.e.,  $e_A^\perp(t, x) := P^\perp(\Pi_t(x))e_A(t, x)$ . Similarly, we have the inequality

$$\begin{aligned} \frac{d}{dt} \mathbb{E}[D_{T-t}(\tilde{Y}_t)] &\leq -(3\beta_{T-t} - 2) \mathbb{E}[D_{T-t}(\tilde{Y}_t)] + 2\rho_{T-t} S_{T-t} + 8d + 2\mathbb{E}[\langle n_{T-t}(\tilde{Y}_t), \frac{1}{h_{T-t}} e_A(T-t, \tilde{Y}_t) \rangle] \\ &\leq -2(\beta_{T-t} - 1) \mathbb{E}[D_{T-t}(\tilde{Y}_t)] + 2\rho_{T-t} S_{T-t} + 8d + \frac{\mathbb{E}[\|e_A^\perp(T-t, \tilde{Y}_t)\|^2]}{h_{T-t}^2 \beta_{T-t}}, \end{aligned}$$

where the last inequality follows from Young's inequality. Therefore, according to the Gronwall's inequality,

$$\begin{aligned} \mathbb{E}[D_{T-t}(\tilde{Y}_t)] &\leq \exp\left(-2 \int_{\tilde{t}_{\text{in}}}^t \beta_{T-u} - 1 du\right) \mathbb{E}[D_{t-\tilde{t}_{\text{in}}}(\tilde{Y}_{\tilde{t}_{\text{in}}})] \\ &\quad + \int_{\tilde{t}_{\text{in}}}^t \exp\left(-2 \int_u^t \beta_{T-s} - 1 ds\right) (2\rho_{T-u} S_{T-u} + \frac{\mathbb{E}[\|e_A^\perp(T-u, \tilde{Y}_u)\|^2]}{h_{T-u}^2 \beta_{T-u}} + 8d) du. \end{aligned}$$

When  $t = T - \delta$ ,  $\beta_t = c/h_t$  and  $\delta \ll 1$ , we have

$$\begin{aligned} & \int_{\tilde{t}_{\text{in}}}^{T-\delta} \exp \left( -2 \int_u^{T-\delta} \beta_{T-s} - 1 \, ds \right) du = \mathcal{O}(\delta^c), \\ & \int_{\tilde{t}_{\text{in}}}^{T-\delta} \exp \left( -2 \int_u^{T-\delta} \beta_{T-s} - 1 \, ds \right) h_{T-u}^{-2} \beta_{T-u}^{-1} \mathbb{E}[\|e_A^\perp(T-u, \tilde{Y}_u)\|^2] du \\ &= \mathcal{O}(\delta^c) \int_{\tilde{t}_{\text{in}}}^{T-\delta} h_{T-u}^{-1-c} \mathbb{E}[\|e_A^\perp(T-u, \tilde{Y}_u)\|^2] du. \end{aligned}$$

□

## F Analysis of Stage 3

In this section, we analyze the stage 3 for both  $Y_t$  and  $\tilde{Y}_t$ , sliding along the tangent directions of the log-ridge density sets. We first state a formal version of Theorem 3.3, then provide the proof of it. Recall

$$\begin{aligned} dY_t &= \underbrace{\left( Y_t - \frac{2}{h_{T-t}} Y_t + \frac{2}{h_{T-t}} m(T-t, Y_t) dt + \sqrt{2} d\bar{B}_t, \quad Y_0 \sim \mathcal{N}(0, I_d), \right)}_{:=b(T-t, Y_t)} \\ d\tilde{Y}_t &= \underbrace{\left( \tilde{Y}_t - \frac{2}{h_{T-t}} \tilde{Y}_t + \frac{2}{h_{T-t}} m_A(T-t, \tilde{Y}_t) dt + \sqrt{2} d\tilde{B}_t, \quad \tilde{Y}_0 \sim \mathcal{N}(0, I_d). \right)}_{:=b_A(T-t, \tilde{Y}_t)} \end{aligned}$$

In Section 3.4, we introduced the tangent frame at the center  $m_{T-t}^{(i)}$ , denoted as  $U_{T-t}^{(i)} \in \mathbb{R}^{d \times d^*}$ .  $U_{T-t}^{(i)}$  is a matrix consisting of orthonormal columns as the top- $d^*$  eigenvectors of  $\nabla \log p_{T-t}(m_{T-t}^{(i)})$ .

For  $Y_t \in \mathcal{T}_{T-t}(\rho_{T-t}) \cap \mathcal{B}_{T-t}^{(i)}(\eta_{T-t})$ , we define the residual  $r_t^{(i)} = Y_t - m_{T-t}^{(i)}$  and

$$u_t^{(i)} := (U_{T-t}^{(i)})^\top (Y_t - m_{T-t}^{(i)}) \in \mathbb{R}^{d^*}.$$

Therefore,  $(U_{T-t}^{(i)})^\top U_{T-t}^{(i)} = I_{d^*}$  and  $U_{T-t}^{(i)}(U_{T-t}^{(i)})^\top = P(m_{T-t}^{(i)})$  is approximately the projection on the tangent space at point  $\Pi_t(m_{T-t}^{(i)})$ : the ideal tangential component to look at requires the tangent frame at  $\Pi_t(m_{T-t}^{(i)})$ . According to D.1,  $m_{T-t}^{(i)}$  is exponentially close to  $\Pi_t(m_{T-t}^{(i)})$  as  $T-t \rightarrow \delta^+ \ll 1$ . Therefore, we adopt  $u_t^{(i)}$  to approximately track the tangent component of the residual  $r_t^{(i)}$ . Similarly,  $\tilde{u}_t^{(i)}$  provides a reasonable tangential estimation of the residual for  $\tilde{Y}_t$ .

Now we introduce the proof of Theorem 3.3.

*Proof of Theorem 3.3.* Apply Itô's formula to  $u_t^{(i)}$  and we get

$$\begin{aligned} du_t^{(i)} &= \partial_t (U_{T-t}^{(i)})^\top (Y_t - m_{T-t}^{(i)}) dt + (U_{T-t}^{(i)})^\top (b(T-t, Y_t) dt - \partial_t a_{T-t} x_0^{(i)} dt + \sqrt{2} d\bar{B}_t) \\ &= -\left(\frac{2}{h_{T-t}} - 1\right) u_t^{(i)} dt + \partial_t (U_{T-t}^{(i)})^\top (Y_t - m_{T-t}^{(i)}) dt + \sqrt{2} (U_{T-t}^{(i)})^\top d\bar{B}_t \\ &\quad + (U_{T-t}^{(i)})^\top (b(T-t, Y_t) - (Y_t + \frac{2}{h_{T-t}} (m_{T-t}^{(i)} - Y_t))) dt. \end{aligned}$$

Now apply Itô's formula again to  $\|u_t^{(i)}\|^2$  and we get,

$$d\|u_t^{(i)}\|^2 = 2\langle u_t^{(i)}, du_t^{(i)} \rangle + 2\text{trace}((U_{T-t}^{(i)})^\top U_{T-t}^{(i)}) dt$$

$$\begin{aligned}
&= -2\left(\frac{2}{h_{T-t}} - 1\right)\|u_t^{(i)}\|^2 dt + 2\langle u_t^{(i)}, \partial_t(U_{T-t}^{(i)})^\top(Y_t - m_{T-t}^{(i)}) \rangle dt \\
&\quad + 2\langle u_t^{(i)}, (U_{T-t}^{(i)})^\top(b(T-t, Y_t) - (Y_t + \frac{2}{h_{T-t}}(m_{T-t}^{(i)} - Y_t))) \rangle dt \\
&\quad + 2d^* dt + 2\sqrt{2}\langle u_t^{(i)}, (U_{T-t}^{(i)})^\top d\bar{B}_t \rangle,
\end{aligned}$$

where according to Lemma F.2,

$$\begin{aligned}
&\langle u_t^{(i)}, \partial_t(U_{T-t}^{(i)})^\top(Y_t - m_{T-t}^{(i)}) \rangle \\
&= \langle u_t^{(i)}, \partial_t(U_{T-t}^{(i)})^\top U_{T-t}^{(i)} u_t^{(i)} \rangle + \langle u_t^{(i)}, \partial_t(U_{T-t}^{(i)})^\top(I_d - U_{T-t}^{(i)}(U_{T-t}^{(i)})^\top)(Y_t - m_{T-t}^{(i)}) \rangle \\
&\leq 0 + \frac{1}{h_{T-t}}\|u_t^{(i)}\|^2 + h_{T-t}\|P(m_{T-t}^{(i)})\partial_t P(m_{T-t}^{(i)})(I_d - P(m_{T-t}^{(i)}))\|^2\|r_t^{(i)}\|^2,
\end{aligned}$$

and according to Lemma F.1 and Assumption 1,

$$\begin{aligned}
&\langle u_t^{(i)}, (U_{T-t}^{(i)})^\top(b(T-t, Y_t) - (Y_t + \frac{2}{h_{T-t}}(m_{T-t}^{(i)} - Y_t))) \rangle \\
&\leq \|b(T-t, Y_t) - (Y_t + \frac{2}{h_{T-t}}(m_{T-t}^{(i)} - Y_t))\|\|Y_t - a_{T-t}x_0^{(i)}\| \\
&\leq 8R^2a_{T-t}^2h_{T-t}^{-1}\theta_{T-t},
\end{aligned}$$

Therefore, taking expectations on both sides of the SDE for  $\|u_t^{(i)}\|^2$ , we have

$$\begin{aligned}
\frac{d}{dt}\mathbb{E}[\|u_t^{(i)}\|^2] &\leq -2\left(\frac{1}{h_{T-t}} - 1\right)\mathbb{E}[\|u_t^{(i)}\|^2] + 2h_{T-t}\|P(m_{T-t}^{(i)})\partial_t P(m_{T-t}^{(i)})(I_d - P(m_{T-t}^{(i)}))\|^2\|r_t^{(i)}\|^2 \\
&\quad + 8R^2a_{T-t}^2h_{T-t}^2\eta_{T-t} + 2d^*,
\end{aligned}$$

where as  $T-t \rightarrow \delta^+ \ll 1$ ,

(1)  $-2(\frac{1}{h_{T-t}} - 1)\mathbb{E}[\|u_t^{(i)}\|^2]$  is a strict contraction term with infinite force;

(2)  $2h_{T-t}\|P(m_{T-t}^{(i)})\partial_t P(m_{T-t}^{(i)})(I_d - P(m_{T-t}^{(i)}))\|^2\|r_t^{(i)}\|^2 = O(1)$ :

(i) Under Assumption 1,  $\|r_t^{(i)}\|^2 = \mathcal{O}(R^2)$ ;

(ii) According to the definition of  $P(m_{T-t}^{(i)})$  and estimations Lemma C.2,

$$\|P(m_{T-t}^{(i)})\partial_t P(m_{T-t}^{(i)})(I_d - P(m_{T-t}^{(i)}))\| = \mathcal{O}(\theta_{T-t}\text{poly}(R, h_t^{-1}))$$

for any  $\theta_{T-t} = \exp(-o(\frac{1}{h_{T-t}}))$ ;

Combining the two estimations, we have the whole term is  $\mathcal{O}(1)$ .

(3)  $8R^2a_{T-t}^2h_{T-t}^2\theta_{T-t} = \mathcal{O}(1)$  since we can choose  $\theta_{T-t} = \exp(-o(\frac{1}{h_{T-t}}))$  as discussed in Remark C.2.

Therefore, we obtain that  $\frac{d}{dt}\mathbb{E}[\|u_t^{(i)}\|^2] \leq -2(\frac{1}{h_{T-t}} - 1)\mathbb{E}[\|u_t^{(i)}\|^2] + \epsilon_{T-t}^{(i)}$  with  $\epsilon_{T-t}^{(i)} = \mathcal{O}(d)$  as  $t \rightarrow T^-$ . By Gronwall's inequality,

$$\mathbb{E}[\|u_t^{(i)}\|^2] \leq \exp\left(-2\int_{t_{in}}^t \frac{1}{h_{T-u}} - 1 du\right)\mathbb{E}[\|u_{t_{in}}^{(i)}\|^2] + \int_{t_{in}}^t \exp\left(-2\int_u^t \frac{1}{h_{T-s}} - 1 ds\right)\epsilon_{T-u}^{(i)} du.$$

When  $t = T - \delta$  and  $\delta \ll 1$ , we have

$$\int_{t_{\text{in}}}^{T-\delta} \exp\left(-2 \int_u^{T-\delta} \frac{1}{h_{T-s}} - 1 \right) \epsilon_{T-u}^{(i)} du = \mathcal{O}(d\delta \log(1/\delta)).$$

Hence we prove that as  $t \rightarrow T - \delta$ , with high probability (tends to 1 as  $\delta \rightarrow 0^+$ ),  $Y_t$  will enter some region dominated by one of the center  $\mathcal{B}_{T-t}^{(i)}(\theta_{T-t})$  and then be pulled towards the center  $a_{T-t}x_0^{(i)}$ . Furthermore, quantitatively, the expected square-norm of  $Y_{t-\delta} - a_\delta x_0^{(i)}$  is of order  $\mathcal{O}(\delta)$ .

For the reverse-time inference process  $\tilde{Y}_t$ , we utilize the same idea. Define

$$\tilde{r}_t^{(i)} = \tilde{Y}_t - m_{T-t}^{(i)}, \quad \tilde{u}_t^{(i)} := (U_{T-t}^{(i)})^\top (\tilde{Y}_t - m_{T-t}^{(i)}).$$

The following the same estimations, we have

$$\frac{d}{dt} \mathbb{E}[\|\tilde{u}_t^{(i)}\|^2] \leq -2\left(\frac{1}{h_{T-t}} - 1\right) \mathbb{E}[\|\tilde{u}_t^{(i)}\|^2] - \frac{4}{h_{T-t}} \langle \tilde{u}_t^{(i)}, (U_{T-t}^{(i)})^\top e_A(T-t, \tilde{Y}_t) \rangle + \tilde{\epsilon}_{T-t}^{(i)},$$

where  $\tilde{\epsilon}_{T-t}^{(i)} = \mathcal{O}(1)$  as  $t \rightarrow T^-$ . Apply Young's inequality, we have  $\frac{4}{h_{T-t}} \langle \tilde{u}_t^{(i)}, (U_{T-t}^{(i)})^\top e_A(T-t, \tilde{Y}_t) \rangle \leq \frac{1}{h_{T-t}} \|\tilde{u}_t^{(i)}\|^2 + \frac{4}{h_{T-t}} \|(U_{T-t}^{(i)})^\top e_A(T-t, \tilde{Y}_t)\|^2$ . Therefore,

$$\frac{d}{dt} \mathbb{E}[\|\tilde{u}_t^{(i)}\|^2] \leq -\left(\frac{1}{h_{T-t}} - 2\right) \mathbb{E}[\|\tilde{u}_t^{(i)}\|^2] + \frac{4}{h_{T-t}} \|(U_{T-t}^{(i)})^\top e_A(T-t, \tilde{Y}_t)\|^2 + \tilde{\epsilon}_{T-t}^{(i)}.$$

Apply Gronwall's inequality and we get

$$\begin{aligned} \mathbb{E}[\|\tilde{u}_t^{(i)}\|^2] &\leq \exp\left(-\int_{\tilde{t}_{\text{in}}}^t \frac{1}{h_{T-u}} - 2 \right) \mathbb{E}[\|\tilde{u}_{\tilde{t}_{\text{in}}}^{(i)}\|^2] + \int_{\tilde{t}_{\text{in}}}^t \exp\left(-\int_u^t \frac{1}{h_{T-s}} - 2 \right) \epsilon_{T-u}^{(i)} du \\ &\quad + \int_{\tilde{t}_{\text{in}}}^t \exp\left(-\int_u^t \frac{1}{h_{T-s}} - 2 \right) \frac{4}{h_{T-u}} \|(U_{T-u}^{(i)})^\top e_A(T-u, \tilde{Y}_u)\|^2 du. \end{aligned}$$

When  $t = T - \delta$  and  $\delta \ll 1$ , we have

$$\begin{aligned} &\int_{\tilde{t}_{\text{in}}}^{T-\delta} \exp\left(-\int_u^{T-\delta} \frac{1}{h_{T-s}} - 2 \right) \epsilon_{T-u}^{(i)} du = \mathcal{O}(\sqrt{\delta}), \\ &\int_{\tilde{t}_{\text{in}}}^{T-\delta} \exp\left(-\int_u^{T-\delta} \frac{1}{h_{T-s}} - 2 \right) \frac{4}{h_{T-u}} \|(U_{T-u}^{(i)})^\top e_A(T-u, \tilde{Y}_u)\|^2 du \\ &= \mathcal{O}(\sqrt{\delta} \int_{\tilde{t}_{\text{in}}}^{T-\delta} h_{T-t}^{-\frac{3}{2}} \|(U_{T-u}^{(i)})^\top e_A(T-u, \tilde{Y}_u)\|^2 du). \end{aligned}$$

□

**Remark F.1** (Tangential distribution of the residual). *To study the distribution of residual  $\tilde{Y}_{T-\delta} - m_\delta^{(i)}$  along the tangent direction, we look at the SDE of  $\|\tilde{u}_t^{(i)}\|^2$  and only look at the leading order drift as  $t \rightarrow T^-$  and the diffusion term:*

$$\begin{aligned} d\|\tilde{u}_t^{(i)}\|^2 &= -2\left(\frac{2}{h_{T-t}} - 1\right) \|\tilde{u}_t^{(i)}\|^2 dt + 2\langle u_t^{(i)}, \partial_t (U_{T-t}^{(i)})^\top (Y_t - m_{T-t}^{(i)}) \rangle dt \\ &\quad + 2\langle \tilde{u}_t^{(i)}, (U_{T-t}^{(i)})^\top (b_A(T-t, \tilde{Y}_t) - (\tilde{Y}_t + \frac{2}{h_{T-t}}(m_{T-t}^{(i)} - \tilde{Y}_t))) \rangle dt \end{aligned}$$

$$\begin{aligned}
& + 2d^*dt + 2\sqrt{2}\langle \tilde{u}_t^{(i)}, (U_{T-t}^{(i)})^\top d\tilde{B}_t \rangle \\
& = -\frac{4}{h_{T-t}}\|\tilde{u}_t^{(i)}\|^2 dt - \frac{4}{h_{T-t}}\langle \tilde{u}_t^{(i)}, (U_{T-t}^{(i)})^\top e_A(T-t, \tilde{Y}_t) \rangle dt \\
& \quad + \mathcal{O}(1)dt + 2\sqrt{2}\langle \tilde{u}_t^{(i)}, (U_{T-t}^{(i)})^\top d\tilde{B}_t \rangle
\end{aligned}$$

which implies

$$d\tilde{u}_t^{(i)} = -\underbrace{\frac{2}{h_{T-t}}(\tilde{u}_t^{(i)} + (U_{T-t}^{(i)})^\top e_A(T-t, \tilde{Y}_t))dt + \sqrt{2}d\tilde{B}_t}_{\text{dominant drift}} + \mathcal{O}(1)dt.$$

Notice that

$$\tilde{Y}_t = m_{T-t}^{(i)} + U_{T-t}^{(i)}\tilde{u}_t^{(i)} + \underbrace{(I_d - U_{T-t}^{(i)}(U_{T-t}^{(i)})^\top)(Y_t - m_{T-t}^{(i)})}_{\text{normal component}}$$

Assume the normal component is negligible, then we have

$$(U_{T-t}^{(i)})^\top e_A(T-t, \tilde{Y}_t) \approx (U_{T-t}^{(i)})^\top e_A(T-t, m_{T-t}^{(i)} + U_{T-t}^{(i)}\tilde{u}_t^{(i)}).$$

Then the approximate SDE for  $\tilde{u}_t^{(i)}$  is given by

$$d\tilde{u}_t^{(i)} = -\frac{2}{h_{T-t}}(\tilde{u}_t^{(i)} + (U_{T-t}^{(i)})^\top e_A(T-t, m_{T-t}^{(i)} + U_{T-t}^{(i)}\tilde{u}_t^{(i)}))dt + \sqrt{2}d\tilde{B}_t. \quad (21)$$

**Lemma F.1.** Under Assumption 1, if  $x \in \mathcal{B}_{T-t}^{(i)}(\eta_{T-t})$ , then

$$\|b(T-t, x) - (x + \frac{2}{h_{T-t}}(m_{T-t}^{(i)} - x))\| \leq 4Ra_{T-t}h_{T-t}^{-1}\theta_{T-t}.$$

*Proof of Lemma F.1.* According to Lemma C.3, we have

$$m(T-t, x) - m_{T-t}^{(i)} = \sum_{j \neq i} \text{Softmax}(-\frac{\|x - m_{T-t}\|^2}{2h_{T-t}})_j a_{T-t}(x_0^{(i)} - x_0^{(i)}).$$

Under Assumption 1 and the definition of  $\mathcal{B}_{T-t}^{(i)}(\eta_{T-t})$ , we immediately have  $\|m(T-t, x) - m_{T-t}^{(i)}\| \leq 2Ra_{T-t}\theta_{T-t}$ . Therefore,

$$\begin{aligned}
& \|b(T-t, x) - (x + \frac{2}{h_{T-t}}(m_{T-t}^{(i)} - x))\| \\
& = \|x + \frac{2}{h_{T-t}}(m(T-t, x) - x) - (x + \frac{2}{h_{T-t}}(m_{T-t}^{(i)} - x))\| \\
& = \frac{2}{h_{T-t}}\|m(T-t, x) - m_{T-t}^{(i)}\| \leq 4Ra_{T-t}h_{T-t}^{-1}\theta_{T-t}.
\end{aligned}$$

□

**Lemma F.2.** The local tangent frame  $U_t^{(i)}$  satisfies the following properties:

$$(I) \quad \langle u, (\partial_t U_t^{(i)})^\top U_t^{(i)} u \rangle = 0 \text{ for any } u \in \mathbb{R}^{d^*};$$

*Proof of Lemma F.2.* Starting from  $(U_t^{(i)})^\top U_t^{(i)} = I_{d^*}$  and take derivative wrt.  $t$  on both side and we get

$$(\partial_t U_t^{(i)})^\top U_t^{(i)} = -((\partial_t U_t^{(i)})^\top U_t^{(i)})^\top.$$

Therefore,  $(\partial_t U_t^{(i)})^\top U_t^{(i)}$  is skew-symmetric. Hence we proved (1). □

## G From Inference to Training

This section converts the error-bound terms in Theorems 3.2 and 3.3, which are expectations along the simulated inference path  $\tilde{Y}_t$ , into quantities that depend only on the exact reverse-time OU path  $X_t^\leftarrow$ . The key tool is a change of measure (Girsanov's theorem). A minor technical issue is that  $\tilde{Y}_0 \sim \mathcal{N}(0, I_d)$  while  $X_0^\leftarrow \sim p_T$ . To isolate the initialization error, we introduce an auxiliary process  $\hat{Y}_t$  that shares the transition kernel with  $\tilde{Y}_t$  but starts from the correct initialization  $p_T$ .

**Reverse-time processes.** Let  $e_A(t, x) := m_A(t, x) - m(t, x)$ . Consider the following reverse-time processes on  $[0, T - \delta]$ :

$$\begin{aligned} dX_t^\leftarrow &= \underbrace{\left( X_t^\leftarrow - \frac{2}{h_{T-t}} X_t^\leftarrow + \frac{2}{h_{T-t}} m(T-t, X_t^\leftarrow) \right) dt + \sqrt{2} dB_t^\leftarrow }_{b(T-t, X_t^\leftarrow)}, \quad X_0^\leftarrow \sim p_T, \\ d\hat{Y}_t &= \underbrace{\left( \hat{Y}_t - \frac{2}{h_{T-t}} \hat{Y}_t + \frac{2}{h_{T-t}} m_A(T-t, \hat{Y}_t) \right) dt + \sqrt{2} d\tilde{B}_t }_{:=b_A(T-t, \hat{Y}_t)}, \quad \hat{Y}_0 \sim p_T, \\ d\tilde{Y}_t &= \underbrace{\left( \tilde{Y}_t - \frac{2}{h_{T-t}} \tilde{Y}_t + \frac{2}{h_{T-t}} m_A(T-t, \tilde{Y}_t) \right) dt + \sqrt{2} d\tilde{B}_t }_{:=b_A(T-t, \tilde{Y}_t)}, \quad \tilde{Y}_0 \sim \mathcal{N}(0, I_d). \end{aligned}$$

We denote the path measures of  $X_t^\leftarrow$  and  $\hat{Y}_t$  respectively by  $\mathbb{P}$  and  $\mathbb{Q}$ . Since  $X_0^\leftarrow$  and  $\hat{Y}_0$  have the same initial distribution, we can apply Girsanov's theorem without evolving extra initial-density ratio factor. The remaining gap between  $\tilde{Y}_t$  and  $\hat{Y}_t$  is purely from initialization, and it will be controlled since  $p_T$  is close to  $\mathcal{N}(0, I_d)$  when  $T$  is large.

**Assumption 3.** *We assume the following hold:*

- (0) *Novikov's condition:*  $\exp\left(2 \int_0^{T-\delta} \frac{\|e_A(T-s, X_t^\leftarrow)\|^2}{h_{T-s}^2} ds\right) < \infty$ ;
- (1) *Bound  $\chi^2$  along trajectory:*  $\sup_{t \in [0, T-\delta]} \chi^2(\mathbb{Q}_t | \mathbb{P}_t) \leq C_\chi^2 = \mathcal{O}(1)$ ;
- (2) *Normal/tangent posterior mean error satisfies:* for any  $\dagger \in \{\perp, \parallel\}$ ,  $\mathbb{E}[\|e_A^\dagger(T-t, X_t^\leftarrow)\|^4]^{\frac{1}{2}} \leq C_m \mathbb{E}[\|e_A^\dagger(T-t, X_t^\leftarrow)\|^2]$  for some  $C_m = \mathcal{O}(1)$ ;
- (3) *Uniform boundedness of the weighted posterior mean error:*

$$\sup_{t \in [0, T-\delta]} \sup_{x \in \mathcal{T}_{T-t}(\rho_{T-t})} \frac{w(T-t) \|e_A(T-t, x)\|^2}{h_{T-t}^2} \leq \frac{C_u}{T-\delta}$$

for some  $C_u = \mathcal{O}(1)$  and decreasing weight  $t \mapsto w(t)$ .

**Theorem G.1.** *Under Assumption 3, the normal/tangent-error floors in Theorems 3.2 and 3.3 can be estimated by the projected posterior mean matching loss in normal/tangent direction, i.e.,*

$$\text{normal-error floor} \lesssim C_\delta^\perp \int_\delta^T \frac{w(t) \mathbb{E}[\|e_A^\perp(t, X_t)\|^2]}{h_t^2} dt + C_\delta^\perp (\sqrt{d} + R) e^{-T} + d\delta^c, \quad (22)$$

$$\text{tangent-error floor} \lesssim C_\delta^\parallel \int_\delta^T \frac{\mathbb{E}[w(t) \|e_A^\parallel(t, X_t)\|^2]}{h_t^2} dt + C_\delta^\parallel (\sqrt{d} + R) e^{-T} + d\delta^{\frac{1}{2}}. \quad (23)$$

where  $C_\delta^\perp := \delta^c (1 \vee \frac{\delta^{1-c}}{w(\delta)})$  ( $c = \lim_{t \rightarrow \delta^+} h_t \beta_t$ ) and  $C_\delta^\parallel = \sqrt{\delta} (1 \vee \frac{\sqrt{\delta}}{w(\delta)})$ .

*Proof of Theorem G.1.* Applying Girsanov's Theorem, define  $\mathcal{L}_t := \sqrt{2} \int_0^t \frac{e_A(T-s, X_s^\leftarrow)}{h_{T-s}} dB_s^\leftarrow$  and according to Assumption 3-(0), we have  $\mathcal{E}(\mathcal{L})_t := \exp(\mathcal{L}_t - \frac{1}{2}[\mathcal{L}]_t)$  is a  $\mathbb{P}$ -martingale and

$$t \mapsto B_t^\leftarrow - \sqrt{2} \int_0^t \frac{e_A(T-s, X_s^\leftarrow)}{h_{T-s}} ds$$

is a Brownian motion under  $\mathcal{E}(\mathcal{L})_{T-\delta}\mathbb{P}$  and  $\mathbb{Q} = \mathcal{E}(\mathcal{L})_{T-\delta}\mathbb{P}$ . Therefore, we can change the path measure from  $\mathbb{Q}$  to  $\mathbb{P}$ , hence relating the inference bounds to the training error.

Recall that with  $e_A(t, x) = m_A(t, x) - m(t, x)$  and  $e_A^\perp(t, x) = P_t^\perp(x)e_A(t, x)$ . When  $\beta_t = c/h_t$  for some  $c \in [1/2, 1)$ , the normal-error term related to training in Theorem 3.2 is

$$\begin{aligned} & \int_{\tilde{t}_{\text{in}}}^{T-\delta} \exp(-2 \int_u^{T-\delta} (\beta_{T-s} - 1) ds) \frac{\mathbb{E}[\|e_A^\perp(T-u, \tilde{Y}_u)\|^2]}{h_{T-u}^2 \beta_{T-u}} du \\ & \lesssim \delta^c \int_{\tilde{t}_{\text{in}}}^{T-\delta} \frac{h_{T-t}^{1-c}}{w(T-t)} \frac{w(T-t) \mathbb{E}[\|e_A^\perp(T-t, \tilde{Y}_t)\|^2]}{h_{T-t}^2} dt \\ & \lesssim \delta^c (1 \vee \frac{\delta^{1-c}}{w(\delta)}) \int_{\tilde{t}_{\text{in}}}^{T-\delta} \frac{w(T-t) \mathbb{E}[\|e_A^\perp(T-t, \tilde{Y}_t)\|^2]}{h_{T-t}^2} dt, \end{aligned}$$

WLOG, assume that  $\tilde{t}_{\text{in}} = 0$ . According to Girsanov's theorem,

$$\begin{aligned} & \int_0^{T-\delta} \frac{\mathbb{E}[w(T-t) \|e_A^\perp(T-t, \tilde{Y}_t)\|^2]}{h_{T-t}^2} dt \\ & = \int_0^{T-\delta} \frac{w(T-t) \mathbb{E}[\|e_A^\perp(T-t, \tilde{Y}_t)\|^2] - \|e_A^\perp(T-t, \hat{Y}_t)\|^2}{h_{T-t}^2} dt \\ & \quad + \int_0^{T-\delta} \frac{w(T-t) \mathbb{E}[\mathcal{E}(\mathcal{L})_t \|e_A^\perp(T-t, X_t^\leftarrow)\|^2]}{h_{T-t}^2} dt. \end{aligned}$$

Notice that

$$\begin{aligned} \mathbb{E}[\mathcal{E}(\mathcal{L})_t \|e_A^\perp(T-t, X_t^\leftarrow)\|^2] & = \mathbb{E}[\|e_A^\perp(T-t, X_t^\leftarrow)\|^2] + \mathbb{E}[(\mathcal{E}(\mathcal{L})_t - 1) \|e_A^\perp(T-t, X_t^\leftarrow)\|^2] \\ & \leq \mathbb{E}[\|e_A^\perp(T-t, X_t^\leftarrow)\|^2] + \mathbb{E}[(\mathcal{E}(\mathcal{L})_t - 1)^2]^{\frac{1}{2}} \mathbb{E}[\|e_A^\perp(T-t, X_t^\leftarrow)\|^4]^{\frac{1}{2}} \\ & = \mathbb{E}[\|e_A^\perp(T-t, X_t^\leftarrow)\|^2] + \sqrt{\chi^2(\mathbb{Q}_t | \mathbb{P}_t)} \mathbb{E}[\|e_A^\perp(T-t, X_t^\leftarrow)\|^4]^{\frac{1}{2}} \end{aligned}$$

Under Assumption 3-(1)(2), we have

$$\int_0^{T-\delta} \frac{w(T-t) \mathbb{E}[\mathcal{E}(\mathcal{L})_t \|e_A^\perp(T-t, X_t^\leftarrow)\|^2]}{h_{T-t}^2} dt \leq (1 + C_\chi C_m) \int_0^{T-\delta} \frac{w(T-t) \mathbb{E}[\|e_A^\perp(T-t, X_t^\leftarrow)\|^2]}{h_{T-t}^2} dt.$$

Meanwhile, under Assumption 3-(3), we have

$$\int_0^{T-\delta} \frac{w(T-t) \mathbb{E}[\|e_A^\perp(T-t, \tilde{Y}_t)\|^2] - \|e_A^\perp(T-t, \hat{Y}_t)\|^2}{h_{T-t}^2} dt \leq C_u \text{TV}(\mathcal{N}(0, I_d), p_T) \lesssim (\sqrt{d} + R) e^{-T}.$$

Therefore, the normal-error floor for aligning can be estimated as

$$\delta^c (1 \vee \frac{\delta^{1-c}}{w(\delta)}) \int_0^{T-\delta} \frac{\mathbb{E}[\|e_A^\perp(T-u, \tilde{Y}_u)\|^2]}{h_{T-u}^2} du$$

$$\lesssim \delta^c \left(1 \vee \frac{\delta^{1-c}}{w(\delta)}\right) \int_0^{T-\delta} \frac{w(T-t) \mathbb{E}[\|e_A^\perp(T-t, X_t^\leftarrow)\|^2]}{h_{T-t}^2} dt + \delta^c \left(1 \vee \frac{\delta^{1-c}}{w(\delta)}\right) (\sqrt{d} + R) e^{-T}.$$

Similarly, along the tangent direction, the tangent floor is of the form

$$\begin{aligned} & \int_{\tilde{t}_{\text{in}}}^{T-\delta} \exp \left( - \int_u^{T-\delta} \frac{1}{h_{T-s}} - 2ds \right) \frac{4}{h_{T-u}} \|(U_{T-u}^{(i)})^\top e_A(T-u, \tilde{Y}_u)\|^2 du \\ & \lesssim \sqrt{\delta} \left(1 \vee \frac{\sqrt{\delta}}{w(\delta)}\right) \int_{\tilde{t}_{\text{in}}}^{T-\delta} \frac{w(T-u) \mathbb{E}[\|(U_{T-u}^{(i)})^\top e_A(T-u, \tilde{Y}_u)\|^2]}{h_{T-u}^2} du, \end{aligned}$$

where the order estimation follows from the choice of  $\beta_t = \Theta(1/h_t)$ . When  $\tilde{Y}_t \in \mathcal{T}_{T-t}(\rho_{T-t}) \cap \mathcal{B}^{(i)}(\theta_{T-t})$  and  $t \rightarrow T - \delta$ , we have  $U_{T-t}^{(i)}(U_{T-t}^{(i)})^\top \approx P_{T-t}^{\parallel}(m_{T-t}^{(i)}) \approx P_{T-t}^{\parallel}(\tilde{Y}_t)$ . Hence we can use the following tangent error to reflect the tangent-floor of the sliding phase:

$$\begin{aligned} & \sqrt{\delta} \left(1 \vee \frac{\sqrt{\delta}}{w(\delta)}\right) \int_{\tilde{t}_{\text{in}}}^{T-\delta} \frac{w(T-t) \mathbb{E}[\|P_{T-t}^{\parallel}(\tilde{Y}_t) e_A(T-t, \tilde{Y}_t)\|^2]}{h_{T-t}^2} dt \\ & := \sqrt{\delta} \left(1 \vee \frac{\sqrt{\delta}}{w(\delta)}\right) \int_{\tilde{t}_{\text{in}}}^{T-\delta} \frac{w(T-t) \mathbb{E}[\|e_A^{\parallel}(T-t, \tilde{Y}_t)\|^2]}{h_{T-t}^2} dt. \end{aligned}$$

Then following the same change of measure discussion, the tangent-error floor for sliding can be estimated as

$$\begin{aligned} & \sqrt{\delta} \left(1 \vee \frac{\sqrt{\delta}}{w(\delta)}\right) \int_0^{T-\delta} \frac{w(T-u) \mathbb{E}[\|e_A^{\parallel}(T-u, \tilde{Y}_u)\|^2]}{h_{T-u}^2} du \\ & \lesssim \sqrt{\delta} \left(1 \vee \frac{\sqrt{\delta}}{w(\delta)}\right) \int_0^{T-\delta} \frac{w(T-t) \mathbb{E}[\|e_A^{\parallel}(T-t, X_t^\leftarrow)\|^2]}{h_{T-t}^2} dt + \sqrt{\delta} \left(1 \vee \frac{\sqrt{\delta}}{w(\delta)}\right) (\sqrt{d} + R) e^{-T}. \end{aligned}$$

Last, the theorem follows from writing the reverse-time OU  $X_t^\leftarrow$  into the forward-time OU  $X_t$  and adding the contraction terms depending on  $d, R$  in Theorems 3.2 and 3.3.  $\square$

## H Analysis of the Training Process

Recall from (7) that

$$A_{k+1} = A_k(I_p - 2\eta\tilde{U}) + 2\eta\tilde{V},$$

with  $U_t = \mathbb{E}[\sigma_t(X_t(z))\sigma_t(X_t(z))^\top] \in \mathbb{R}^{p \times p}$  and  $V_t = \mathbb{E}_z[a_t X_0 \sigma_t(X_t(z))^\top] \in \mathbb{R}^{d \times p}$

$$\tilde{U} = \int_{\delta}^T \frac{w(t)}{h_t^2} \frac{\mathbb{E}[\sigma_t(X_t(z))\sigma_t(X_t(z))^\top]}{p} dt, \quad \tilde{V} = \int_{\delta}^T \frac{w(t)}{h_t^2} \frac{\mathbb{E}[a_t X_0 \sigma_t(X_t(z))^\top]}{\sqrt{p}} dt.$$

$\tilde{U}$  is the RFNN kernel matrix in (7) with rank  $r \leq p$  and eigen-decomposition  $\tilde{U} = \sum_{j=1}^r \lambda_j u_j u_j^\top$  with  $\{u_j\}_{j \in [r]}$  being a set of orthonormal vectors in  $\mathbb{R}^p$  and  $\lambda_1 > \lambda_2 > \dots > \lambda_r > 0$ .

We first provide initialization-dependent expressions for  $A_k$  and the equilibrium of gradient descent.

Apply the iteration recursively and we get

$$A_k = A_0(I_p - 2\eta\tilde{U})^k + 2\eta\tilde{V} \sum_{j=0}^{k-1} (I_p - 2\eta\tilde{U})^j.$$

If  $2\eta\|\tilde{U}\| \leq 1$ , the gradient descent is stable. As  $k \rightarrow \infty$ ,

$$A_k \rightarrow A_\infty = A_0(I_p - \tilde{U}\tilde{U}^+) + \tilde{V}\tilde{U}^+,$$

where  $\tilde{U}^+$  is the pseudo-inverse of  $\tilde{U}$ .

Next, we present the error decomposition of  $\mathcal{L}_{\text{MM}}(A_k)$  into architecture-driven error and optimization-driven error.

**Proposition H.1.** *Let  $\{A_k\}$  be the matrix iterates from gradient descent (7) with learning rate  $\eta < 2/\lambda_1$  and initialization  $A_0$ , then the  $\mathcal{L}_{\text{MM}}$  can be decomposed as*

$$\mathcal{L}_{\text{MM}}(A_k) = \text{Err}_{\text{arc}} + \text{Err}_{\text{train}}(k), \quad \mathcal{L}_{\text{MM}}(A_\infty) = \text{Err}_{\text{arc}},$$

with

$$\begin{aligned} \text{Err}_{\text{arc}} &= \int_{\delta}^T \frac{w(t)}{h_t^2} \mathbb{E}[\|m(t, X_t(z)) - \frac{\tilde{V}\tilde{U}^+}{\sqrt{p}}\sigma_t(X_t(z))\|^2] dt, \\ \text{Err}_{\text{train}}(k) &= \sum_{i=1}^r \lambda_i(1 - 2\eta\lambda_i)^{2k} \|a_i\|^2, \end{aligned}$$

and  $a_j = (A_0 - \tilde{V}\tilde{U}^+)u_j \in \mathbb{R}^d$  for all  $j \in [r]$ .

*Proof of Proposition H.1.* Based on the dynamics of  $\{A_k\}_{k \geq 0}$ , we can study the dynamics of the DMM loss  $\{\mathcal{L}_{\text{DMM}}(A_k)\}_{k \geq 0}$ . According to (4), we have

$$\begin{aligned} \mathcal{L}_{\text{DMM}}(A) &= \int_{\delta}^T \frac{w(t)}{h_t^2} \mathbb{E}[\| -a_t X_0 + \frac{A}{\sqrt{p}}\sigma_t(X_t(z))\|^2] dt \\ &= \int_{\delta}^T \frac{w(t)}{h_t^2} \mathbb{E}[\| -a_t X_0 \|^2] dt + \int_{\delta}^T \frac{w(t)}{h_t^2} \mathbb{E}[\| \frac{A}{\sqrt{p}}\sigma_t(X_t(z)) \|^2] dt \\ &\quad - 2 \int_{\delta}^T \frac{w(t)}{h_t^2} \mathbb{E}[\langle a_t X_0, \frac{A}{\sqrt{p}}\sigma_t(X_t(z)) \rangle] dt \\ &= C + \text{trace}(A\tilde{U}A^\top) - 2\text{trace}(A\tilde{V}^\top), \end{aligned} \tag{24}$$

where the constant  $C = \int_{\delta}^T \frac{w(t)}{h_t^2} \mathbb{E}[\|a_t X_0\|^2] dt$  is independent to  $A$ . Notice that  $\nabla_A \mathcal{L}_{\text{DMM}}(A) = 2(A\tilde{U} - \tilde{V})$ . Therefore, the equilibrium satisfy  $A^*$  satisfy  $A^*\tilde{U} = \tilde{V}$  and they share the same DMM loss value  $\mathcal{L}_{\text{DMM}}(A^*)$ . Next, we study the decay of DMM loss along gradient descent by tracking  $\mathcal{L}_{\text{DMM}}(A_k) - \mathcal{L}_{\text{DMM}}(A^*)$ . Define  $\Delta A_k = A_k - A^*$ , according to (24), we have

$$\begin{aligned} \mathcal{L}_{\text{DMM}}(A_k) &= C + \text{trace}((A^* + \Delta A_k)\tilde{U}(A^* + \Delta A_k)^\top) - 2\text{trace}((A^* + \Delta A_k)\tilde{V}^\top) \\ &= C + \text{trace}(A^*\tilde{U}(A^*)^\top) - 2\text{trace}(A^*\tilde{V}^\top) + \text{trace}(\Delta A_k \tilde{U} \Delta A_k^\top) \\ &\quad + 2(\text{trace}(\Delta A_k \tilde{U} (A^*)^\top) - \text{trace}(\Delta A_k \tilde{V}^\top)) \\ &= \mathcal{L}_{\text{DMM}}(A^*) + \text{trace}(\Delta A_k \tilde{U} \Delta A_k^\top) \\ &= \mathcal{L}_{\text{DMM}}(A^*) + \|\Delta A_k \tilde{U}^{\frac{1}{2}}\|_F^2, \end{aligned}$$

where the last part in the second equation cancel due to the property of the equilibrium  $A^*$ . Meanwhile, according to the iteration formula, we can easily get that

$$\Delta A_{k+1} = A_{k+1} - A^* = \Delta A_k(I_p - 2\eta\tilde{U}) + 2\eta(A^*\tilde{U} + \tilde{V}) = \Delta A_k(I_p - 2\eta\tilde{U}),$$

where the last identity follows from the property of the equilibrium  $A^*$ . Combined with our equation of  $\mathcal{L}_{\text{DMM}}(A_k)$ , we have

$$\mathcal{L}_{\text{DMM}}(A_k) = \mathcal{L}_{\text{DMM}}(A^*) + \|\Delta A_k \tilde{U}^{\frac{1}{2}}\|_F^2 = \mathcal{L}_{\text{DMM}}(A^*) + \|\Delta A_0 (I_p - 2\eta \tilde{U})^k \tilde{U}^{\frac{1}{2}}\|_F^2.$$

Therefore, based on the spectral information of  $\tilde{U}$  and  $A_0$ , we can represent the DMM loss along gradient descent as follows

$$\mathcal{L}_{\text{DMM}}(A_k) = \mathcal{L}_{\text{DMM}}(A^*) + \sum_{i=1}^r \lambda_i (1 - 2\eta \lambda_i)^{2k} \|a_i\|^2. \quad (25)$$

In order to look at a loss with minimum strictly zero, we need to go back to the (non-denoising) posterior mean matching loss, i.e.,  $\mathcal{L}_{\text{MM}}(A) = \int_{\delta}^T \frac{w(t)}{h_t^2} \mathbb{E}[\| - a_t X_0 + \frac{A}{\sqrt{p}} \sigma_t(X_t(z)) \|^2] dt$ . The DMM loss  $\mathcal{L}_{\text{DMM}}$  can be easily related to  $\mathcal{L}_{\text{MM}}$ :

$$\begin{aligned} \mathcal{L}_{\text{DMM}}(A) &= \int_{\delta}^T \frac{w(t)}{h_t^2} \mathbb{E}[\| - a_t X_0 + \frac{A}{\sqrt{p}} \sigma_t(X_t(z)) \|^2] dt \\ &= \int_{\delta}^T \frac{w(t)}{h_t^2} \mathbb{E}[\| - m(t, X_t(z)) + \frac{A}{\sqrt{p}} \sigma_t(X_t(z)) \|^2] dt \\ &\quad + \int_{\delta}^T \frac{w(t)}{h_t^2} \mathbb{E}[\| - a_t X_0 + m(t, X_t(z)) \|^2] dt \\ &\quad + \underbrace{2 \int_{\delta}^T \frac{w(t)}{h_t^2} \mathbb{E}[\langle m(t, X_t(z)) - a_t X_0, \frac{A}{\sqrt{p}} \sigma_t(X_t(z)) \rangle] dt}_{\text{cross term}} \\ &= \mathcal{L}_{\text{MM}}(A) + \int_{\delta}^T \frac{w(t)}{h_t^2} \mathbb{E}[\| - a_t X_0 + m(t, X_t(z)) \|^2] dt, \end{aligned}$$

where the cross term is canceled based on definition of  $m(t, x) = \mathbb{E}[a_t X_0 | X_t = x]$  and the tower property. Therefore, we can derive a decomposition of  $\mathcal{L}_{\text{MM}}(A_k)$  along the gradient descent dynamics:

$$\begin{aligned} \mathcal{L}_{\text{MM}}(A_k) &= \mathcal{L}_{\text{DMM}}(A_k) - \int_{\delta}^T \frac{w(t)}{h_t^2} \mathbb{E}[\| - a_t X_0 + m(t, X_t(z)) \|^2] dt \\ &= \sum_{i=1}^r \lambda_i (1 - 2\eta \lambda_i)^{2k} \|a_i\|^2 + \mathcal{L}_{\text{DMM}}(A^*) - \int_{\delta}^T \frac{w(t)}{h_t^2} \mathbb{E}[\| - a_t X_0 + m(t, X_t(z)) \|^2] dt \\ &= \sum_{i=1}^r \lambda_i (1 - 2\eta \lambda_i)^{2k} \|a_i\|^2 + \int_{\delta}^T \frac{w(t)}{h_t^2} \mathbb{E}[\langle a_t X_0, a_t X_0 - \frac{A^*}{\sqrt{p}} \sigma_t(X_t(z)) \rangle] dt \\ &\quad - \int_{\delta}^T \frac{w(t)}{h_t^2} \mathbb{E}[\| - a_t X_0 + m(t, X_t(z)) \|^2] dt \\ &= \sum_{i=1}^r \lambda_i (1 - 2\eta \lambda_i)^{2k} \|a_i\|^2 + \int_{\delta}^T \frac{w(t)}{h_t^2} \mathbb{E}[\langle m(t, X_t(z)), m(t, X_t(z)) - \frac{A^*}{\sqrt{p}} \sigma_t(X_t(z)) \rangle] dt \\ &= \sum_{i=1}^r \lambda_i (1 - 2\eta \lambda_i)^{2k} \|a_i\|^2 + \int_{\delta}^T \frac{w(t)}{h_t^2} \mathbb{E}[\|m(t, X_t(z)) - \frac{A^*}{\sqrt{p}} \sigma_t(X_t(z))\|^2] dt, \end{aligned} \quad (27)$$

where the second last property follows from the tower property and the last identity follows from the property of  $A^*$  and the tower property. Therefore, Equation (26) decompose the posterior mean error into two parts which induce different type of implicit bias.

(1) Architecture Implicit Bias: the term  $\int_{\delta}^T \frac{w(t)}{h_t^2} \mathbb{E}[\|m(t, X_t(z)) - \frac{A^*}{\sqrt{p}} \sigma_t(X_t(z))\|^2] dt$  orients from the inadequate representation ability of the RFNN with finite  $p$ . Even though the equilibrium  $A^*$  can be any matrix of the form  $A_0(I_p - \tilde{U}\tilde{U}^+) + \tilde{V}\tilde{U}^+$  (depending on initialization), the value of the architecture implicit bias stays the same. Therefore, we can pick a special  $A^* = \tilde{V}\tilde{U}^+$  to represent it, i.e.,

$$\text{Err}_{arc} = \int_{\delta}^T \frac{w(t)}{h_t^2} \mathbb{E}[\|m(t, X_t(z)) - \frac{\tilde{V}\tilde{U}^+}{\sqrt{p}} \sigma_t(X_t(z))\|^2] dt.$$

(2) Training Dynamical Implicit Bias: the term  $\sum_{i=1}^r \lambda_i (1 - 2\eta\lambda_i)^{2k} \|a_i\|^2$  is produced by running the optimization algorithm for finite time. If we can ideally run the gradient descent for infinite many step, this bias will vanish. We represent the training dynamical bias as follows

$$\text{Err}_{train}(k) = \sum_{i=1}^r \lambda_i (1 - 2\eta\lambda_i)^{2k} \|a_i\|^2.$$

□

Based on Proposition H.1, we can proceed to prove Theorem 4.2.

*Proof of Theorem 4.2.* The decomposition of training dynamical/architecture implicit bias requires to repeat our analysis to the total DMM loss.

$$\begin{aligned} \mathcal{L}_{\text{DMM}}^{\perp}(A) &:= \int_{\delta}^T \frac{w(t)}{h_t^2} \mathbb{E}[\|P_t^{\perp}(X_t(z))(-a_t X_0 + \frac{A}{\sqrt{p}} \sigma_t(X_t(z)))\|^2] dt \\ &= \underbrace{\int_{\delta}^T \frac{w(t)}{h_t^2} \mathbb{E}[\|P_t^{\perp}(X_t(z))(-a_t X_0)\|^2] dt}_{:= C^{\perp}} + \underbrace{\int_{\delta}^T \frac{w(t)}{h_t^2} \mathbb{E}[\|P_t^{\perp}(X_t(z))(\frac{A}{\sqrt{p}} \sigma_t(X_t(z)))\|^2] dt}_{\text{quadratic in } A} \\ &\quad - 2 \underbrace{\int_{\delta}^T \frac{w(t)}{h_t^2} \mathbb{E}[\langle P_t^{\perp}(X_t(z))(a_t X_0), \frac{A}{\sqrt{p}} \sigma_t(X_t(z)) \rangle] dt}_{\text{linear in } A}. \end{aligned}$$

Then we have

$$\begin{aligned} \mathcal{L}_{\text{DMM}}^{\perp}(A_k) &= \mathcal{L}_{\text{DMM}}^{\perp}(A^* + \Delta A_k) \\ &= C^{\perp} + \int_{\delta}^T \frac{w(t)}{h_t^2} \mathbb{E}[\|P_t^{\perp}(X_t(z))(\frac{A^* + \Delta A_k}{\sqrt{p}} \sigma_t(X_t(z)))\|^2] dt \\ &\quad - 2 \int_{\delta}^T \frac{w(t)}{h_t^2} \mathbb{E}[\langle P_t^{\perp}(X_t(z))(a_t X_0), \frac{A^* + \Delta A_k}{\sqrt{p}} \sigma_t(X_t(z)) \rangle] dt \\ &= \mathcal{L}_{\text{DMM}}^{\perp}(A^*) + \int_{\delta}^T \frac{w(t)}{h_t^2} \mathbb{E}[\|P_t^{\perp}(X_t(z))(\frac{\Delta A_k}{\sqrt{p}} \sigma_t(X_t(z)))\|^2] dt \\ &\quad + 2 \int_{\delta}^T \frac{w(t)}{h_t^2} \mathbb{E}[\langle P_t^{\perp}(X_t(z))(\frac{A^*}{\sqrt{p}} \sigma_t(X_t(z)) - a_t X_0), \frac{\Delta A_k}{\sqrt{p}} \sigma_t(X_t(z)) \rangle] dt. \end{aligned}$$

Therefore, the posterior mean loss is

$$\mathcal{L}_{\text{MM}}^{\perp}(A_k) = \mathcal{L}_{\text{DMM}}^{\perp}(A_k) - \int_{\delta}^T \frac{w(t)}{h_t^2} \mathbb{E}[\|P_t^{\perp}(X_t(z))(-a_t X_0 + m(t, X_t(z)))\|^2] dt$$

$$\begin{aligned}
&= \mathcal{L}_{\text{DMM}}^\perp(A^*) + \int_\delta^T \frac{w(t)}{h_t^2} \mathbb{E}[\|P_t^\perp(X_t(z))(\frac{\Delta A_k}{\sqrt{p}}\sigma_t(X_t(z)))\|^2]dt \\
&\quad + 2 \int_\delta^T \frac{w(t)}{h_t^2} \mathbb{E}[\langle P_t^\perp(X_t(z))(\frac{A^*}{\sqrt{p}}\sigma_t(X_t(z)) - a_t X_0), \frac{\Delta A_k}{\sqrt{p}}\sigma_t(X_t(z)) \rangle]dt \\
&\quad - \int_\delta^T \frac{w(t)}{h_t^2} \mathbb{E}[\|P_t^\perp(X_t(z))(-a_t X_0 + m(t, X_t(z)))\|^2]dt \\
&= \int_\delta^T \frac{w(t)}{h_t^2} \mathbb{E}[\|P_t^\perp(X_t(z))(m(t, X_t(z)) - \frac{A^*}{\sqrt{p}}\sigma_t(X_t(z)))\|^2]dt \\
&\quad + \int_\delta^T \frac{w(t)}{h_t^2} \mathbb{E}[\|P_t^\perp(X_t(z))(\frac{\Delta A_k}{\sqrt{p}}\sigma_t(X_t(z)))\|^2]dt \\
&\quad + 2 \int_\delta^T \frac{w(t)}{h_t^2} \mathbb{E}[\langle P_t^\perp(X_t(z))(\frac{A^*}{\sqrt{p}}\sigma_t(X_t(z)) - m(t, X_t(z))), \frac{\Delta A_k}{\sqrt{p}}\sigma_t(X_t(z)) \rangle]dt.
\end{aligned}$$

Similarly, along the tangent directions, we have

$$\begin{aligned}
\mathcal{L}_{\text{MM}}^\parallel(A_k) &= \int_\delta^T \frac{w(t)}{h_t^2} \mathbb{E}[\|P_t^\parallel(X_t(z))(m(t, X_t(z)) - \frac{A^*}{\sqrt{p}}\sigma_t(X_t(z)))\|^2]dt \\
&\quad + \int_\delta^T \frac{w(t)}{h_t^2} \mathbb{E}[\|P_t^\parallel(X_t(z))(\frac{\Delta A_k}{\sqrt{p}}\sigma_t(X_t(z)))\|^2]dt \\
&\quad + 2 \int_\delta^T \frac{w(t)}{h_t^2} \mathbb{E}[\langle P_t^\parallel(X_t(z))(\frac{A^*}{\sqrt{p}}\sigma_t(X_t(z)) - m(t, X_t(z))), \frac{\Delta A_k}{\sqrt{p}}\sigma_t(X_t(z)) \rangle]dt.
\end{aligned}$$

Then along the normal and tangent directions, the architecture implicit bias are

$$\begin{aligned}
\text{Err}_{arc}^\perp &= \int_\delta^T \frac{w(t)}{h_t^2} \mathbb{E}[\|P_t^\perp(X_t(z))(m(t, X_t(z)) - \frac{A^*}{\sqrt{p}}\sigma_t(X_t(z)))\|^2]dt, \\
\text{Err}_{arc}^\parallel &= \int_\delta^T \frac{w(t)}{h_t^2} \mathbb{E}[\|P_t^\parallel(X_t(z))(m(t, X_t(z)) - \frac{A^*}{\sqrt{p}}\sigma_t(X_t(z)))\|^2]dt.
\end{aligned}$$

The training dynamical implicit bias along the tangent directions are

$$\begin{aligned}
\text{Err}_{train}^\perp(k) &= \int_\delta^T \frac{w(t)}{h_t^2} \mathbb{E}[\|P_t^\perp(X_t(z))(\frac{\Delta A_k}{\sqrt{p}}\sigma_t(X_t(z)))\|^2]dt \\
&\quad + 2 \int_\delta^T \frac{w(t)}{h_t^2} \mathbb{E}[\langle P_t^\perp(X_t(z))(\frac{A^*}{\sqrt{p}}\sigma_t(X_t(z)) - m(t, X_t(z))), \frac{\Delta A_k}{\sqrt{p}}\sigma_t(X_t(z)) \rangle]dt, \\
\text{Err}_{train}^\parallel(k) &= \int_\delta^T \frac{w(t)}{h_t^2} \mathbb{E}[\|P_t^\parallel(X_t(z))(\frac{\Delta A_k}{\sqrt{p}}\sigma_t(X_t(z)))\|^2]dt \\
&\quad + 2 \int_\delta^T \frac{w(t)}{h_t^2} \mathbb{E}[\langle P_t^\parallel(X_t(z))(\frac{A^*}{\sqrt{p}}\sigma_t(X_t(z)) - m(t, X_t(z))), \frac{\Delta A_k}{\sqrt{p}}\sigma_t(X_t(z)) \rangle]dt.
\end{aligned}$$

Again, since  $\Delta A_k = \Delta A_0(1 - 2\eta\tilde{U})^k$ , we have  $\frac{\Delta A_k}{\sqrt{p}}\sigma_t(X_t(z)) = \sum_{j=1}^r (1 - 2\eta\lambda_j)^k \frac{u_j^\top \sigma_t(X_t(z))}{\sqrt{p}} a_j := \sum_{j=1}^r (1 - 2\eta\lambda_j)^k \sigma_{t,u_j} a_j$ . Then we have

$$\int_\delta^T \frac{w(t)}{h_t^2} \mathbb{E}[\|P_t^\perp(X_t(z))(\frac{\Delta A_k}{\sqrt{p}}\sigma_t(X_t(z)))\|^2]dt$$

$$\begin{aligned}
&= \sum_{j,l=1}^r (1-2\eta\lambda_j)^k (1-2\eta\lambda_l)^k a_j^\top \int_\delta^T \frac{w(t)}{h_t^2} \mathbb{E}[\sigma_{t,u_j} \sigma_{t,u_l} P_t^\perp(X_t(z))] a_l \\
&:= \sum_{j,l=1}^r (1-2\eta\lambda_j)^k (1-2\eta\lambda_l)^k a_j^\top P_{jl}^\perp a_l \\
&\quad 2 \int_\delta^T \frac{w(t)}{h_t^2} \mathbb{E}[\langle P_t^\perp(X_t(z))(\frac{A^*}{\sqrt{p}}\sigma_t(X_t(z)) - m(t, X_t(z)), \frac{\Delta A_k}{\sqrt{p}}\sigma_t(X_t(z))) \rangle] dt \\
&= 2 \sum_{j=1}^r (1-2\eta\lambda_j)^k a_j^\top \int_\delta^T \frac{w(t)}{h_t^2} \mathbb{E}[\sigma_{t,u_j} P_t^\perp(X_t(z))(\frac{A^*}{\sqrt{p}}\sigma_t(X_t(z)) - m(t, X_t(z))] dt \\
&:= 2 \sum_{j=1}^r (1-2\eta\lambda_j)^k a_j^\top b_j^\perp.
\end{aligned}$$

We can work on the tangent directions similarly. Therefore, we have

$$\begin{aligned}
\text{Err}_{train}^\perp(k) &= \sum_{j,l=1}^r (1-2\eta\lambda_j)^k (1-2\eta\lambda_l)^k a_j^\top P_{jl}^\perp a_l + 2 \sum_{j=1}^r (1-2\eta\lambda_j)^k a_j^\top b_j^\perp, \\
\text{Err}_{train}^\parallel(k) &= \sum_{j,l=1}^r (1-2\eta\lambda_j)^k (1-2\eta\lambda_l)^k a_j^\top P_{jl}^\parallel a_l + 2 \sum_{j=1}^r (1-2\eta\lambda_j)^k a_j^\top b_j^\parallel,
\end{aligned}$$

where

$$\begin{aligned}
P_{jl}^\perp &= \int_\delta^T \frac{w(t)}{h_t^2} \mathbb{E}[\sigma_{t,u_j} \sigma_{t,u_l} P_t^\perp(X_t(z))] dt, \quad b_j^\perp = \int_\delta^T \frac{w(t)}{h_t^2} \mathbb{E}[\sigma_{t,u_j} P_t^\perp(X_t(z))(\frac{A^*}{\sqrt{p}}\sigma_t(X_t(z)) - m(t, X_t(z))] dt, \\
P_{jl}^\parallel &= \int_\delta^T \frac{w(t)}{h_t^2} \mathbb{E}[\sigma_{t,u_j} \sigma_{t,u_l} P_t^\parallel(X_t(z))] dt, \quad b_j^\parallel = \int_\delta^T \frac{w(t)}{h_t^2} \mathbb{E}[\sigma_{t,u_j} P_t^\parallel(X_t(z))(\frac{A^*}{\sqrt{p}}\sigma_t(X_t(z)) - m(t, X_t(z))] dt
\end{aligned} \tag{28}$$

and recall  $\sigma_{t,u_j} = \frac{u_j^\top \sigma_t(X_t(z))}{\sqrt{p}}$  for all  $j \in [r]$ . It is worth mentioning that

$$P_{jl}^\perp + P_{jl}^\parallel = \int_\delta^T \frac{w(t)}{h_t^2} \mathbb{E}[\sigma_{t,u_j} \sigma_{t,u_l}] dt = \lambda_j \mathbf{1}_{j=l}, \quad b_j^\perp + b_l^\parallel = 0.$$

Hence  $\text{Err}_{train}(k) = \text{Err}_{train}^\perp(k) + \text{Err}_{train}^\parallel(k)$ . □

## I Experimental Details

In this section, we list the specific model architectures and hyperparameters that were not included in the main text.

### I.1 Two Points in 2D Plane

#### Model Architectures

- **RFNN:** Our RFNN model strictly follows the architecture defined in Eq. (6), with a model width of  $p = 2000$  and a temporal embedding dimension of  $K_t = 128$ .

- **MLP:** We employ a two-layer MLP for  $f(\mathbf{x}, t)$ . The scalar  $t$  is first transformed via a sinusoidal embedding of dimension 32. This embedding is concatenated with the input  $\mathbf{x} \in \mathbb{R}^2$ , passed through a hidden layer of 128 units with ReLU activation, and finally projected to  $\mathbb{R}^2$ .

**Training and Loss Computation** For the RFNN with width  $p = 2000$ , we optimize the model via gradient descent for  $10^7$  epochs with a learning rate of  $5 \times 10^{-4}$ . For the MLP, we trained for  $3 \times 10^4$  epochs with a learning rate of  $1 \times 10^{-4}$ . Both models share the same optimizer (Gradient Descent, performed using the full-batch SGD optimizer in PyTorch) and loss function (4). We numerically evaluate the integral in the loss function (4) using the trapezoidal rule with 2,000 discretization points.

**SDE and Sampling Details** We model the diffusion process using a stochastic differential equation (SDE) with a drift coefficient of  $f(x, t) = -x$  and a constant diffusion coefficient of  $g(t) = \sqrt{2}$ . For generation, we employ the Euler-Maruyama sampler with  $N = 1000$  discrete time steps. The time schedule follows a geometric progression decaying from  $T = 10$  down to  $\delta = t_{min} = 10^{-3}$ . Specifically, the time points are defined as  $t_i = T \cdot (t_{min}/T)^{i/N}$  for  $i = 0, \dots, N$ .

## I.2 More Points in 2D Plane

We use the RFNN model with the same architecture, training, and sampling settings as described in Section I.1. The only differences are the training epochs: for the four-point case (Figure 6), we train for 5,000,000 epochs with  $lr = 0.0005$ ; for the three-point case (Figure 7), we train for 3,000,000 epochs with  $lr = 0.0005$ .

## I.3 MNIST

**Model Architectures** We utilize Multi-Layer Perceptrons (MLPs) for all components of our framework.

- **VAE Architecture:** The encoder maps the flattened input image ( $\mathbb{R}^{784}$ ) to the latent space through two hidden layers with 400 and 200 units, respectively. It uses ReLU activations and outputs the mean and log-variance parameters. The decoder mirrors this structure (latent  $\rightarrow$  200  $\rightarrow$  400  $\rightarrow$  784) and uses a Sigmoid activation at the final layer to ensure pixel values lie within  $[0, 1]$ .
- **Latent Score Network:** The score model is a time-conditioned MLP. The time step  $t$  is first mapped to a 128-dimensional feature vector using Sinusoidal Embedding. This embedding is concatenated with the input vector and passed through three fully connected layers (sizes: input  $\rightarrow$  256  $\rightarrow$  256  $\rightarrow$  latent dimension) with ReLU activations to estimate the score function.

**Training Configuration** All models are trained on a single GPU using the Adam optimizer with a batch size of 1024.

- **VAE Training:** The VAE is trained for 100 epochs with a learning rate of  $10^{-3}$ . It minimizes the standard Evidence Lower Bound loss.
- **Score Model Training:** The latent diffusion model is trained for 300 epochs with a learning rate of  $10^{-4}$ . The loss function follows the denoising score matching objective (4). The weight schedule in the loss function is set to a constant  $w(t) = 1$ .

**SDE and Sampling Details** We model the diffusion process using a stochastic differential equation (SDE) with a drift coefficient of  $f(x, t) = -x$  and a constant diffusion coefficient of  $g(t) = \sqrt{2}$ . For generation, we employ the Euler-Maruyama sampler with  $N = 1000$  discrete time steps. The time schedule follows a geometric progression decaying from  $T = 10$  down to  $\delta = t_{min} = 10^{-3}$ . Specifically, the time points are defined as  $t_i = T \cdot (t_{min}/T)^{i/N}$  for  $i = 0, \dots, N$ .

## I.4 Derivation of the Newton Distance Estimator

First notice that the condition  $E(x)E(x)^\top \nabla \log p(x) = 0$  in our definition is equivalent to  $E(x)^\top \nabla \log p(x) = 0$ , as the columns of  $E(x)$  are orthonormal. Since  $E(x)$  has full column rank, the projection of the gradient vanishes if and only if its coordinates in the normal basis are all zero. Then we can only consider  $F(x) = E(x)^\top \nabla \log p(x) = 0$ .

To measure the distance from a point  $x$  to  $\mathcal{R}_{d^*}$ , we perform a first-order Taylor expansion of the condition  $F(x) = E(x)^\top \nabla \log p(x) = 0$  within the normal space  $\text{span}\{E(x)\}$ . By neglecting high-order variations of the eigenvector field  $E(x)$ , we obtain:

$$0 = F(x + \delta) \approx F(x) + [E(x)^\top \nabla^2 \log p(x)] \delta$$

Since the distance vector  $\delta$  lies in the normal space, we set  $\delta = E(x)\eta$ . Substituting the spectral decomposition  $\nabla^2 \log p(x)E(x) = E(x)\Lambda_\perp(x)$ , the equation becomes:

$$0 \approx E(x)^\top \nabla \log p(x) + E(x)^\top E(x)\Lambda_\perp(x)\eta$$

Given  $E(x)^\top E(x) = I$ , we solve for  $\eta$ :

$$\eta = -\Lambda_\perp(x)^{-1} E(x)^\top \nabla \log p(x)$$

The distance estimator  $\hat{d}_{\text{Newton}}(x)$  is the magnitude of this vector,  $\|\eta\|_2$ .

## J More Experiment Results

### J.1 RFNN on Different Sets

#### Two-Point Case: (-3,0), (3,0)

We present detailed visualizations of the sampling dynamics for the symmetric two-point configuration (centers at  $(\pm 3, 0)$ ). We compare three distinct weight schedules to examine their impact on the generation process:  $w(t) = 1$  (Figure 9),  $w(t) = h_t$  (Figure 10), and  $w(t) = h_t^2$  (Figure 11). These comparisons demonstrate that while the proposed three-stage evolution—Reach, Normal Alignment, and Tangent Sliding—is consistent across different settings, the choice of weight schedule significantly influences the timing of each phase and the quality of generated samples.

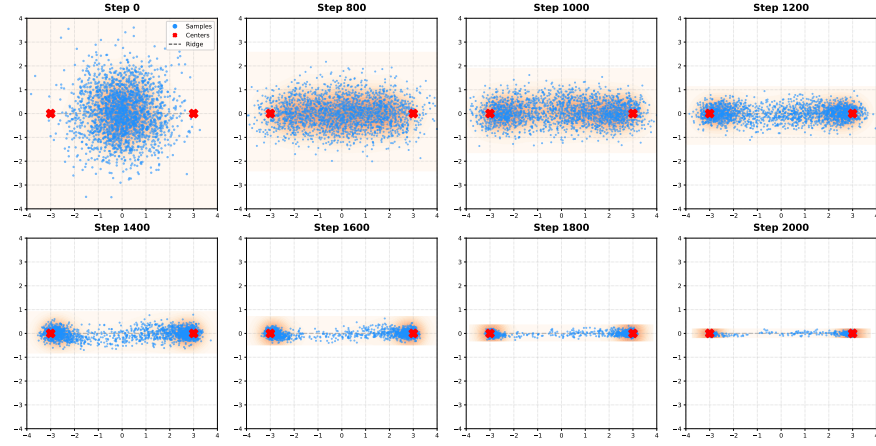


Figure 9: **Evolution of generated samples under the proposed sampling dynamics with weight schedule  $w(t) = 1$ .** The visualization displays snapshots of  $N = 2000$  particles in a 2D plane during the sampling process. The background contours depict the kernel density estimation (KDE) of the particle distribution. Samples reach the ridge neighborhood at **Step 800**. **Steps 800–1800** illustrates Normal Alignment. **Steps 1800–2000** demonstrate Tangent Sliding.

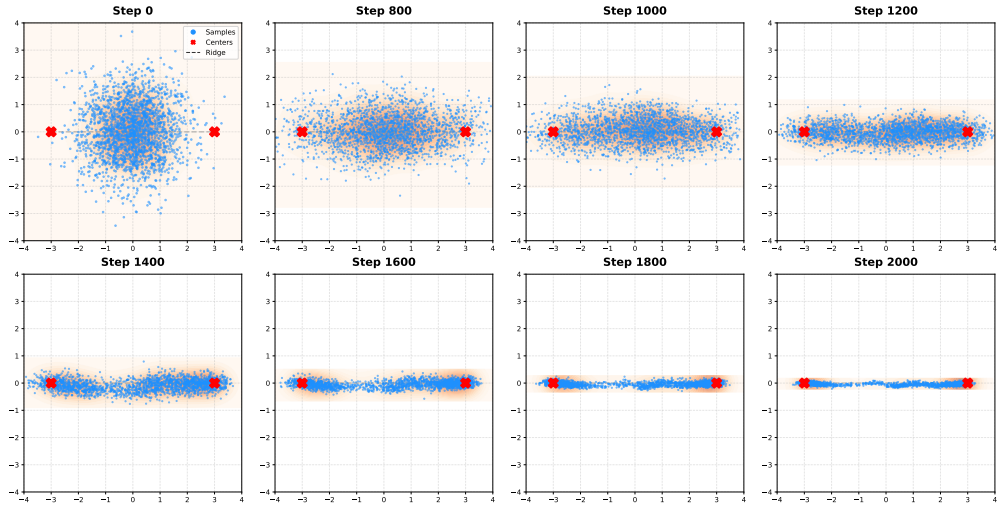
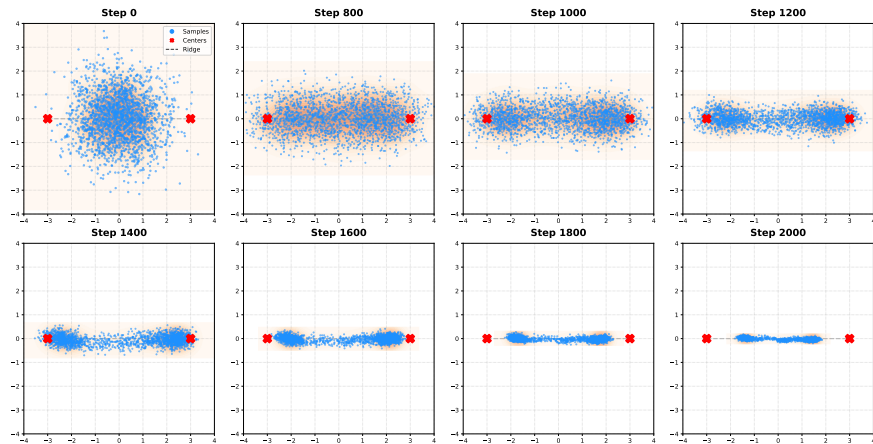


Figure 10: **Evolution of generated samples under the proposed sampling dynamics with weight schedule  $w(t) = h_t$ .** The visualization displays snapshots of  $N = 2000$  particles in a 2D plane during the sampling process. The background contours depict the kernel density estimation (KDE) of the particle distribution. Samples reach the ridge neighborhood at **Step 800**. **Steps 800–1800** illustrates Normal Alignment. **Steps 1800–2000** demonstrate Tangent Sliding.



**Figure 11: Evolution of generated samples under the proposed sampling dynamics with weight schedule  $w(t) = h_t^2$ .** The visualization displays snapshots of  $N = 2000$  particles in a 2D plane during the sampling process. The background contours depict the kernel density estimation (KDE) of the particle distribution. Samples reach the ridge neighborhood at **Step 1200**. **Steps 1200–1800** illustrates Normal Alignment. **Steps 1800–2000** demonstrate Tangent Sliding.

### Three-Point Case: (0,0), (5,0), (0,5)

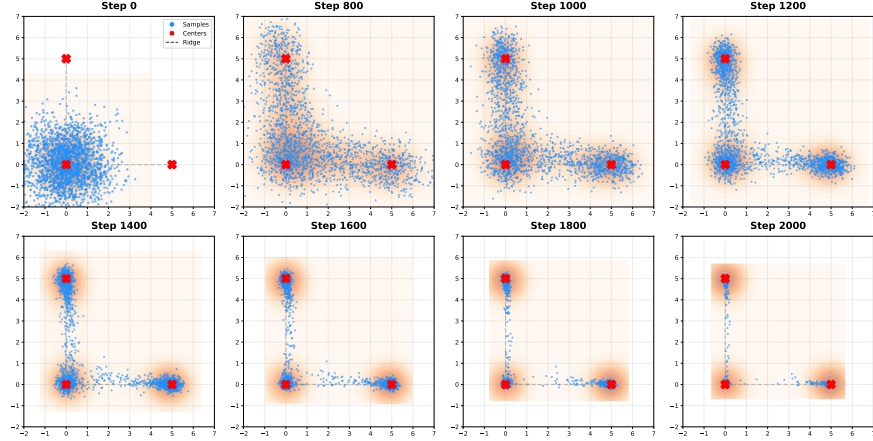


Figure 12: **Evolution of generated samples under the proposed sampling dynamics with weight schedule  $w(t) = 1$ .** The visualization displays snapshots of  $N = 2000$  particles in a 2D plane during the sampling process. The background contours depict the kernel density estimation (KDE) of the particle distribution. Samples reach the ridge neighborhood at **Step 800**. **Steps 800–1400** illustrates Normal Alignment. **Steps 1400–2000** demonstrate Tangent Sliding.

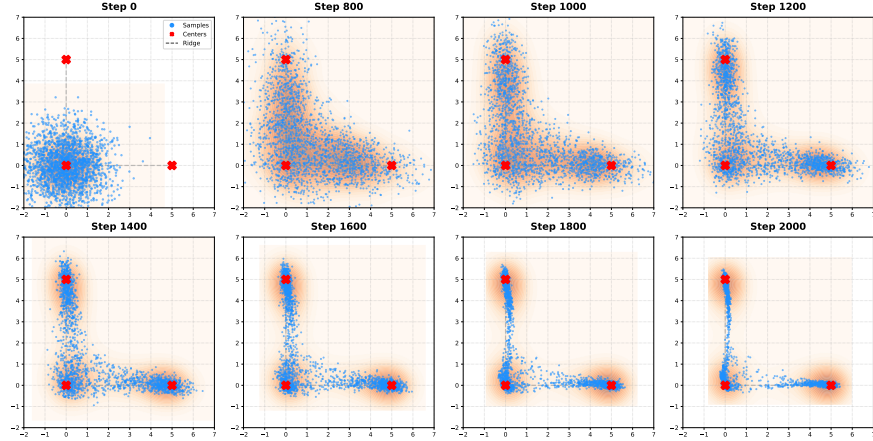
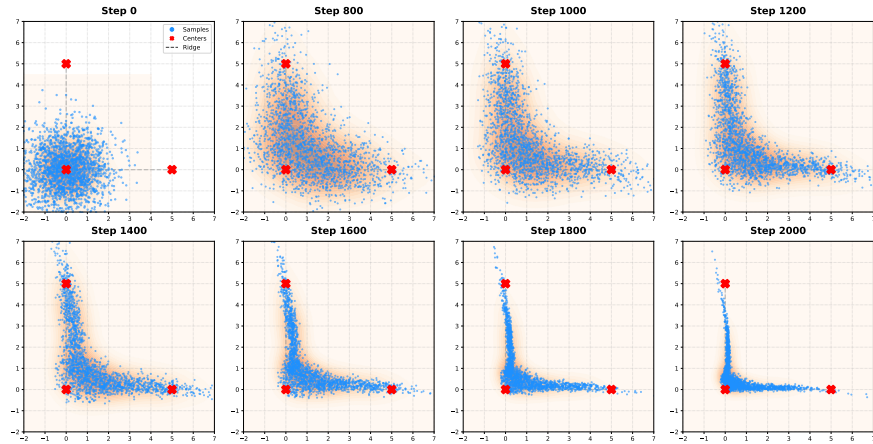


Figure 13: **Evolution of generated samples under the proposed sampling dynamics with weight schedule  $w(t) = h_t$ .** The visualization displays snapshots of  $N = 2000$  particles in a 2D plane during the sampling process. The background contours depict the kernel density estimation (KDE) of the particle distribution. Samples reach the ridge neighborhood at **Step 1000**. **Steps 1000–1600** illustrates Normal Alignment. **Steps 1600–2000** demonstrate Tangent Sliding.



**Figure 14: Evolution of generated samples under the proposed sampling dynamics with weight schedule  $w(t) = h_t^2$ .** The visualization displays snapshots of  $N = 2000$  particles in a 2D plane during the sampling process. The background contours depict the kernel density estimation (KDE) of the particle distribution. Samples reach the ridge neighborhood at **Step 1200**. **Steps 1200–1600** illustrates Normal Alignment. **Steps 1600–2000** demonstrate Tangent Sliding.

## Four-Point Cases

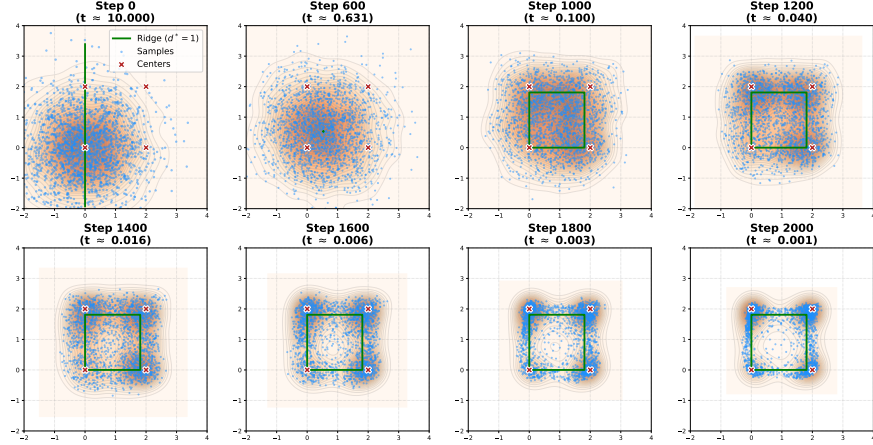


Figure 15: **Evolution of generated samples under the proposed sampling dynamics with weight schedule  $w(t) = h_t$ .** The visualization displays snapshots of  $N = 2000$  particles in a 2D plane during the sampling process. The background contours depict the kernel density estimation (KDE) of the particle distribution. Samples reach the ridge neighborhood at **Step 1200**. **Steps 1200–1600** illustrates Normal Alignment. **Steps 1600–2000** demonstrate Tangent Sliding.

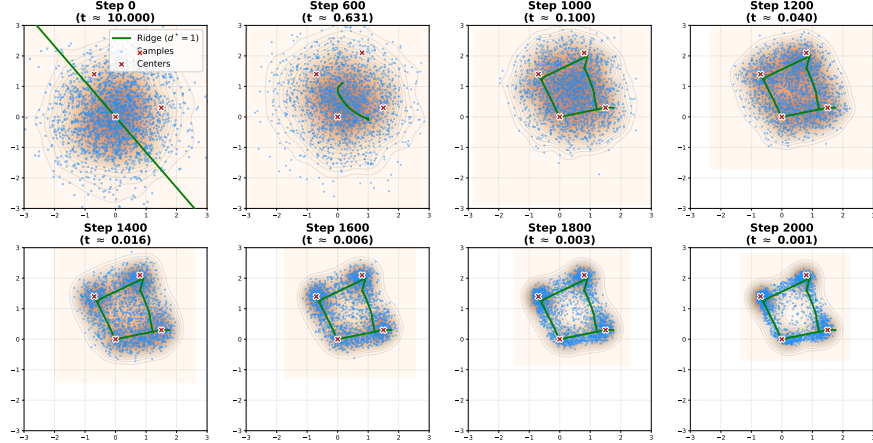


Figure 16: **Evolution of generated samples under the proposed sampling dynamics with weight schedule  $w(t) = h_t$ .** The visualization displays snapshots of  $N = 2000$  particles in a 2D plane during the sampling process. The background contours depict the kernel density estimation (KDE) of the particle distribution. Samples reach the ridge neighborhood at **Step 1200**. **Steps 1200–1600** illustrates Normal Alignment. **Steps 1600–2000** demonstrate Tangent Sliding.

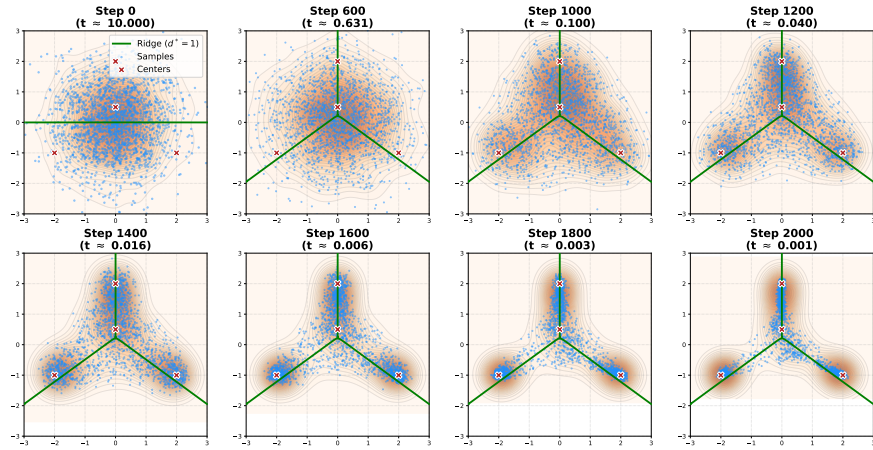


Figure 17: **Evolution of generated samples under the proposed sampling dynamics with weight schedule  $w(t) = h_t$ .** The visualization displays snapshots of  $N = 2000$  particles in a 2D plane during the sampling process. The background contours depict the kernel density estimation (KDE) of the particle distribution. Samples reach the ridge neighborhood at **Step 1200**. **Steps 1200–1600** illustrates Normal Alignment. **Steps 1600–2000** demonstrate Tangent Sliding.

## J.2 MNIST Trajectories

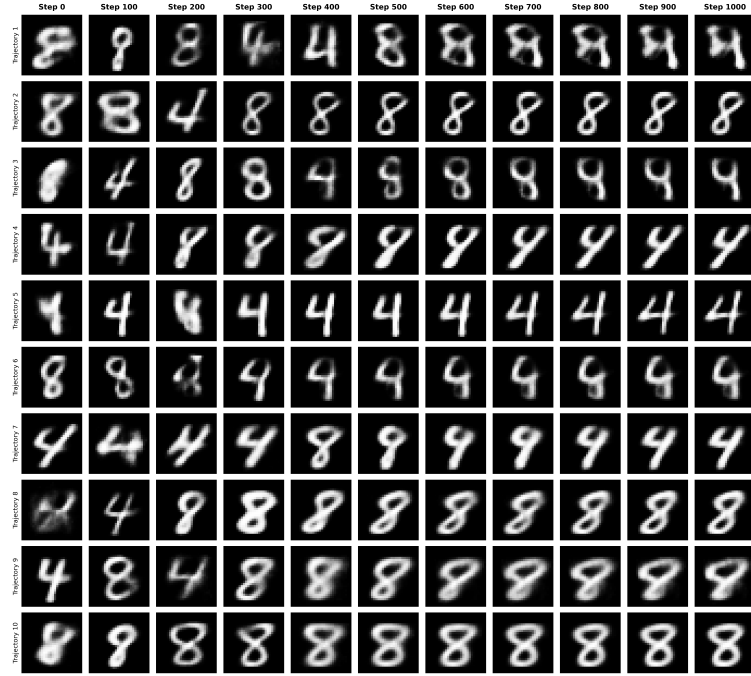


Figure 18: **Visualization of the full sampling evolution for 10 independent trajectories.** The process initiates from standard Gaussian noise at Step 0. Distinct geometric structures begin to emerge around Step 200 as the samples are pulled towards the ridge manifold. By Step 800, the digits (4 or 8) are clearly formed, showing that the semantic content has stabilized.

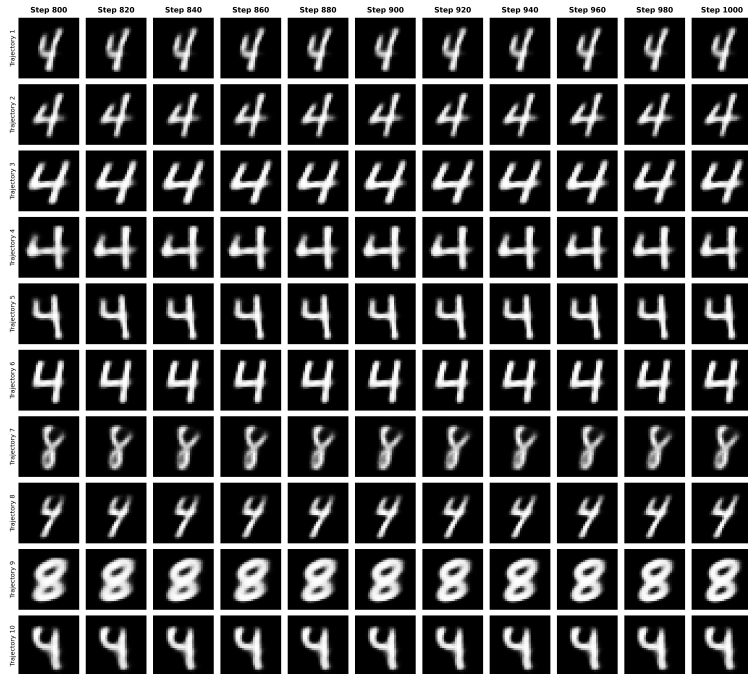


Figure 19: **Evolution during the final sampling phase (Steps 800–1000).** In this regime, the visual changes are negligible, restricted to minor high-frequency refinements. This visual stability corroborates our quantitative finding that the tangent direction error plateaus, indicating that the generated samples remain stationary on the manifold rather than drifting towards specific training data points.